THÈSE de DOCTORAT de L'UNIVERSITÉ de LILLE 1

Spécialité: Mécanique

CONTRÔLE ACTIF EN BOUCLE FERMÉE POUR LE RECOLLEMENT D'UNE COUCHE LIMITE TURBULENTE ÉPAISSE

Présentée et soutenue par

Tamer SHAQARIN

pour obtenir le grade de DOCTEUR de l'UNIVERSITÉ de LILLE 1

Soutenue le 12 Juillet 2011 devant le jury composé de:

M. **Eduardo WESFREID**	*Rapporteur*	*Directeur de recherche CNRS*	*PMMH, Paris*
M. **Bernd NOACK**	*Rapporteur*	*Directeur de recherche CNRS*	*ENSMA , Poitiers*
M. **Rudibert KING**	**Président**	*Professeur*	*TU, Berlin*
M. **Michel STANISLAS**	*Directeur de thèse*	*Professeur*	*LML-EC, Lille*
M. **Thierry FLOQUET**	*Examinateur*	*Chargé de recherche CNRS*	*LAGIS-EC, Lille*
MMe. **Caroline BRAUD**	*Co-directrice de thèse*	*Chargé de recherche CNRS*	*LML, Lille*
M. **Jean-Claude COURTY**	*Invité*	*Responsable du service aérodynamique*	*Dassault Aviation*

Dedicated to the memory of my father.

Résumé

Cette étude concerne l'étude d'actionneurs jets pulsés pour le contrôle de décollements sur une rampe. Des expériences de contrôle en boucle ouverte puis en boucle fermée ont été effectuées avec succés pour rèattacher une couche limite turbulente épaisse ($\delta = 20\,cm$). Ces tests ont été effectués dans la soufflerie de couches limites du LML (caractérisée par Carlier and Stanislas [2005]), celle-ci ayant la particularité d'avoir une couche limite dilatée permettant d'obtenir des nombre de Reynolds et des temps caractéristiques long. Différents nombre de Reynolds basés sur l'épaisseur de quantité de mouvement ont été testés dans la gamme: Re_θ =7500-12600.

Les tests de contrôle en boucle ouverte ont été menées dans la soufflerie pour sélectionner une entrée/sortie adaptée au problème de contrôle, pour identifier les échelles de temps du processus de décollement/réattachement, pour les modéliser, pour choisir les fréquences optimales et pour finalement les utiliser en contrôle en boucle fermée.

Ensuite, des contrôleurs simples (Proportionnel Intégral (PI) et Régulateur Linéaire Quadratique (RLQ)) ont été implémenté en oeuvre expérimentalement en boucle fermée et comparé à des simulations. La réactivité du contrôle, à vitesse de l'écoulement constante est améliorée par rapport aux résultats en boucle ouverte. La robustesse des contrôleurs a été testée avec des variations de la vitesse de l'écoulement. Ces tests ont mit en évidence la nécessité de contrôleurs plus complexes. Dans cette optique, des contrôleurs robustes H_∞, basés sur le modéle linéaire du premier ordre extrait des expériences en boucle ouverte, ont été conu et simulés. Un modéle Linéaire à Paramètres Variables (LPV) a été proposé. Celui-ci tient compte des variations de la vitesse de l'écoulement. Finalement, un contrôleur H_∞ LPV a été proposé pour de future implémentations expérimentales. Il donne de bon résultats en dépit des variations de la vitesse de l'écoulement dans la gamme étudiée.

Abstract

The current study deals with the employment of the pulsed jet actuators for flow separation over a ramp. Open and closed-loop control experiments were successfully performed to reattach a thick turbulent boundary layer, thanks to large scales of the facility (LML wind tunnel) characterized by Carlier and Stanislas [2005]. They were performed at three Reynolds numbers based on the momentum thickness of the turbulent boundary layer, varying from Re_θ =7500 to 12600.

Open-loop control were conducted in wind tunnel experiments to select an adequate input/output for the control problem, identify the time scales of the separation/attachment process, model the separated flow system under actuation, study the influence of the actuation frequency and extract the optimal frequencies in the range of study to be used in closed-loop control. Then, simple controllers (Proportional-Integral and Linear Quadratic Regulator) were experimentally implemented in closed-loop configurations and compared to simulations. The control reactivity at constant free stream velocity is improved compared to open-loop results. The robustness of the controllers is tested under variations of the free stream velocity, which highlights the need for more complex controllers.

H_∞ controllers based on first order model extracted in open-loop experiments, were designed and simulated. Linear Parameter Varying (LPV) model is proposed that takes into account free stream velocity variations. Then, an H_∞ LPV controller is proposed, that performs well in spite of free stream velocity variations in all the operating range.

Acknowledgements

There are many people that I must thank for their guidance and assistance presented in this Ph.D thesis. First of all, It is difficult to overstate my greatest appreciation and sincere gratitude to my advisor, Prof. Michel Stanislas. His guidances, scrupulous assistance and worthy advices were very valuable for me in each step of my research and writing of this thesis. Huge thanks goes for him for sharing with me his expertise and research insight. I could not have imagined having a better advisor and mentor for my Ph.D study. Also, Many thanks goes to my co-advisor Dr. Caroline Braud for the continuous support of my Ph.D study, for her patience, motivation, enthusiasm. She been my inspiration as I hurdle all the obstacles in the completion this research work.

I would like to thank the rest of my thesis committee: Dr. Eduardo Wesfreid, Dr. Bernd Noack, and Prof. Rudibert King, for their encouragement, insightful comments, hard questions and acceptance.

Many thanks goes to my fellow lab-mates and all the ER2 group in LML, for their help and support and for the comfortable and friendly environment I had during my work.

And I am deeply grateful to Tafila Technical University for the trust and support that they gave me in order to study in France, for following up my progress in this work. Also thanks to Erasmus Mundus for its financial

support that gave me this chance to fulfil one of my dreams.

I cannot finish without saying how grateful I am with my family: Specially for My lovely and amazing wife who supported me during my study and I acknowledge her motivation and understanding, my deepest thanks and gratitude for my great late father who always was the source of encouragement for me, for my beloved mother, brothers, sisters, for my sweet lovely kid who was born in the beginning of my research period and was source of joy and happiness, and for the rest of my beloved family.

Contents

List of Figures

List of Tables

Chapter 1

Introduction

Fluid flow significantly influences the performance of various systems such as transportation, industrial manufacturing, heating and cooling management. Recently a variety of flow control techniques have been developed for a wide range of applications (GadelHak [2000]). Flow control involves passive or active devices to effect a beneficial change in wall-bounded or free-shear flows. "Whether the task is to delay/advance transition, to suppress/enhance turbulence or to prevent/provoke separation, useful end results include drag reduction, lift enhancement, mixing augmentation and flow-induced noise suppression". (GadelHak [1996]). The science of flow control originated with Prandtl (1904), who introduced the boundary layer theory, explained the physics of the separation phenomena and described several experiments in which a boundary layer was controlled. Improving the efficiency of airplanes by flow control will significantly reduce the production of greenhouse gases and save money for the airlines and for customers. It is not just the increased lift by flow control, which will allow smaller and lighter engines which consumes less fuel. It is of course as well the reduced flow-induced drag exerted by different components of an aircaft, which will allow smaller engines (King-

Ed. [2007]).

Flow control has been used widely in aerodynamics application to inhibit flow separation (McManus et al. [1994]). Control of flow separation, historically referred to as boundary-layer control (BLC), is probably the oldest and most economically important (Gad-el-Hak and Bushnell, 1991). Generally it is desired to postpone separation so that form drag is reduced, stall is delayed, lift is enhanced and pressure recovery is improved. Separation control is broadly studied and reviews on its various applications have been published (GadelHak [1996]; Greenblatt et al. [2000]). Separation control has been demonstrated in a wide variety of configurations, such as flow over backward-facing steps and ramps, on sharp leading-edge wedges, on bluff bodies, on various airfoils, delta wings, circular cylinders and behind two-dimensional fences (Greenblatt et al. [2000]).

Passive separation control has been widely applied to compressor blades, diffusers, airfoils, and the after body of aircraft fuselages. Passive vortex generator are essentially small aspect-ratio airfoils mounted on the surface (GadelHak [2000]). The most obvious advantage of active over passive control is the possibility to adapt the kind and size of control in a desired, if possible optimal way to the actual operating conditions of a process (King-Ed. [2007]). Many active device types were then developed for which, depending on the control source used, the control is of different nature (acoustic actuators, plasma actuators, fluidic actuators ...). Active separation control can be driven at time scales consistent with relevant flow dynamics.

Unsteady flow control is known to offer the same or even larger control authority as steady control, but with less cost of the control (King-Ed. [2007]). The pulsed jet vortex generators concept for separation control was initially based on producing streamwise vortices. This is achieved by energiz-

ing the boundary layer through turbulent mixing of high-speed external fluid into the low-speed boundary layer fluid, causing an increase in the boundary layer momentum flux (Tilmann and Langan [2000]). Vortex generators jets shown in figure 1.1, are pitched to the surface at an angle β and skewed to the free stream velocity at an angle α to mimic passive vortex generators. The configuration described in the figure is co-rotating vortex generator, as the one used in the present work. Where λ is the distance between two jets and ϕ is the internal diameter of the jet. The other key parameters of the

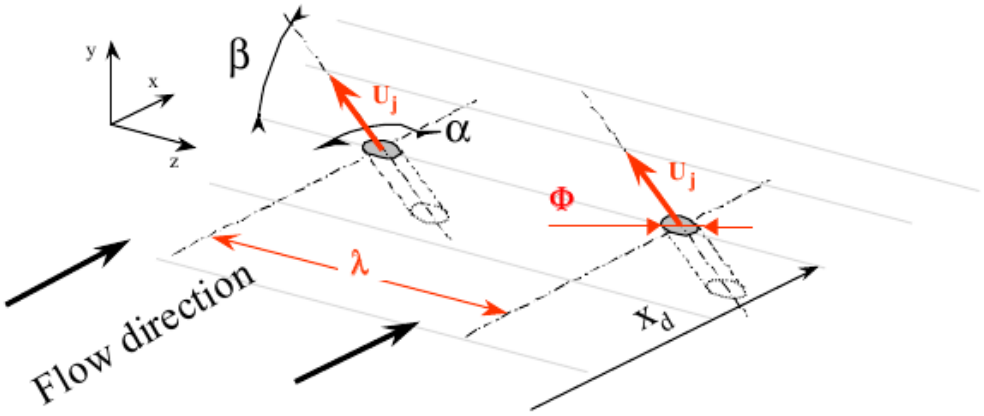

Figure 1.1: Co-rotating round jets vortex generators configuration

pulsed jets vortex generators used for separation control are the duty cycle and actuation frequency. The duty cycle indicates the percentage of the time that the jet is on. The reduced jet actuation frequency, F^+, is defined as

$$F^+ = \frac{f L_{sep}}{U_\infty} \tag{1.1}$$

where f is the actuation frequency, L_{sep} the characteristic length of the separated region and U_∞ the free stream velocity. The inverse of this dimensionless property stands for the ratio of one period of jet actuation to the time of

flight of free stream over the controlled domain (Amitay and Glezer [2002a]). Most of the previous studies on active separation control using synthetic jets have demonstrated that the effective reduced jet actuation frequency should be chosen such that $F^+ \approx 1$ (Seifert et al. [1996], Seifert and Pack [1999] and Amitay and Glezer [2002a]). This result will be compared to the current work using pulsed jet vortex generators.

Unsteady jet also gives the capability for the implementation of closed-loop control of separated flows, by coupling them with suitable sensors and controllers to increase the overall efficiency. Recently studies have been performed to demonstrate the feasibility of closed-loop implementations to further decrease the cost of the control to make it more robust using the operating parameters of the actuators (actuation frequency, duty cycle, amplitude of the jet ...) (see e.g. Allan et al. [2000]; Becker et al. [2004]; Becker and King [2005]; Henning and King [2005]; Tian et al. [2006a]; Tian et al. [2006b]; Beaudoin et al. [2006]; Becker et al. [2007]; Song et al. [2007]; Pinier et al. [2007]; Benard et al. [2010]).

To improve the understanding of the separation mechanisms of turbulent flows in order to extend the validity of the models, some studies have compared the transient time between the two states of the flow (i.e. separated/attached) for different configurations (Amitay and Glezer [2002b]; Darabi and Wygnanski [2004]; Mathis et al. [2009]; Siauw et al. [2010]). Unfortunately, this time scale is not systematically reported in closed-loop studies and more experiments are needed. Another useful dimensionless property that will be used to compare the time scales of the separation/reattachment process with the literature is defined below (Siauw et al. [2010]):

$$t^+ = \frac{tU_\infty}{L_{sep}} \tag{1.2}$$

In the present work, thanks to the large scale of the wind tunnel (Car-

lier and Stanislas [2005]), the configuration is a ramp with a thick turbulent boundary layer before separation ($\delta = 20\,cm$). This extends to large Reynolds number and large time scales in the range of flow conditions for which open and closed-loop control configurations are investigated. In a previous set of experiments, at $U_\infty = 10\,m/s$, $Re_\theta = 12600$ and a slight adverse pressure gradient coefficient $\frac{d_C p}{ds} = 0.06$ (Cuvier et al. [2010]), a parametric study was conducted to choose the optimal actuator arrangements (exit hole geometry, spacing between jets, orientations ...). In the present study, open-loop experiments were performed for two main purposes. First, the adequate Input/Output variables were extracted to help in the closed-loop implementations. Then, the dynamics of the systems (i.e. three free stream velocities) were identified and their associated time scales extracted. At last, simple controllers (Proportional-Integral and Linear Quadratic Regulator) were implemented in closed-loop configurations to get a better reactivity of the system and to improve the robustness under variations of the free-stream velocity. In experiment, the number of controllers that can be tested is limited by time. but since the system is modelled, a wider range of controllers can be simulated in order to assess the performance of the different controllers used and to investigate possibilities to improve them. When the free stream velocity is constant, the system is addressed as a linear time-invariant (LTI) system. Hence, LTI controllers were designed. Unfortunately, it will be limited to a small range of free stream velocity. But, since the system dynamics changes with variation of the free stream velocity, the system can be treated as a linear parameter-varying (LPV) system. Then, a robust H_∞ LPV controller is proposed, that performs well in spite of free stream velocity variation in all the operating range.

1.1 Literature Review

In this section, some selected previous work that is relevant to the current study is reviewed and important knowledge is gathered. In particular, the fluidic actuators, the ramp model and the closed-loop separation control.

1.1.1 Fluidic actuator

Pulsed jet vortex generators (VGs) have been gaining widespread interest for use in flow control experiments. Kostas et al. [2009] have done a good review for separation control by means of pulsed jet VGs. Many studies on flow control over high-lift configurations (McManus et al. [1994], Cormick [2000], Braud et al. [2004]), bluff bodies (Siller and Fernholz [2007], Szumowski and Wojciechowski [2006]) or turbomachines (Lin and Hariharan [2002]) have proved the practical efficiency of fluidic actuators to control flow separation. It is well established that unsteady jest has significant advantages vs. steady ones for many flow control applications (Greenblatt et al. [2000], Smith and Swift [2003]). A pulsed jet is an unsteady jet which is ideally on or off in a periodic sense that can be characterized by a positive definite square wave with a duty cycle ($0 < DC < 100$). Hence, pulsed jets have both mean and unsteady components. One way to generate pulsed jets is to use an external flow source modulated by, for example, a fast acting solenoid valve (Bons et al. [2002], Kostas et al. [2005], Kostas et al. [2007], Braud et al. [2008] and Kostas et al. [2009]), a high speed siren valve (Allan et al. [2000] and Williams et al. [2006]) or rotating orifice/slot assembly (Choi et al. [2006]). Rotary type pulsed jet actuators are hard to implement in feed-back control due to their slow response. The solenoid valve pulsed jet actuator is more flexible and hence, it is possible to synchronize the valve with reference sensor

signal (Cattafesta and Sheplak [2009]).

1.1.2 The ramp model

The ramp model added in the wind tunnel for separation control purpose has been thoroughly described and characterized by Cuvier et al. [2010]. This model was built for the European project AVERT and it is described thoroughly in section 4.2. The extensive study of Cuvier et al. [2010] was targeted to optimize the parameters of continuous jet using many different configurations; co-rotative and counter rotative, blowing downstream ($\alpha = 45°$) and upstream ($\alpha = 135°$), two jet streamwise position ($\frac{\Delta X_{vg}}{\delta} = 0.6, 1.4$) and different jet spanwise distribution ($\frac{\lambda}{\Phi}$), two jet diameters $\Phi = 6\,, 12\,mm$, and different velocity ratio VR that ranged from 0.5 to 3.5 with a step of 0.5. The results showed that upstream blowing is more robust than downstream blowing and that there is no influence of the jet streamwise position for the tested positions ($\frac{\Delta X_{vg}}{\delta} = 0.6, 1.4$) and also the optimum jet spanwise distribution was found to be ($\frac{\lambda}{\Phi} = 13.6$) while the jet diameter $\Phi = 6\,mm$ was found to be better than $\Phi = 12\,mm$ in terms of mass consumption. For the velocity ratio VR, it was found that there is no effect for $VR < 1.5$ on the separated flow for both co-rotative and counter rotative blowing. For the counter rotating case, this effect is increasing progressively up to $VR = 2.5$. While for the co-rotative blowing case, increasing VR reduces the separation until fully attached. All the previous parameters were optimized by Cuvier et al. [2010] mainly in terms of the gain of skin friction coefficient and how the skewness of the hot film signal (in the separated/reattached region) is going towards the Gaussian distribution with actuation.

1.1.3 Closed-loop separation control

Recently a variety of closed-loop separation control techniques have been developed for a wide range of applications and geometries. Allan et al. [2000] developed two 2nd order models for both the separated flow over a hump and the actuator. Then a discrete PID controller was designed to track the desired pressure gradient command by means of oscillatory blowing valve. The pressure gradient was the difference between the upstream and downstream pressure with respect to the jet exit slot. It was used to characterize the degree of flow reattachment and referred as pressure recovery parameter. Closed-loop control was successfully implemented, but with no such improvement on the control reactivity compared to open loop results.

Becker et al. [2004] implemented a closed loop robust control both experimentally and numerically on the flow over a backward facing step. The control objective was based on the minimization of the reattachment length using loudspeakers as actuators. H_∞ controller based on a second order model have been compared to both PI controller and open loop control. Better tracking performance and disturbance rejection was found with the H_∞ controller, but still the controlled reattachment length followed the reference with a significant delay. Instead of single-input single-output (SISO) control, Henning and King [2005] used robust multi-input multi-output (MIMO) H_∞ controller based on a 4th order model, with four loud speakers and four sensors arrays. Also Becker and King [2005] used the same set-up to compare robust H_∞ controller based on a 1st order linear model with flatness based controller in combination with nonlinear black box model. The flatness based control improved the tracking performance. Becker et al. [2004]; Henning and King [2005]; Becker and King [2005] succeded to reduce the reattachment length up to $\frac{\Delta x_r}{h} = 2$, where x_r is the reattachment length and

h is the step size.

Becker et al. [2007] used SISO extremum seeking control for separation control using pulsed jet actuator over a two elements high lift configuration. Then, they extended it to SISO slope seeking control to avoid saturation of the control input. Finally, for more realistic 3D flight configurations, spanwise MIMO slope seeking control was used. The pressure gradient on the flap was used as criteria for reattachment.

Tian et al. [2006a] have used adaptive closed-loop to control separation on NACA airfoil 0025 by means of zero-net mass flux (ZNMF) actuators. The control strategy was based on simplex optimization algorithm for the lift to drag ratio. Energy consumption penalty was added to the cost function to minimize the control effort. Tian et al. [2006b] also implemented an adaptive disturbance rejection control algorithm with system identification to control the separation over a NACA 0025 airfoil, using synthetic actuators and two dynamic pressure sensors. The objective was to minimize the unsteady pressure fluctuations over the airfoil, which results up to ~ 5 dB of power reduction and $\sim 5\times$ improvement in the lift/drag ratio. Song et al. [2007] used the same set-up with MIMO generalized predictive control algorithm. The results showed that $\sim 7\times$ improvement in the lift/drag ratio with less computational cost compared to Tian et al. [2006b].

Pinier et al. [2007] have used proportional controller based on low order model to control separation on NACA 4412 airfoil by means of piezoelectric synthetic jets. The unsteady pressure measurements were used to estimate the proper orthogonal decomposition (POD) coefficients for the model. More recently, Benard et al. [2010] implemented slope seeking control to maximize the lift over a NACA 0015 airfoil using plasma actuators.

Table 1.1 presents a summary of closed-loop separation control experi-

ments available in the literature. As can be observed, most experiments are focused either on the backward facing step or on different NACA airfoils. A variety of actuators have been used, while sensors were mostly pressure transducers. Also a large variety of controllers were used. Most of the studies were at relatively low Reynolds number except that by Allan et al. [2000], where the chord Reynolds number was 16 millions.

Author	Controller	Approach	System	Actuator	Sensors	Separation criteria
Allan et al. [2000]	PID control based on 2nd order model	Exp and Sim	Hump model, $Re_c = 16 \times 10^6$	Siren type oscillatory valve	Dynamic pressure transducer and differential pressure transducer	pressure gradient, ($\frac{dC_p}{dx} = 0.77 \Rightarrow Separated$), ($\frac{dC_p}{dx} \geq 1.85 \Rightarrow$ Separation reduced significantly)
Becker et al. [2004]	H_∞ Robust control compared to PI controller	Exp and Sim	Backward facing step, $Re_h = 4000$	Slot loud-speakers	Microphones	reducing reattachment length
Henning and King [2005]	MIMO H_∞ Robust control	Exp and Sim	Backward facing step, $Re_h = 25000$	Slot loud-speakers	Microphones	reducing reattachment length
Becker and King [2005]	MIMO H_∞ Robust control based on 1st order linear model compared to flatness based controller in combination with nonlinear black box model	Exp and Sim	Backward facing step, $Re_h = 4000$	Slot loud-speakers	Microphones	reducing reattachment length
Becker et al. [2007]	SISO extremum seeking control, SISO and MIMO Slop seeking control	Exp	NACA 4412 airfoil and NACA 4415 flap, $Re_c = 0.5 \times 10^6$	Slot type pulsed jet actuator	Static pressure sensors	Pressure difference on the flap ($\Delta C_p \geq 1 \Rightarrow Attached$), ($\Delta C_p \cong 0 \Rightarrow Separated$)

Tian et al. [2006a]	Quasi static adaptive closed loop control based on simplex optimization	Exp	NACA 0025 airfoil $Re_c = 10^5$	ZNMF Synthetic jet	Balance that measure lift and drag by strain gauges	Maximize L/D, ($L/D \geq 1.27 \Rightarrow Sep.$), ($L/D > 2.4 \Rightarrow attached$)
Tian et al. [2006b]	Adaptive feedback disturbance rejection algorithm based on ARMARKOV system ID	Exp	NACA 0025 airfoil $Re_c = 10^5$	piezoelectric Synthetic jet	MEMS unsteady pressure sensors (Kulite LQ 125-5A)	Minimize the power of the pressure fluctuation over the airfoil
Pinier et al. [2007]	P control based on low order model	Exp	NACA-4412 airfoil $Re_c = 1.35 \times 10^5$	piezoelectric Synthetic jet	unsteady pressure transducers (ICP, from PCB Piezotronics)	Minimize the error between the estimated time-dependent POD coefficient and the desired state in which the flow is fully attached
Song et al. [2007]	MIMO generalized predictive control algorithm	Exp	NACA 0025 airfoil $Re_c = 1.2 \times 10^5$	piezoelectric Synthetic jet	MEMS unsteady pressure sensors (Kulite LQ 125-5A)	Minimize the power of the pressure fluctuation over the airfoil
Benard et al. [2010]	Slope seeking control algorithm	Exp	NACA 0015 airfoil, up to $Re_c = 4 \times 10^5$	DBD plasma actuator	Balance that measure lift by strain gauges (FN3148)	Maximize the lift

Table 1.1: Overview of closed-loop separation control experiments in the literature

1.2 Objectives of the Research

The primary goal of the present research is to assess the ability of fluidic actuators to reattach the present thick turbulent boundary layer and to provide a feedback control strategy of flow separation using fluidic actuators. The research aims at achieving this goal by meeting the objectives given below.

- Validate the theoretical model of fluidic actuators experimentally.
- Investigate the effect of their parameters (duty cycle, actuation frequency and velocity ratio) on the flow separation over a ramp model.
- Model the separated flow system with fluidic actuators using open-loop experimental results.
- Design linear controllers for the closed-loop separation control experiments and simulations, that meets performance and robustness objectives.

1.3 Organization

The current work begins with the background and motivation for this research.

Chapter 2 presents the fluidic actuator used. It describes the set-up, design and operation of the actuator. A theoretical model of the actuator is satisfactorily validated by experiments.

In **chapter 3**, some control theories are provided to be used for developing a feedback control system for flow separation. The performance specifications to design the controllers are presented. Then some theoretical basis

for the classical PID control and the Linear Quadratic Regulator (LQR) are documented. The classical control structure is then extended to the robust control structure. The robust H_∞ control theory is then presented.

Chapter 4 documents the experimental facility and instrumentations used for separation control experiments over the ramp model. Also it explains the hardware of the data monitoring and acquisition system.

In **chapter 5**, the results of the separation control using fluidic actuator on the ramp model are presented. This chapter is divided into two parts. In the first part, the experimental results of the open-loop separation control are discussed in terms of the choice of input/output variables. Moreover, the involved time scales are identified and discussed. The second part focuses on the experimental results of the closed-loop control experiments. The closed-loop response with the PI controller and LQR controller are discussed.

Chapter 6 presents the mathematical formulation of the control problem for the separated flow over the ramp model. Several types of controller are designed (PI, LQR and H_∞), and the closed loop system is simulated for each controller. Finally, a general linear parameter varying model is proposed to improve the robustness of the control. The formulation of this model is developed and a robust H_∞ LPV controller is implemented and tested.

In **chapter 7** the conclusion of the current work and some perspectives for future work are presented.

Chapter 2

Fluidic Actuator design and analysis

2.1 Introduction

Two types of fluidic actuators can be found mostly in the literature for flow control applications, synthetic jets and pulsed jets. Synthetic jets are often preferred, because no external flow source is needed and higher frequencies can be reached. However, for a full size application, one need to avoid blockage of the exit orifices from dust (suction phase of synthetic jets), and a high frequency is needed only in small or medium wind tunnel investigations (Petz and Nitsche [2007]). Moreover the highest exit velocity is limited for these zero net mass flow actuators (around 100 m/s), whereas practicable applications in aeronautics need a higher exit velocities (Petz and Nitsche [2007]). Hence both actuators possess advantage and disadvantage that need to be explored. For both of them the modification of inputs and physical parameters such as: the pitch and skew angles, the velocity ratio/momentum coefficient or the Duty Cycle/non-dimensional frequency has been extensively

explored (Bray and Garry [1999], Barberopoulos and Garry [1998], Kostas et al. [2007], Tilmann and Langan [2000], Lundell [2003], Amitay and Cannelle [2006], Greenblatt et al. [2000] and others).

It is well established that unsteady jet has significant advantages vs. steady jet for many flow control applications (Greenblatt et al. [2000], Smith and Swift [2003]). A pulsed jet is an unsteady jet which is ideally on or off in a periodic sense that can be characterized by a positive definite square wave with a duty cycle ($0 < DC < 100$). The duty cycle indicates the percentage of the time that the jet is on. Hence, pulsed jets have both mean and unsteady components. One way to generate pulsed jet is to use an external flow source to modulate the flow using, for example, a fast acting solenoid valve (Bons et al. [2002], Kostas et al. [2005], Kostas et al. [2007],Braud et al. [2008] and Kostas et al. [2009]), a high speed siren valve (Allan et al. [2000] and Williams et al. [2006]) or rotating orifice/slot assembly (Choi et al. [2006]). Rotary type pulsed jet actuators are hard to be implemented in feed-back control due it's slow response. The solenoid valve pulsed jet actuator is more flexible and hence, it is possible to synchronize the valve with reference sensor signal (Cattafesta and Sheplak [2009]).

However, the control depends strongly on the perturbations delivered by the actuators which is a result by the flow produced inside the device (Cattafesta and Sheplak [2009]). Recently, studies of Amitay and Glezer [2006] and Kostas et al. [2007] have highlighted the importance of the transient phases of the pulsed-jet actuators dynamic (i.e. opening time/closure of the actuator).

The pulsed-jet actuator used by Kostas et al. [2007] and Kostas et al. [2009], is considered in this chapter. The objective is to give tools to design pulsed jet actuators with known limitations for closed-loop control experi-

ments (see section 4.3). In the following sections the experimental set-up and the diagnostic tools for the actuator bench are described. Then the oscillatory stage of the model (Braud and Dyment [2011]) is solved numerically and compared to experiments.

2.2 Experimental set-up

A scheme of the actuator bench set-up is given in figure 2.1 and a sketch is shown in figure 2.2. As can be seen from figure 2.2, only one valve was used for these tests. The available pressurized air can provide up to 7 bar at 3 000 L/min. The air feed line is then connected to oil filters to avoid contamination of the hot-wire measurements. A compressed air regulator is then used to maintain the desired pressure, p_r, in the accumulator. A reservoir is placed upstream of the valve to damp the pressure fluctuations during each open/close cycle of the valves and hence provide a constant reservoir pressure of air (and so provide a constant flow rate) for the jet. A manometer is used to check the difference in pressure, $p_r - p_o$, where p_o is the pressure at the outlet of the valve. The temperature in the reservoir, θ_r, is supposed to be equal to the ambient air temperature, θ_o. The pressurized air arrives at the solenoid valve through feed lines which have been minimized to reduce losses. The solenoid valve is a usual 3/2 distributor type from FESTO. A throat is connected to the outlet of the valve, more details are given in subsection 2.2.1. Tubes of diameter D =4, 6 and 8 mm, can be connected to the end of the valve.

To measure the velocity at the actuator exit, a single hot-wire probe was placed at one diameter from the tube end. This ensures the probe is in the potential core, where the measurement error is a minimum. Before each

measurement a 3D micro-displacement system was used in the continuous mode of the actuator, to place the probe at the center of the velocity profile, perpendicular to the tube axis. The signal was observed in real time and was used to check for the maximum jet exit velocity at each transverse probe location. The hot-wire signal was converted to velocity using the standard King's law. A home made pressure probe was used for an in-situ calibration of the hot-wire. This probe was also displaced in the radial direction to evaluate the velocity profile fitted using the formula:

$$\frac{u(r)}{u_{max}} = \left(1 - \left(\frac{r}{R}\right)^{\frac{1}{n}}\right), \tag{2.1}$$

which corresponds to turbulent flow in pipes, where r is position of the probe and R is the maximum radius of the tube. Then, the mean velocity is given by

$$u_{mean} = u_{max}\frac{2n^2}{(n+1)(2n+1)}, \tag{2.2}$$

The hot-probe of standard type (i.e. platinum-plated tungsten wire 1.0 mm long and 5μm in diameter) was connected to a constant temperature anemometer manufactured by DISA. The signal from the anemometer was digitized. The acquisition frequency was 100 kHz and 500 000 samples were recorded for each measurement.

A dedicated unit with the DOS operating system was used to drive the valves in order to avoid any time management delays. An in-house computer software was used to generate the required driving signal (square waves) to operate the valve via a digital I/O card. For synchronization purpose, the square waves signal and the hot-wire signal were acquired at the same time in the same unit. During all bench experiments the duty cycle and the frequency were kept unchanged: $DC = 50\%$ and $f = 2Hz$.

The effect of tube Diameter D and tube length L, was investigated using nine different tube lengths ranging from $0.16\,m$ up to $2.72\,m$ for each tube

diameter ($D = 4$, 6 and 8 mm). The pressure effect was also characterised using twelve different absolute pressure ratios (p_r/p_o) ranging from 1.5 to 7 bar.

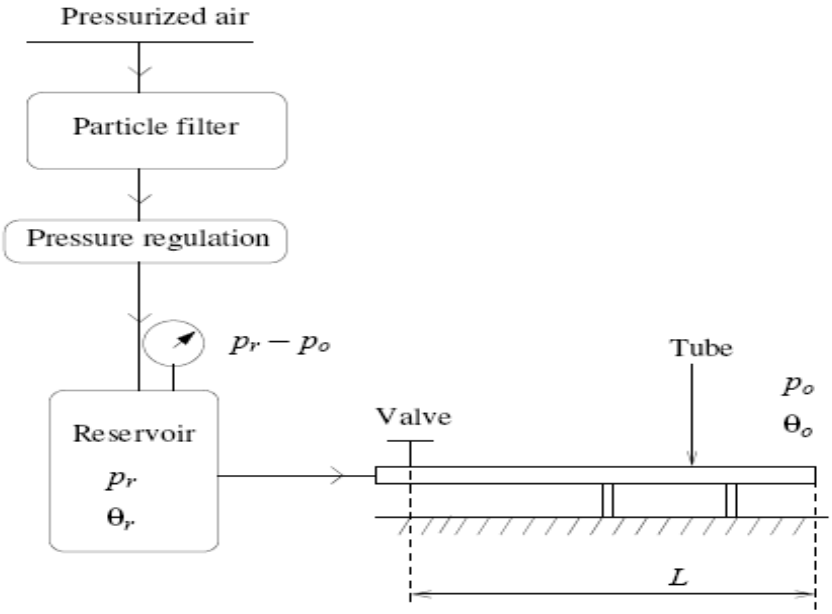

Figure 2.1: Scheme of the actuator bench set-up

2.2.1 Throat design

Basically, the throat addition at the outlet of the Festo valve was for two reasons; to ensure smooth convergence of the air flow by designing third order profile for the throat contraction, and to be sure about the throat diameter which was designed to be equal $1mm \pm 10\,\mu m$. Also because a sonic throat allows to neglect the flow in the valve (perturbations created downstream of the enlargement cannot be transmitted upstream of it). The conditions at the exit of the tube are repeatable which was not the case without the throat where the variations of the exit velocity was more than 30% (Braud et al.

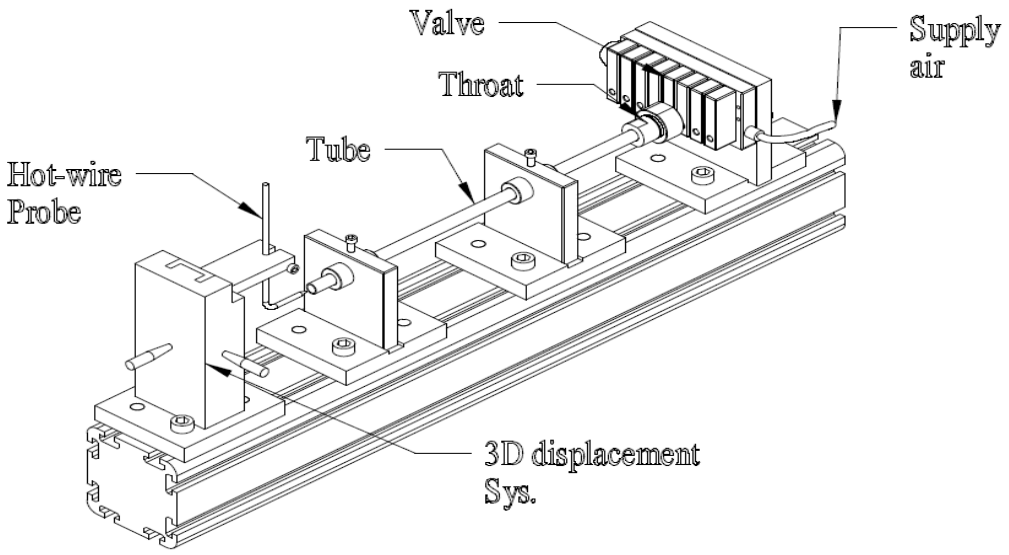

Figure 2.2: sketch of the the actuator set-up

[2008]).

Two throat were designed as depicted in figure 2.3(a) and figure 2.3(b). The Advantage of the first design was to use the same throat for different tube sizes, on the other hand it can generate flow leakage and pressure losses. The second design was done to minimize the losses but consequently each tube size needs a different throat, as it appears in figure 2.3(b) three features were added to avoid losses. First, the throat was done in one part while the attached part is for simplifying the O-Ring groove manufacturing only. Second, a circular groove was done to fit the tube from inside and outside and also to deal with improper cut of tube. Third, an O-Ring was added to avoid any external losses from the tube. For all tests conducted in this work, the second design was used.

Due to the high dependency of the exit velocity on the throat diameter,

the manufacturing of the throat done by high accuracy machine, "Electrical Discharge Machine" (EDM) with an accuracy down to 0.2 μm. Moreover, the circular groove was done using the EDM due the complexity of such groove manufacturing using conventional machines.

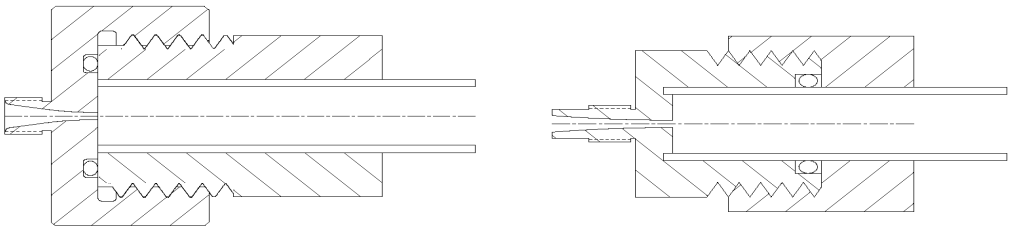

(a) Design 1 (b) Design 2

Figure 2.3: Throat Design

2.3 Continuous mode

A schematic representation of the apparatus is given in figure 2.4. Air is supplied through a valve from a reservoir (subscript $_r$); it runs along a tube of section S and is discharged into the atmosphere (subscript $_o$) where the pressure is constant. The valve contains a throat of section S_c , small with respect to S, where the velocity is sonic, which implies that the pressure p_r is sufficiently high with respect to p_o. The important enlargement at the entrance of the tube makes the velocity in the tube significantly lower than the speed of sound c_o. Friction losses along the tube are neglected with regard to the losses consecutive to the enlargement. The distance between the valve and the location where the flow reattaches is neglected in comparison with the length of the tube.

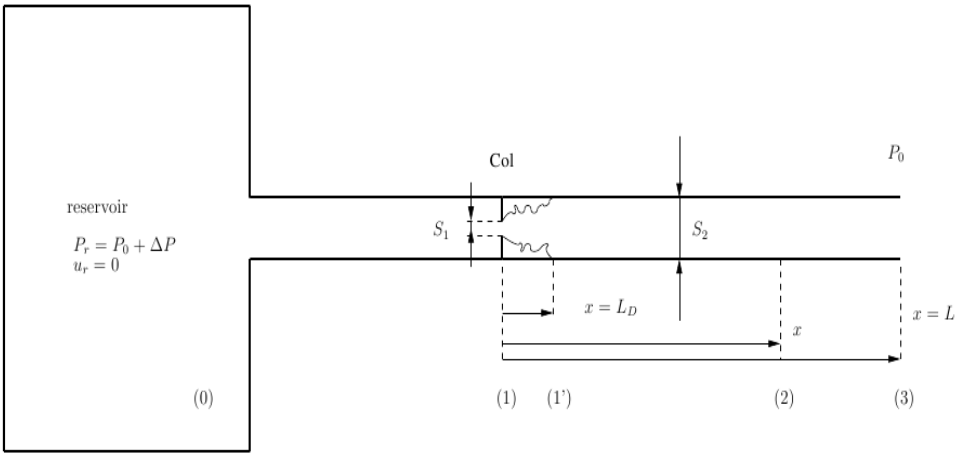

Figure 2.4: Sketch of the actuator

The model of actuator in the continuous mode is described below. More details can be found in Braud and Dyment [2011]. When the valve is maintained open, the flow is steady with a velocity U in the tube. Applying the conservation of mass and energy leads to:

$$\left(\frac{U}{c_k}\right)^2 + \frac{2}{\gamma - 1}\frac{S}{S_c}\frac{p_o}{p_k}\frac{U}{c_k} - \frac{\gamma + 1}{\gamma - 1} = 0, \tag{2.3}$$

with $p_k/p_r = (2/(\gamma + 1))^{\gamma/(\gamma-1)}$ and $\theta_r/\theta_0 = 2/\gamma + 1$, γ being the ratio of specific heats.

Generally, the temperatures θ_r and θ_0 are equal, so we obtain:

$$\left(\frac{U}{c_o}\right)^2 + \left[\frac{2}{\gamma - 1}\right]\left[\frac{\gamma + 1}{2}\right]^{\frac{\gamma+1}{2(\gamma-1)}}\frac{S_c}{S}\frac{p_r}{p_o}\frac{U}{c_o} - \frac{2}{\gamma - 1} = 0. \tag{2.4}$$

In the frame of the present model U is supposed much lower than c_o; on the other hand $2/(\gamma - 1) = 5$ for air. Therefore, the first term is negligible with the result:

$$\frac{U}{c_o} = \left[\frac{2}{\gamma+1}\right]^{\frac{\gamma+1}{2(\gamma-1)}} \frac{S_c}{S}\frac{p_r}{p_o}, \tag{2.5}$$

from what $S_c p_r$ must be significantly lower than $S p_o$.

The flow is sonic at the throat if the following condition, resulting from conservation of momentum at the enlargement is fulfilled:

$$\left(\frac{p_o}{p_k}\right)^2 - \left(1+\gamma\frac{S_c}{S}\right)\frac{p_o}{p_k} + \frac{\gamma(\gamma+1)}{2}\left(\frac{S_c}{S}\right)^2 < 0. \tag{2.6}$$

Previous remarks provide the range of the values p_r/p_o admissible in the framework of the model.

2.3.1 Experimental validation

Experiments have been performed with θ_r and θ_o close to $20° C$, $S/S_c = 16$, $S/S_c = 33.3$ and $S/S_c = 56.4$ for the tubes (4, 6 and 8 mm in diameter respectively), and various values of L and p_r/p_o. The condition (2.6) requires $p_r/p_o > 1.85$ which is valid for all tested S/S_c. On the other hand p_r/p_o must be significantly lower than 10.5 in order to have U/c_o small enough.

Figures 2.5 and 2.6 give the experimental results for the conducted tests. Figure 2.5 shows the effect of p_r/p_o on the exit velocity for different tube diameters and lengths. While figure 2.6 represent the dimensionless expression $\frac{S_c}{S}\frac{p_r}{p_o}$ as a function of U/c_o to validate equation 2.5 for $L/D = 120$. A good agreement is obtained with the above $1D$ model in equation 2.5, although it does not take into account the complex flow that occurs at the valve as well as the friction in the tube.

It is clear in figures 2.5 and 2.6 that the exit velocity for the $4\,mm$ tube is lower than expected by the theory (even though it still stays in the uncertainty range). For the $6\,mm$ and $8\,mm$ tubes the agreement is better, which

can be explained by the friction, which is smaller for larger tube diameters. In the following, the measurements of the transient exit velocity $v(t)$ are scaled using the steady value U acquired during the same experimental run.

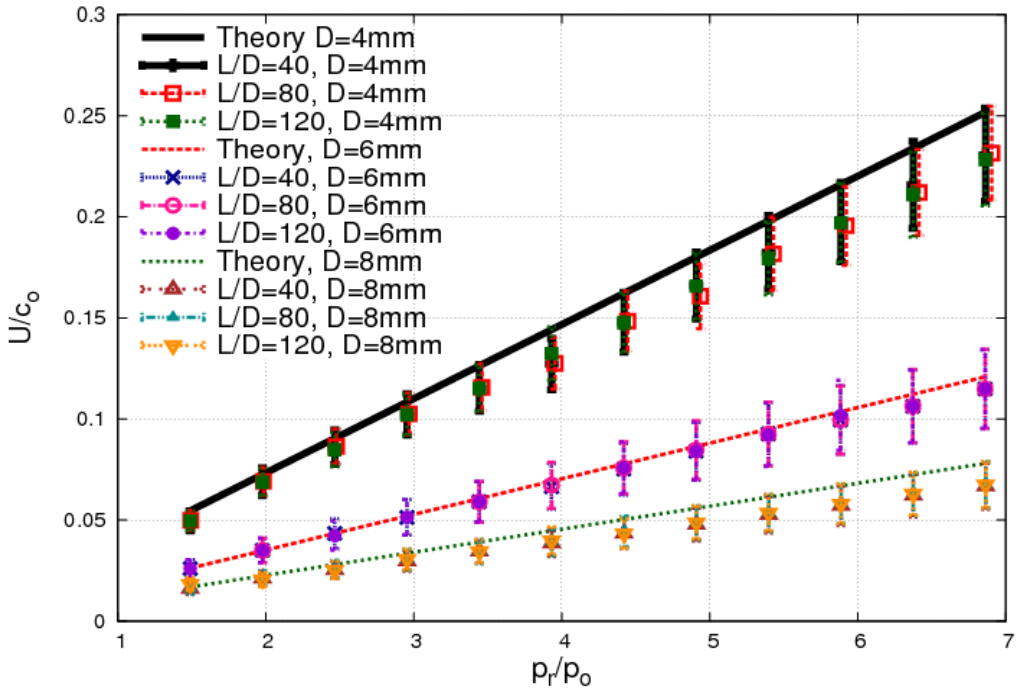

Figure 2.5: Comparison of the measured and theoretical exit velocity in the continuous mode of the actuator for D=4 mm, 6 mm and 8 mm respectively, and for various tube lengths.

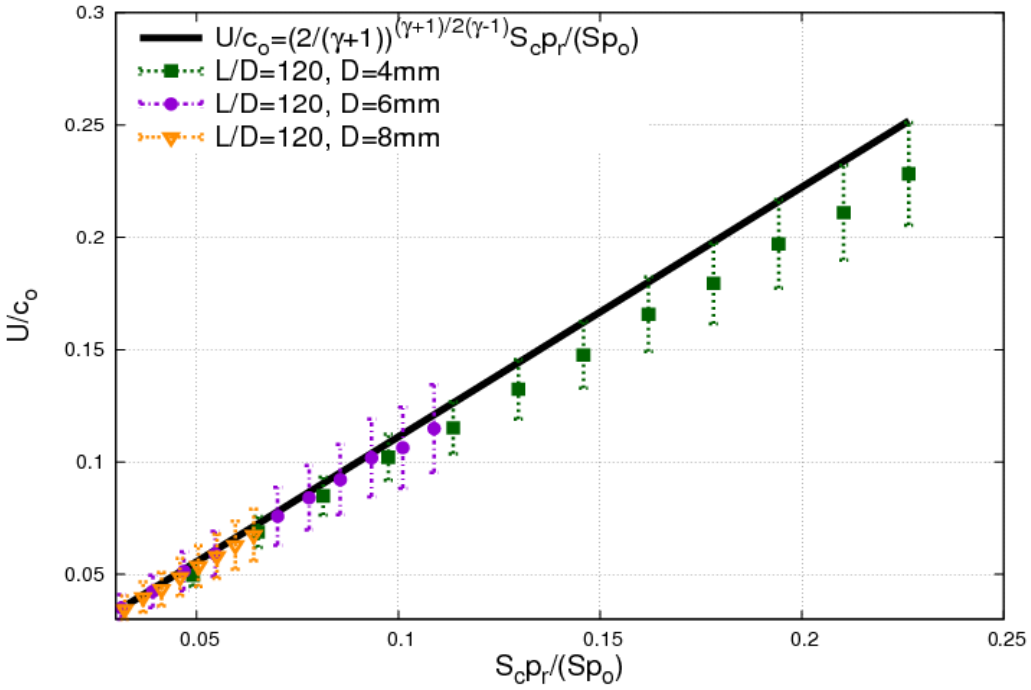

Figure 2.6: Exit velocity in the continuous mode as a function of . $\frac{S_c}{S}\frac{p_r}{p_o}$, compared to model of equation 2.5, for $L/D = 120$ and different tube diameter.

2.4 Pulsed mode

Experiments have been conducted with the same parameters as in the continuous mode . During all bench experiments the duty cycle and the frequency were : $DC = 50\%$ and $f = 2\,Hz$, and all the results were phase averaged over 4 cycles. As depicted in figure 2.7, the exit velocity were plotted for different tube lengths with $8\,mm$ tube diameter. It can be noticed in the figure that the amplitude and the frequency of the oscillations depends on the length of the tube. Also it is verifying that the exit velocity in the pulsed mode is equal the continuous exit velocity in the steady state. Moreover, it can be seen that there is delay at tube exit, which depends on the length of the tube. This delay is given in figure 2.8 which shows that it can be written as:

$$dt_a = \frac{L}{c_o} + dt_v \tag{2.7}$$

Where dt_a is the delay at tube exit and dt_v is the delay of the FESTO valve. It was checked that $dt_v = 0.95\,ms$ and it is constant for the valve used, which does not depend on the tube length.

The transient flow generated by a sudden opening of the valve is now considered. Once the valve is opened, an acoustic phenomena is generated, the interface at the front of the pressurized air issuing from the reservoir acts as a piston on the air initially at rest in the tube (figure 2.9). The velocity $u^{'}$ of the interface that is less than the speed of sound, increases with the time t from $u^{'} = 0$ at $t = 0$ up to the velocity U calculated by equation 2.5. The wave front is then displaced at a velocity equal to the speed of sound. When the pressure reaches its minimum $P = P_0$, at the exit of the tube, the wave front reflects in the opposite direction, then as

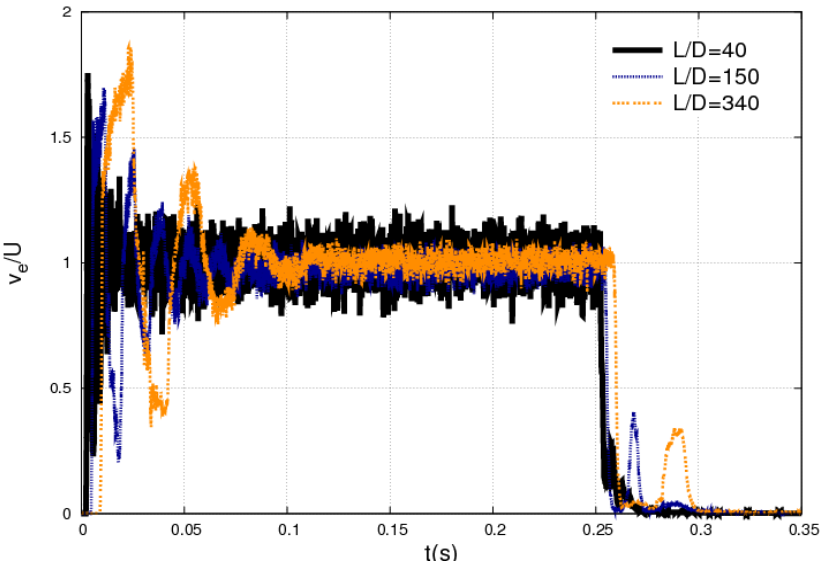

Figure 2.7: Exit velocity in the transient mode for $D = 8mm$

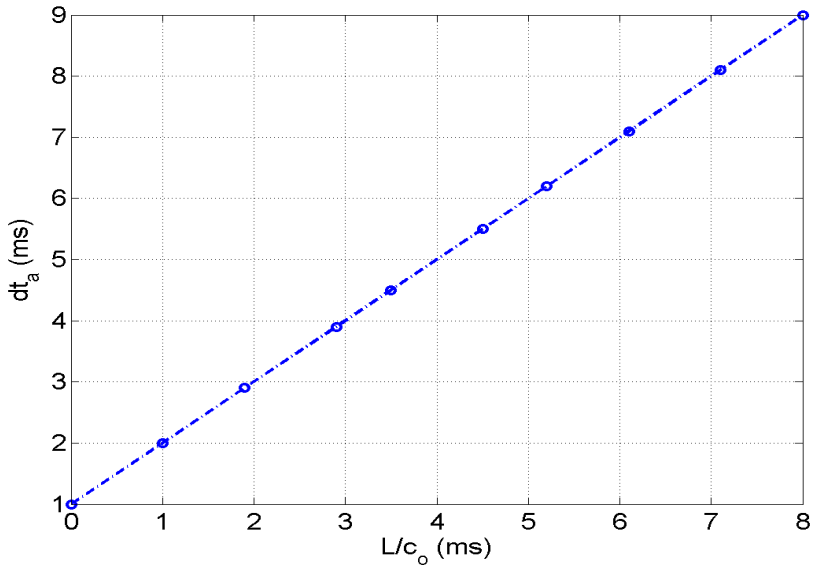

Figure 2.8: Delay at tube exit for different tube length

it reaches the maximum pressure it changes its direction again and so on, until the phenomena disappeared by the viscous effect. In reality, the first

wave front that is reflecting at the exit of the jet meets another oncoming wave front formed just after this one and so on. To simplify the model, this phenomenon will not be taken into account (more details can be found in Braud and Dyment [2011]). Also, the sonic jet does not form instantaneously at the throat and is not dependant of the length at the first instant of the opening. The jet is then steady and found experimentally to have a velocity equal to the steady velocity given by equation 2.5.

The relation between the interface velocity and the exit velocity described by Braud and Dyment [2011] is presented below, this relation will be used to calculate the interface velocity from the experimental exit velocity.

$$v(t) = 0 \quad \text{for} \quad 0 < t < L/c_o. \tag{2.8}$$

$$v(t) = 2u^{'}(t - L/c_o) \quad \text{for} \quad L/c_o < t < 3L/c_o. \tag{2.9}$$

$$v(t) = 2u^{'}(t - L/c_o) - 2u^{'}(t - 3L/c_o) \ \text{ for } \ 3L/c_o < t < 5L/c_o. \tag{2.10}$$

2.4.1 Numerical Results

The derivation of the transient model is described thoroughly in appendix B. Equations (B.3, B.4) with and without friction were solved using Godunov scheme with second order correction using Flux-limiter (Appendix B.2). With $D = 8\,mm$, $L = 1500\,mm$ and $p_r/p_o = 5\,bar$, the results are given in figure 2.10. The interface velocity used in the simulation depicted in figure 2.11 was calculated using equation 2.9. The model successfully predicts the exit velocity for the pulsed actuator (i.e. until $t \simeq \frac{2L}{c_o}$). After this duration the model fails to represent experimental results in terms of

time duration and level of oscillations. This is due to the complex interaction which is occurs with the first reflected wave. However, this model gives useful informations for the design of the valve which will be used in section 4.3.

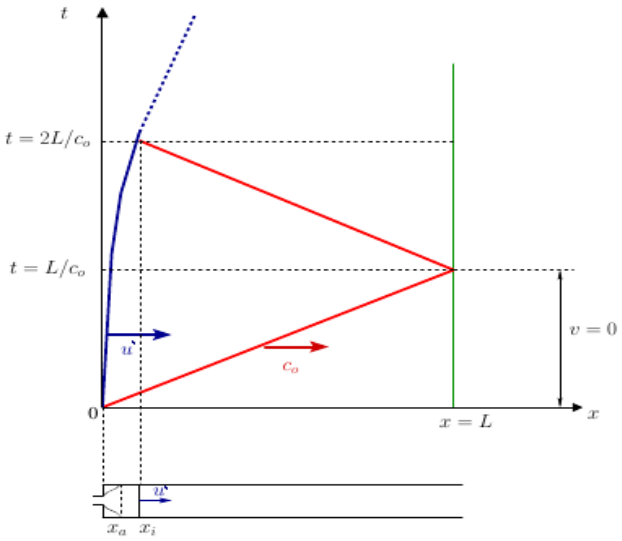

Figure 2.9: Displacement of the acoustic wave which travels at the speed of sound with the displacement of the interface velocity

2.4.2 Experimental Results

In figure 2.12 the delay dt_a of equation 2.7 was taken into account and the time scaled by L. As can be seen, all curves are collapsed except a variation in acceleration for the first peak (more details can be found in Braud and Dyment [2011]). The frequency is a function of the tube length and the shorter the tubes the higher the frequency.

The parameters S_c/S and p_r/p_o influence the exit velocity (figure 2.13 with $p_r/p_o = 4\,bar$ and $L/D = 150$ and figure 2.14 with $S_c/S = 0.03$ and $L/D = 150$). As depicted in figures 2.13 and 2.14, the amplitude of the exit

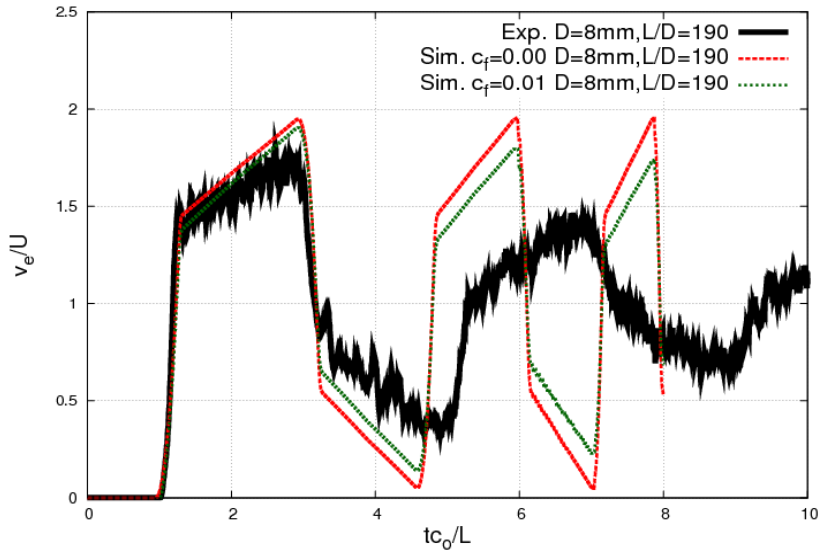

Figure 2.10: Comparison between simulated exit velocity and experimental results

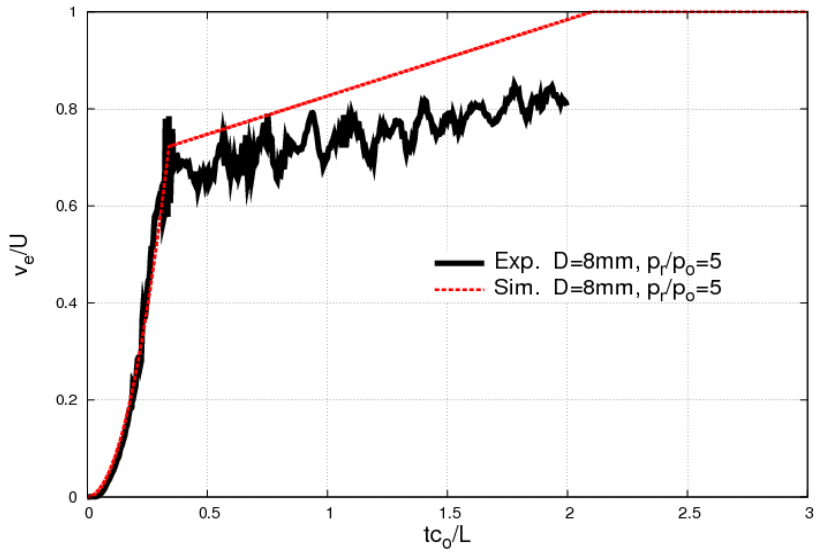

Figure 2.11: Interface velocity used in simulation

velocity depends on the S_c/S and p_r/p_o, therefore higher amplitudes can be obtained with lower S_c/S and lower p_r/p_o.

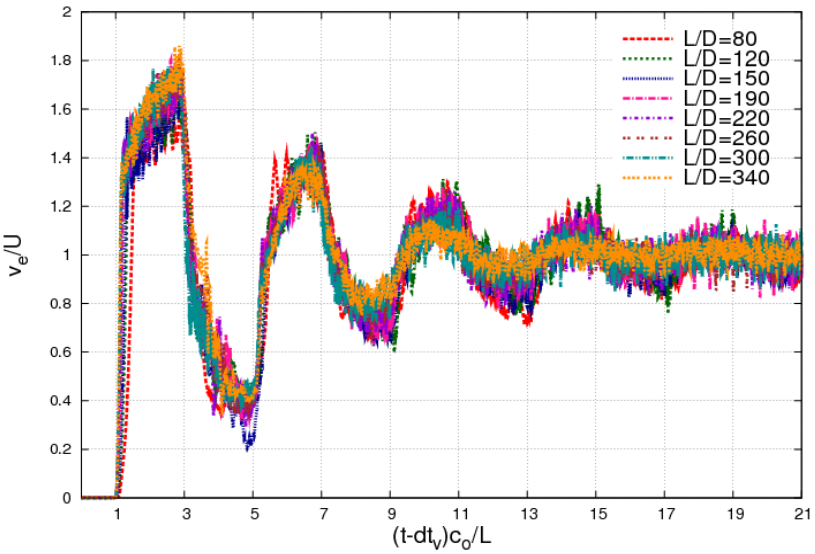

Figure 2.12: Influence of tube length on the exit velocity

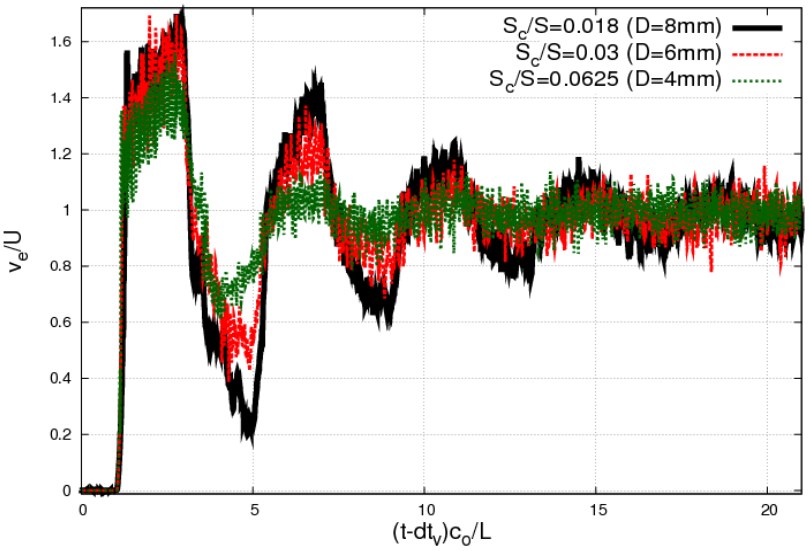

Figure 2.13: Influence of $\frac{S_c}{S}$ on the exit velocity

Figure 2.15 shows the influence of $S_c p_r / S p_o$ on the exit velocity. As predicted, all the curves collapsed. Full demonstration on the effect of this

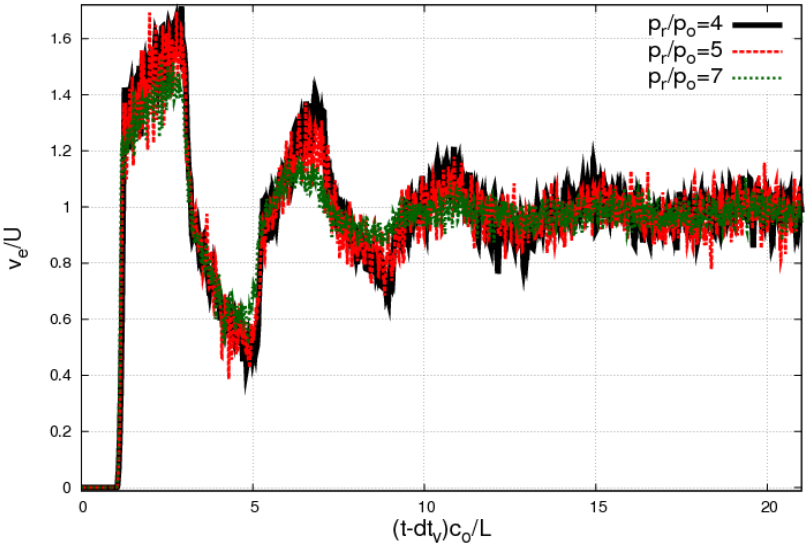

Figure 2.14: Influence of $\frac{p_r}{p_o}$ on the exit velocity

parameter on the exit velocity can be found in Braud and Dyment [2011].

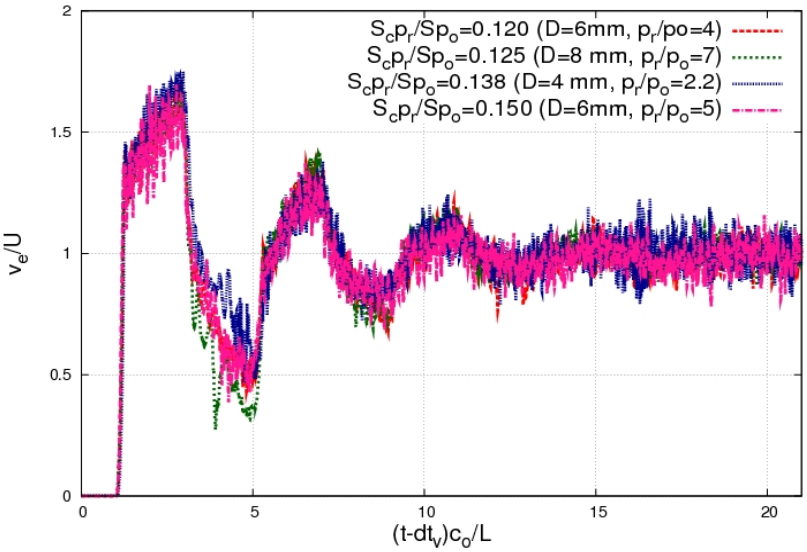

Figure 2.15: Influence of $\frac{S_c}{S}\frac{p_r}{p_o}$ on the exit velocity

2.5 Conclusion

A theoretical model of a steady jet actuator that has been proposed by Braud and Dyment [2011] was satisfactorily validated by experimental results. The model offers the ability to fix and optimize the working conditions of the actuator, according to criteria defined in advance. This is performed by adjusting the dimensionless parameters S/S_c, p_r/p_o and L/c_o.

This will be used is section 4.3 to design the valves for open and closed loop control experiments within the frame work of the model. The perfect knowledge of the actuator dynamics will help to separate it from the controlled dynamics.

Chapter 3

Closed-Loop Control Theory

This chapter provides some control theories to be used for developing a feedback control system for flow separation, as will be explained in the next chapters. They are introduced with an increase of complexity. The first section describes the performance specifications to design the controllers. The second section provides some theoretical basis for the classical PID control. Then the linear quadratic regulator theory is presented. The classical control structure is extended to the robust control structure. The robust H_∞ control theory is then presented.

3.1 Transient Response performance Measures

Figure 3.1 identifies important performance criteria for the transient response. That is, features of the response that may have to meet certain performance specifications. These specifications are defined below:

- Settling time: The time required for the response to come permanently within a 2% band around the steady state value.

- Percentage overshoot: The maximum percentage overshoot over the steady state response.
- Peak time: The time at the maximum peak of the response.
- Rise time: The time at which the response first reaches the steady state level.

These performance measures will be used to compare open and closed loop response, and also closed loop response of various controllers. Our major concern is the settling time. Which is in the present problem, the time from the initial state (i.e separated) to the final state of the flow (i.e attached)as will be discussed later in chapter 5.

3.2 PID control

PID (Proportional Integral Derivative) control is one of the earlier control strategies. It is the most commonly used controller in practice. Also, it has a simple control structure as given in figure 3.2, which was understood by plant operators and which they found relatively easy to tune. If the controller $K(s)$ in figure 3.2 is a PID, then its output u and input e are related by the equation (de Vegte [1994]):

$$u = k_p e + k_i \int e dt + k_d \dot{e} \tag{3.1}$$

where the error is $e = r - y$, with r is the reference and y the system output. The coefficients k_p, k_i and k_d are the proportional, integral and derivative gains respectively. This implies that the transfer function, which is the Laplace transform of the output to input ratio of the controller writes:

$$K(s) = k_p + \frac{k_i}{s} + k_d s = \frac{k_d s^2 + k_p s + k_i}{s} \tag{3.2}$$

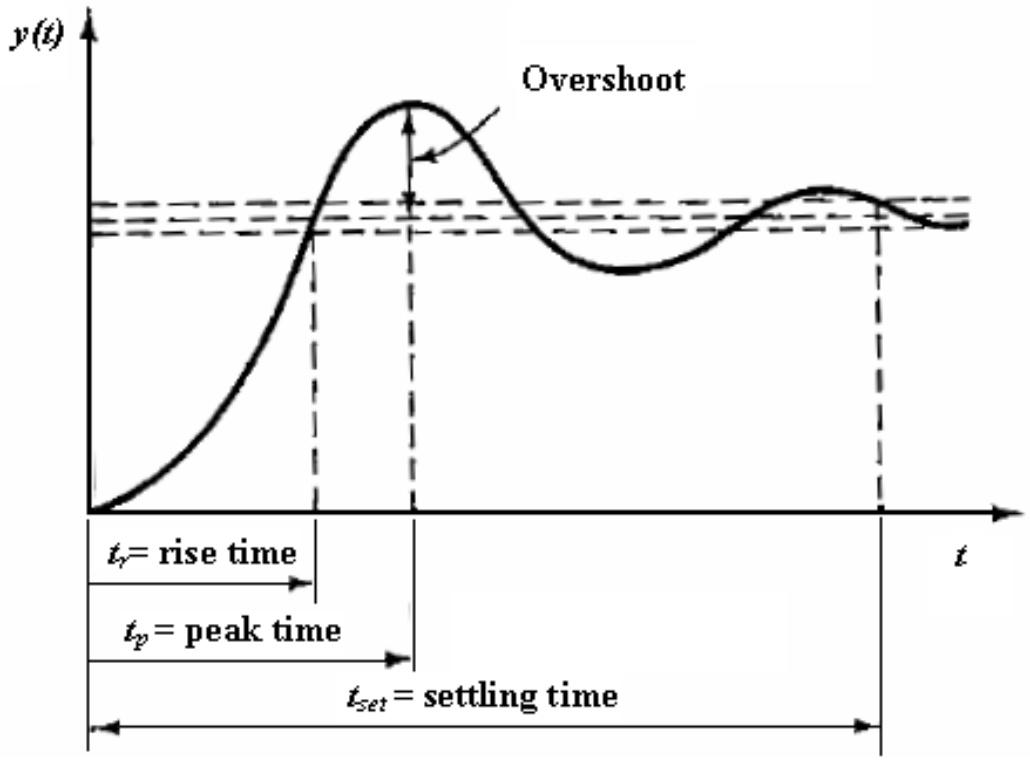

Figure 3.1: Performance criteria (de Vegte [1994]).

A drawback with the derivative action is the high gain for high frequency signals. This means that high frequency measurement noise will generate large variations of the control signal. Therefore, in this work the derivative action will not be used. This lead to:

$$K(s) = k_p + \frac{k_i}{s} = \frac{k_p s + k_i}{s} \tag{3.3}$$

Assume that the considered system is a first order system with the transfer function

$$G(s) = \frac{G_{dc}}{s\tau + 1} \tag{3.4}$$

where G_{dc} is the "DC gain" and τ the time constant of the system.

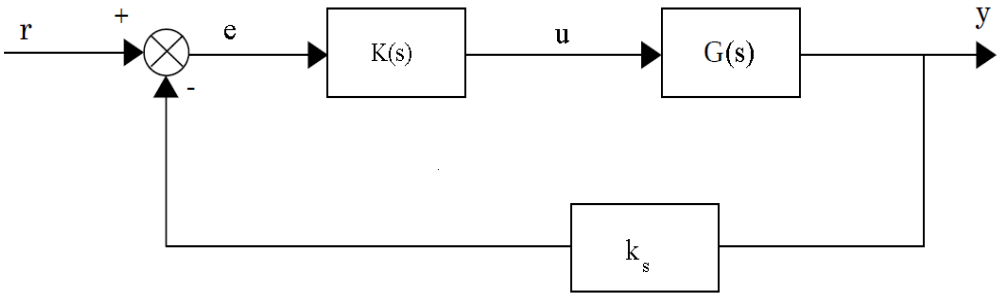

Figure 3.2: General structure of the system with PID controller

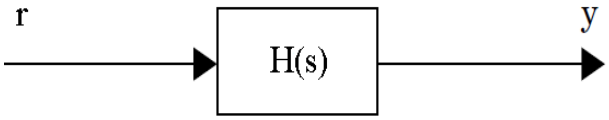

Figure 3.3: Closed-loop transfer function.

Then the general closed-loop transfer function for the system in figure 3.3 is given by:

$$H(s) = \frac{K(s)G(s)}{1 + K(s)G(s)k_s} \tag{3.5}$$

where k_s is the sensor gain. Substituting $K(s)$ and $G(s)$ given in equations 3.3 and 3.4 respectively in the closed-loop transfer function 3.5 gives:

$$H(s) = \frac{\frac{G_{dc}k_p}{\tau}s + \frac{G_{dc}k_i}{\tau}}{s^2 + \frac{G_{dc}k_pk_s+1}{\tau}s + \frac{G_{dc}k_ik_s}{\tau}}$$

Normally $k_s = \frac{1}{G_{dc}}$, which will be assumed all over the present work, then:

$$H(s) = \frac{\frac{G_{dc}k_p}{\tau}s + \frac{G_{dc}k_i}{\tau}}{s^2 + \frac{k_p+1}{\tau}s + \frac{k_i}{\tau}} \tag{3.6}$$

The closed loop system has the characteristic polynomial:

$$s^2 + \frac{k_p + 1}{\tau}s + \frac{k_i}{\tau}$$

Assuming that the desired characteristic polynomial is

$$s^2 + 2\zeta\omega s + \omega^2$$

where the parameter ω determines the response speed and ζ determines the damping. Then the settling time and the percentage overshoot (P.O) can be defined for the underdamped ($0 < \zeta < 1$) second order closed loop system as following (de Vegte [1994]):

$$t_{set} = \frac{4}{\zeta\omega} \tag{3.7}$$

$$P.O = 100 \exp\left(\frac{-\pi\zeta}{\sqrt{1-\zeta^2}}\right) \tag{3.8}$$

The previous relations can be used to design PI controllers based on specific criteria on the settling time or the percentage overshoot.

3.2.1 Steady State Error

When using proportional control only, the system output will have steady state error, which is a crucial drawback of the proportional control. In the following, the steady state error is described. If the controller $K(s)$ in figure 3.2 is a P controller, then we have:

$$E(s) = R(s) - k_s Y(s)$$

$$Y(s) = k_p G(s) E(s)$$

where $E(s)$, $R(s)$ and $Y(s)$ are the Laplace transforms of the error, reference and system output, respectively. Then, combining the previous relations gives the error:

$$E(s) = \frac{R(s)}{1 + k_s k_p G(s)}$$

Assuming a unit step input, $R(s) = \frac{1}{s}$, this leads to:

$$E(s) = \frac{1}{s(1 + k_s k_p G(s))}$$

The steady state error (E_{ss}) can be found directly, without the need for inverse transformation, by the final value theorem:

$$E_{ss} = \lim_{t \to \infty} e(t) = \lim_{s \to 0} sE(s)$$

Then, we have:

$$E_{ss} = \lim_{s \to 0} \frac{1}{1 + k_s k_p G(s)} = \frac{1}{1 + k_s k_p G_{dc}} = \frac{1}{1 + k_p} \tag{3.9}$$

which will be used later to compensate the steady state error by adjusting the reference.

3.2.2 Discrete PI Controller

In experiments, a digital form of PI controller will be used, by implementing finite difference approximation based on the differential form of equation 3.1

$$\dot{u} = k_i e + k_p \dot{e} \tag{3.10}$$

Then, by using backward differences,

$$\begin{aligned} \tfrac{(u_k - u_{k-1})}{T} &= k_i e_k + k_p \tfrac{e_k - e_{k-1}}{T} \\ u_k &= u_{k-1} + (k_p + k_i T) e_k - k_p e_{k-1} \end{aligned} \tag{3.11}$$

where T is the integration time and the subscript k is the discrete time variable.

3.2.3 PID Tuning

PID tuning is necessary to adjust the parameters of the controller so that the control system exhibits the desired property. Manual PID tuning can

Controller	k_p	k_i	k_d
P	$0.5k_u$	-	-
PI	$0.45k_u$	$0.54\ \frac{k_u}{T_u}$	-
PID	$0.6k_u$	$1.2\ \frac{k_u}{T_u}$	$4.8\ \frac{k_u}{T_u}$

Table 3.1: Ziegler-Nichols' ultimate-cycle method (de Vegte [1994]).

be a choice, but on the other hand it can consume a lot of time to have a desirable response. A very useful empirical tuning formula was proposed by Ziegler and Nichols in early 1942, "the Ultimate-Cycle Method" which was designed for a step response overshoot of about 25%. This method is based on experiments analysis and it is convenient if the mathematical model of the plant is not available. In this method, only proportional control is used for tuning, the gain k_p is increased to the critical or ultimate gain k_u, where the output shows sustained oscillations of measured period T_u. The controller settings are then suggested as given in table 3.1.

There are many more methods for PID tuning which are beyond the scope of this study. But PID control does not take into account the control effort of the controller, which is a major concern in the present case. In the following section, optimal control is discussed, in which one can optimize the controller gains while minimizing the control effort or the settling time.

3.3 Linear Quadratic Regulator (LQR)

Optimal control is one of the main techniques for controller design in state space representation. In optimal control, the control is sought such that it gives the best trade-off between performance and cost of control. Optimal

design can be carried out for both open-loop and closed-loop systems. A standard form of the closed-loop case is to seek the control that minimizes the values of a performance index J of the form

$$J = \int_0^\infty (x^T Q x + u^T R u) \tag{3.12}$$

Q and R are weighting matrices usually diagonal. The terms $x^T Q x$ and $u^T R u$ of the integrand are quadratic forms that measure the performance and the control cost respectively. The choice of the elements of Q and R allows the relative weighting of individual state variables and individual control inputs, as well as the relative weighting of state variables and control inputs. Increasing R relative to Q, increases the weighting on the control and has the effect of reducing the control inputs at the expense of the response. The choice of Q and R requires considerable trial and error until the transient response is satisfactory (de Vegte [1994]). But in the scalar case the selection is much easier.

Theorem 3.3.1 *Optimal Regulator Theorem: Consider the system*

$$\begin{aligned} \dot{x} &= Ax + Bu \\ y &= Cx \end{aligned} \tag{3.13}$$

The optimal control is a constant-gain state feedback

$$\begin{aligned} u_{opt} &= -Kx \\ K &= R^{-1} B^T P \end{aligned} \tag{3.14}$$

where P is a symmetric and positive definite matrix obtained as the solution of the algebraic matrix Riccati equation

$$PA + A^T P + Q - PBR^{-1}B^T P = 0 \tag{3.15}$$

And, under mild restrictions, gives a stable closed-loop system. (de Vegte [1994])

Here, $x \in \mathbb{R}^n$ is the state vector, $u \in \mathbb{R}^p$ the control vector, $y \in \mathbb{R}^q$ the output vector, $A \in \mathbb{R}^{n \times n}$ is the system matrix, $B \in \mathbb{R}^{n \times p}$ is the input matrix, and $C \in \mathbb{R}^{n \times q}$ is the output matrix.

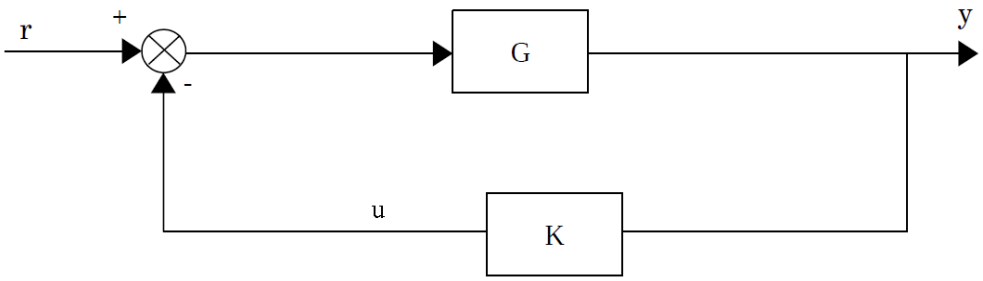

Figure 3.4: structure of the system with LQR controller

The previous control structures for the PID and LQR controller does not take into account the measured signal noise and the external disturbances. These disturbances are included in the robust control structure that will be discussed in the next section.

3.4 H_∞ Control

In this section we consider H_∞ control theory. Specifically, the suboptimal H_∞ control problem is solved using two approaches; Ricatti-based and LMI-based approach. The LMI-based approach is computationally more involved for large problems, and it has the merit of eliminating the regularity restrictions attached to the Riccati-based solution (Gahinet et al. [1995]). The robust control structure is formulated thoroughly. Then, the H_∞ controller is solved for both approaches.

Two important definitions will be listed below

Optimal H_∞ Control: Find all admissible controllers $K(s)$ such that

$\|T_{zw}\|_\infty$ is minimized. Where $\| \ \|_\infty$ is the infinity norm defined in Appendix A. The closed loop transfer function T_{zw} will be defined in the next paragraph.

Suboptimal H_∞ Control: Given $\gamma > 0$, find all admissible controllers $K(s)$, if there is any, such that $\|T_{zw}\|_\infty < \gamma$ (Zhou and Doyle [1999]).

3.4.1 Problem Formulation

The conventional block diagram in figure 3.2 does not show the disturbances that act on the system, nor does it explicitly show which signals are of interest, this is side information in a conventional description of the control problem. To cast the classical control in this framework, we first add inputs corresponding to disturbances and outputs indicating the signals of importance to us. One way to do this is shown in figure 3.5, this control structure is often called the classical one degree of freedom (1-DOF) controller (Boyd and Barratt [1991]).

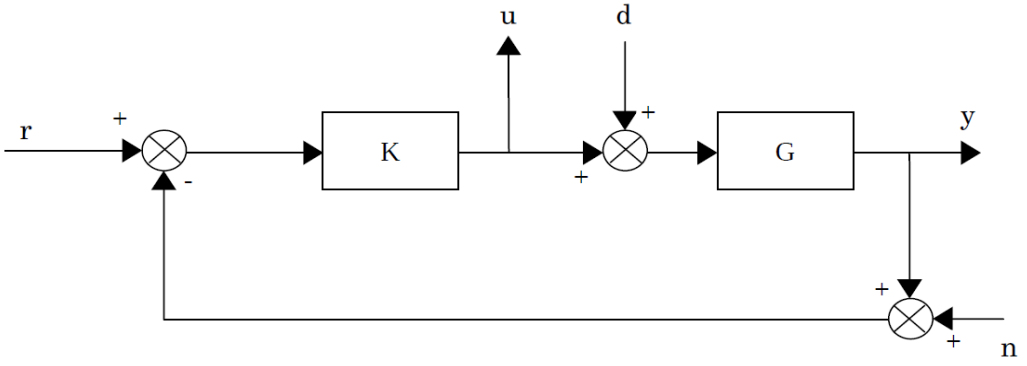

Figure 3.5: structure of the system with H_∞ controller

The basic goal in the design of the (1-DOF) control system is to keep the system output y close to the reference signal r despite the disturbance d and the sensor noise n while ensuring that the actuator signal u is not too large.

A feedback control system can be rearranged as a Linear Fractional Transformation (LFT) as shown in figure 3.6. LFT is a useful way to standardize block diagrams for robust control analysis and design.

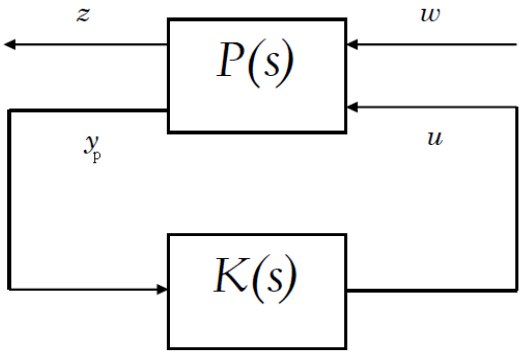

Figure 3.6: LFT scheme of the system

$$\begin{bmatrix} z \\ y_p \end{bmatrix} = [P] \begin{bmatrix} w \\ u \end{bmatrix} \Rightarrow \begin{bmatrix} z \\ y_p \end{bmatrix} = \begin{bmatrix} P_{11} & P_{12} \\ P_{21} & P_{22} \end{bmatrix} \begin{bmatrix} w \\ u \end{bmatrix} \tag{3.16}$$

$$u = Ky_p \tag{3.17}$$

where $P(s)$ is the generalized plant and $K(s)$ is the controller. The reference input r, the disturbance d and sensor noise n are the exogenous inputs. So we take the exogenous input vector w to be:

$$w = \begin{bmatrix} d \\ n \\ r \end{bmatrix}$$

We take the vector of regulated outputs z to consist of the system output y and the actuator signal u

$$z = \begin{bmatrix} y \\ u \end{bmatrix}$$

The control input is u, while the measured output y_p will be:

$$y_p = r - y - n$$

The plant has four inputs (d, n, r and u) and three outputs (y, u and y_p). Its transfer matrix is

$$P = \begin{bmatrix} P_{11} & P_{12} \\ P_{21} & P_{22} \end{bmatrix} = \begin{bmatrix} P_{zw} & P_{zu} \\ P_{yw} & P_{yu} \end{bmatrix} = \left[\begin{array}{ccc|c} G & 0 & 0 & G \\ 0 & 0 & 0 & 1 \\ \hline -G & -1 & 1 & -G \end{array}\right] \tag{3.18}$$

Where for example, the P_{zw} is the transfer function from w to z. Then, the closed loop transfer matrix T_{zw} now has three inputs and two outputs:

$$T_{zw} = P_{11} + P_{12}K(I - P_{22}K)^{-1}P_{21} \tag{3.19}$$

$$T_{zw} = \begin{bmatrix} \frac{G}{1+GK} & -\frac{GK}{1+GK} & \frac{GK}{1+GK} \\ -\frac{GK}{1+GK} & -\frac{K}{1+GK} & \frac{K}{1+GK} \end{bmatrix} = \begin{bmatrix} SG & -T & T \\ -T & -KS & KS \end{bmatrix} \tag{3.20}$$

where $L = GK$ is the loop gain, $S = 1/(1 - L)$ is the sensitivity transfer function and $T = 1 - S$ is the complementary sensitivity transfer function.

State Space Representation

The general plant P takes two vectors of input signals (w and u) and produces two vectors of output signals (z and y_p). To develop the matrices, let subscripts p and c denote the plant and the controller, respectively. A state space realization of the plant is thus:

$$\begin{aligned} \dot{x}_p &= Ax_p + B_1 w + B_2 u \\ z &= C_1 x_p + D_{11} w + D_{12} u \\ y_p &= C_2 x_p + D_{21} w + D_{22} u \end{aligned} \tag{3.21}$$

So that with $(x(0) = 0)$,

$$P(s) = \begin{bmatrix} P_{11}(s) & P_{12}(s) \\ P_{21}(s) & P_{22}(s) \end{bmatrix} = C_p(sI - A_p)^{-1}B_p + D_p \tag{3.22}$$

Where,

$$A_p = A$$

$$B_p = \begin{bmatrix} B_1 & B_2 \end{bmatrix}$$

$$C_p = \begin{bmatrix} C_1 \\ C_2 \end{bmatrix}$$

$$D_p = \begin{bmatrix} D_{11} & D_{12} \\ D_{21} & D_{22} \end{bmatrix}$$

In this plant P, D_{22}=0. Such a plant is called strictly proper. Suppose that the controller has the state space realization

$$\begin{aligned} \dot{x_c} &= A_c x_c + B_c y_p \\ u &= C_c x_c + D_c y_p \end{aligned} \tag{3.23}$$

So that

$$K(s) = C_c(sI - A_c)^{-1}B_c + D_c \tag{3.24}$$

Then, by assembling and eliminating u and y_p from equations 3.21 and 3.23, a state space realization of the closed loop system can be found in compact form,

$$\begin{bmatrix} \dot{x_p} \\ \dot{x_c} \end{bmatrix} = \begin{bmatrix} A + B_2 D_c C_2 & B_2 C_c \\ B_c C_2 & A_c \end{bmatrix} \begin{bmatrix} x_p \\ x_c \end{bmatrix} + \begin{bmatrix} B_1 + B_2 D_c D_{21} \\ B_c D_{21} \end{bmatrix} w$$

$$z = \begin{bmatrix} C_1 + D_{12} D_c C_2 & D_{12} \end{bmatrix} \begin{bmatrix} x_p \\ x_c \end{bmatrix} + \begin{bmatrix} D_{11} + D_{12} D_c D_{21} \end{bmatrix} w$$

or simply

$$\begin{aligned} \dot{x} &= A_{cl}x + B_{cl}w \\ z &= C_{cl}x + D_{cl}w \end{aligned} \tag{3.25}$$

where

$$\begin{aligned} A_{cl} &= \bar{A} + \bar{B}\bar{G}M, \quad B_{cl} = \bar{D} + \bar{B}\bar{G}E \\ C_{cl} &= \bar{C} + H\bar{G}M, \quad D_{cl} = F + H\bar{G}E \end{aligned} \tag{3.26}$$

$$\bar{A} = \begin{bmatrix} A_p & 0 \\ 0 & 0 \end{bmatrix}, \quad \bar{B} = \begin{bmatrix} B_2 & 0 \\ 0 & I \end{bmatrix}, \quad M = \begin{bmatrix} C_2 & 0 \\ 0 & I \end{bmatrix}, \quad E = \begin{bmatrix} D_{21} \\ 0 \end{bmatrix}, \quad x = \begin{bmatrix} x_p \\ x_c \end{bmatrix}$$

$$H = \begin{bmatrix} D_{12} & 0 \end{bmatrix} \quad \bar{D} = \begin{bmatrix} B_1 \\ 0 \end{bmatrix}, \quad \bar{G} = \begin{bmatrix} D_c & C_c \\ B_c & A_c \end{bmatrix}, \quad \bar{C} = \begin{bmatrix} C_1 & 0 \end{bmatrix}, \quad F = D_{11}$$

and the vector dimensions are:

$x_p \in \mathbb{R}^{n_p}$, $x_c \in \mathbb{R}^{n_c}$, $y \in \mathbb{R}^{n_y}$, $z \in \mathbb{R}^{n_z}$, $w \in \mathbb{R}^{n_w}$, $u \in \mathbb{R}^{n_u}$, $x \in \mathbb{R}^{n_x}$, $n_x = n_p + n_c$

3.4.2 H_∞ Controller Design

In this section, only important theorems for the existence conditions of the H_∞ controllers are stated, much more details can be found in Zhou and Doyle [1999] and Skelton et al. [1998].

Riccati-Based Approach

Consider the system 3.21, in which the following assumptions are satisfied:

(i) (A, B_1) is controllable and (C_1, A) is observable
(ii) (A, B_2) is stabilizable and (C_2, A) is detectable
(iii) $D_{12}^T \begin{bmatrix} C_1 & D_{12} \end{bmatrix} = \begin{bmatrix} 0 & I \end{bmatrix}$
(iv) $\begin{bmatrix} B_1 \\ D_{21} \end{bmatrix} D_{21}^T = \begin{bmatrix} 0 \\ I \end{bmatrix}$

These assumptions simplify the theorem statements and proofs, and can

be relaxed. Two additional assumptions that are implicit in the assumed realization for $P(s)$ are that $D_{11} = 0$ and $D_{22} = 0$. However, relaxing the assumption $D_{11} = 0$ complicates the formulas substantially.

Theorem 3.4.1 *$\exists$ an admissible controller K such that $\|T_{zw}\|_\infty < \gamma$ if and only if the following three conditions hold: (Zhou and Doyle [1999])*

(i) $\exists X_\infty > 0$ *such that:*

$$X_\infty A + A^T X_\infty + X_\infty (B_1 B_1^T/\gamma^2 - B_2 B_2^T) X_\infty + C_1^T C_1 = 0$$

(ii) $\exists Y_\infty > 0$ *such that:*

$$AY_\infty + Y_\infty A^T + Y_\infty (C_1^T C_1/\gamma^2 - C_2^T C_2) Y_\infty + B_1 B_1^T = 0$$

(iii) $\rho(X_\infty Y_\infty) < \gamma^2$

$$K_{sub}(s) := \begin{bmatrix} \hat{A}_\infty & -Z_\infty L_\infty \\ F_\infty & 0 \end{bmatrix}$$

where

$\hat{A}_\infty = A + \gamma^{-2} B_1 B_1^T X_\infty + B_2 F_\infty + Z_\infty L_\infty C_2$

$F_\infty = -B_2^T X_\infty$, $L_\infty = -Y_\infty C_2^T$

$Z_\infty = (I - \gamma^{-2} Y_\infty X_\infty)^{-1}$.

LMI-Based Approach

Theorem 3.4.2 *Let a scalar $\gamma > 0$ be given and consider the system 3.21. Then the following statements are equivalent: (Skelton et al. [1998])*

(i) There exists a controller of order n_c which stabilizes the system and yields $\|T_{zw}\|_\infty < \gamma$.

(ii) There exists a matrix pair $(X, Y) \in \Re^{(n_p+n_c)\times(n_p+n_c)} \times \Re^{(n_p+n_c)\times(n_p+n_c)}$ such that

$$X > 0,\ Y > 0,\ XY = \gamma^2 I$$

$$\begin{bmatrix} \bar{B} \\ H \end{bmatrix}^{\perp} \begin{bmatrix} \bar{A}X + X\bar{A}^T + \bar{D}\bar{D}^T & X\bar{C}^T + \bar{D}F^T \\ \bar{C}X + F\bar{D}^T & FF^T - \gamma^2 I \end{bmatrix} \begin{bmatrix} \bar{B} \\ H \end{bmatrix}^{\perp T} < 0$$

$$\begin{bmatrix} M^T \\ E^T \end{bmatrix}^{\perp} \begin{bmatrix} Y\bar{A} + \bar{A}^T Y + \bar{C}^T\bar{C} & Y\bar{D} + \bar{C}^T F \\ \bar{D}^T Y + F^T\bar{C} & F^T F - \gamma^2 I \end{bmatrix} \begin{bmatrix} M^T \\ E^T \end{bmatrix}^{\perp T} < 0$$

(iii) There exists a matrix pair $(X_p, Y_p) \in \Re^{n_p\times n_p} \times \Re^{n_p\times n_p}$ such that

$$\begin{bmatrix} X_p & \gamma I \\ \gamma I & Y_p \end{bmatrix} > 0$$

$$\begin{bmatrix} B_2 \\ D_{12} \end{bmatrix}^{\perp} \begin{bmatrix} AX_p + X_pA^T + B_1B_1^T & X_pC_1^T + B_1D_{11}^T \\ C_1X_p + D_{11}B_1^T & D_{11}D_{11}^T - \gamma^2 I \end{bmatrix} \begin{bmatrix} B_2 \\ D_{12} \end{bmatrix}^{\perp T} < 0$$

$$\begin{bmatrix} C_2^T \\ D_{21}^T \end{bmatrix}^{\perp} \begin{bmatrix} Y_pA + A^TY_p + C_1^TC_1 & Y_pB_1 + C_1^TD_{11} \\ B_1^TY_p + D_{11}^TC_1 & D_{11}^TD_{11} - \gamma^2 I \end{bmatrix} \begin{bmatrix} C_2^T \\ D_{21}^T \end{bmatrix}^{\perp T} < 0$$

In this case, all such controllers are given by

$$\bar{G} = -R^{-1}\Gamma^T\Phi\Lambda^T(\Lambda\Phi\Lambda^T)^{-1} + S^{1/2}L(\Lambda\Phi\Lambda^T)^{-1/2}$$

where L is an arbitrary matrix such that $\|L\| < 1$ and R is an arbitrary positive definite matrix such that $\Phi = (\Gamma R^{-1}\Gamma^T - \Theta)^{-1} > 0$ and $S = R^{-1} - R^{-1}\Gamma^T[\Phi - \Phi\Lambda^T(\Lambda\Phi\Lambda^T)^{-1}\Lambda\Phi]\Gamma R^{-1}$,

$$\Theta = \begin{bmatrix} Y\bar{A} + \bar{A}^TY & Y\bar{D} & \bar{C}^T \\ \bar{D}^TY & -\gamma^2 I & F^T \\ \bar{C} & F & -I \end{bmatrix}, \qquad \Gamma = \begin{bmatrix} Y\bar{B} \\ 0 \\ H \end{bmatrix}, \qquad \Lambda = \begin{bmatrix} M & E & 0 \end{bmatrix}$$

Consider $\Omega \in \mathbb{R}^{m\times n}$, then $\Omega^{\perp}$ is a non unique matrix such that $\Omega^{\perp}\Omega = 0$ and $\Omega^{\perp}\Omega^{\perp T} > 0$

All the theorems stated in this chapter will be used to design the controllers in chapter 6.

Chapter 4

Experimental Setup

In this chapter the description the experimental set-up used for both open-loop and closed-loop control experiments is explained. It first describe the LML wind tunnel and the flow characterization. Then, it gives a detailed description of the tested model for the separation control experiments. The actuators and sensor in this work described. Finally, the acquisition and control system is explored.

4.1 LML wind tunnel

The experiments were conducted in the LML boundary layer Wind Tunnel in the Lille Mechanics Lab (LML). The LML wind tunnel has been extensively described and characterized in Carlier and Stanislas [2005]. A sketch of the facility is shown in figure 4.1. The working section of the wind tunnel is $1\,m$ high, $2\,m$ wide and $21.6\,m$ long. The flow is produced by a fan and motor that allow the variation of the mean velocity of the external flow continuously from $3\,m/s$ up to $10\,m/s$ with a stability better than 0.5%. The turbulence level in the free stream is about 0.3% of the external velocity

Re_θ	U_∞ (m/s)	θ (m)	δ^+	u_τ (m/s)	δ (m/s)	1^+ (ν/u_τ) (um)	P_x (Pa/m)
7630	3	0.0362	2590	0.112	0.332	128	-0.090
10140	5	0.0291	3620	0.185	0.279	77	-0.200
13420	7	0.0276	5020	0.255	0.281	56	-0.350
18950	10	0.0280	6860	0.350	0.288	42	-0.540

Table 4.1: properties of the boundary layer in the LML wind-tunnel at $x = 18m$ obtained from single wire HWA

U_∞, and the temperature is kept within $\pm 0.2C^\circ$ by using an air-water heat exchanger in the plenum chamber. The last five meters of the working section are made up of glass to give full optical access to the flow. The turbulent boundary layer under study develops on the lower wall of the working section after being tripped at the entrance by a grid fixed on the floor. Due to the long length of the working section ($21.6\,m$ at most), this facility is suitable for high spatial resolution measurements at high Reynolds numbers: the Reynolds number based on the momentum thickness Re_θ can reach values up to 20600, with a boundary layer thickness of about $0.3\,m$. The boundary layer has been previously characterized with hot-wire anemometry at two measurement station: $x = 18\,m$ and $x = 19.6\,m$ downstream of the tripping device. The measurements at $x = 18\,m$ were realized using single-wire probes only, and those at $x = 19.6\,m$ using both single-wire and X-wire probes. The characteristics of the boundary layer at these two measurement stations are reported in tables (4.1) and (4.2).

4.2 The Ramp Model

The Model added in the wind tunnel for separation control purpose has been thoroughly described and characterized by Cuvier et al. [2010]. This model,

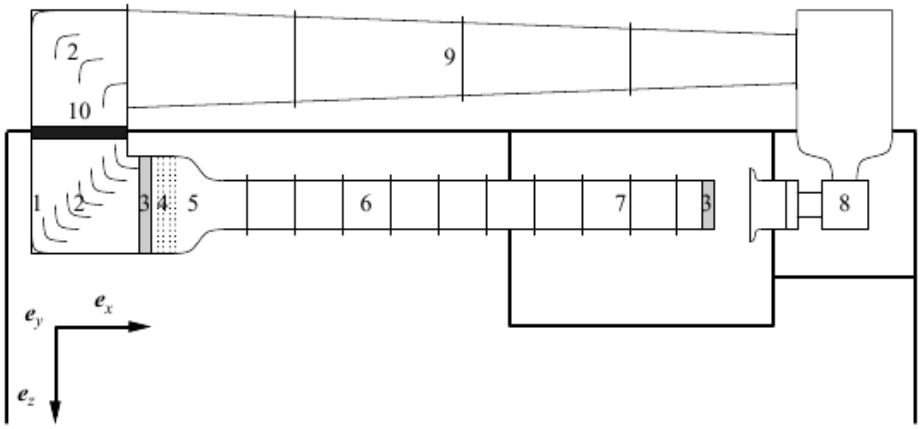

Figure 4.1: LML wind-tunnel, 1- plenum chamber; 2- guide vanes; 3- honeycomb; 4- grids; 5- contraction; 6- turbulent boundary layer developing zone; 7- testing zone of wind tunnel; 8- fan and motor; 9- return circuit; 10- heat exchanger (air-water).

which was built for the European project AVERT, consists of four parts as depicted in figure 4.2. First, a smooth converging part with a contraction ratio of 0.75, pointed to generate an adverse pressure gradient. The second part is an articulated flat plate used to tune the pressure gradient, that can rotate from $\alpha = 2^\circ$ to $\alpha = -4^\circ$ around its leading edge. For $\alpha = 0^\circ$ the flat plate is parallel to the streamwise direction. For positive values of α

Re_θ	U_∞ (m/s)	θ (m)	δ^+	u_τ (m/s)	δ (m/s)	1^+ (ν/u_τ) (um)	P_x (Pa/m)
8170	3	0.041	2570	0.110	0.350	136	-0.090
11450	5	0.034	3890	0.183	0.319	82	-0.200
14500	7	0.031	4970	0.252	0.298	60	-0.350
20920	10	0.031	7070	0.347	0.304	43	-0.540

Table 4.2: properties of the boundary layer in the LML wind-tunnel at $x = 19m$ obtained from single wire HWA

the boundary layer tends to develop towards favorable pressure gradients. For negative values of α, adverse pressure gradients are realized. This flat plate is made of four plates. One of them is composed of six interchangeable inserts ($625 \times 135\, mm^2$) in which actuators were mounted. The third part is again an articulated flat plate called later "flap". It can rotate from $\beta = -5°$ to $\beta = -40°$ around its leading edge. For $\beta = -5°$ the flap is parallel to the streamwise direction. The aim of this part is to fix the separation when it exists. By increasing the absolute value of β, the adverse pressure gradient is increased. Therefore, it can modify the extend of an existing separation or initiate one. This flap is made of three interchangeable inserts ($625 \times 240\, mm^2$) where sensors were mounted. Finally, the fourth part of the model consists of a flexible sheet of PVC that is shaped to obtain a smooth transition with the wind tunnel floor.

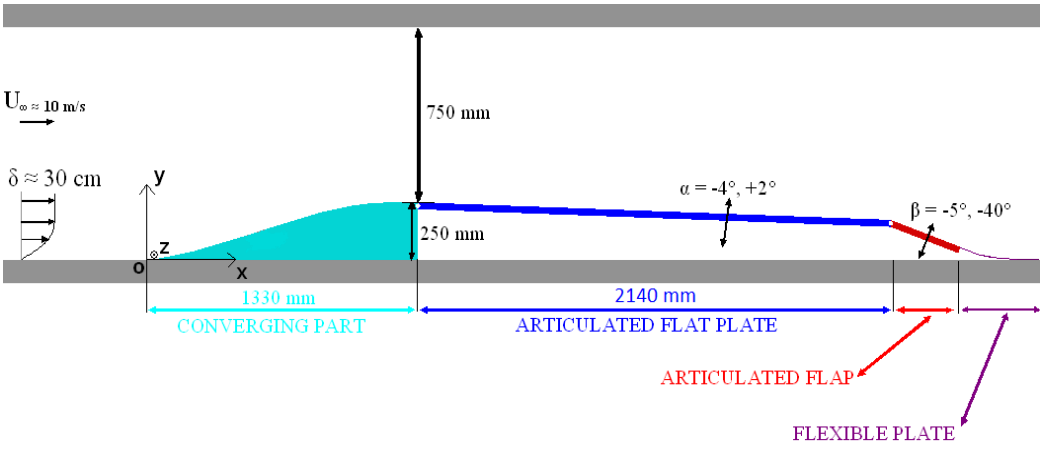

Figure 4.2: schematic view of the model

In the present study, the parameters α and β were fixed to $-2°$ and $-22°$ respectively. For these angles an adverse pressure gradient is imposed to the boundary layer before separation as shown in figure 4.4, and the flow is

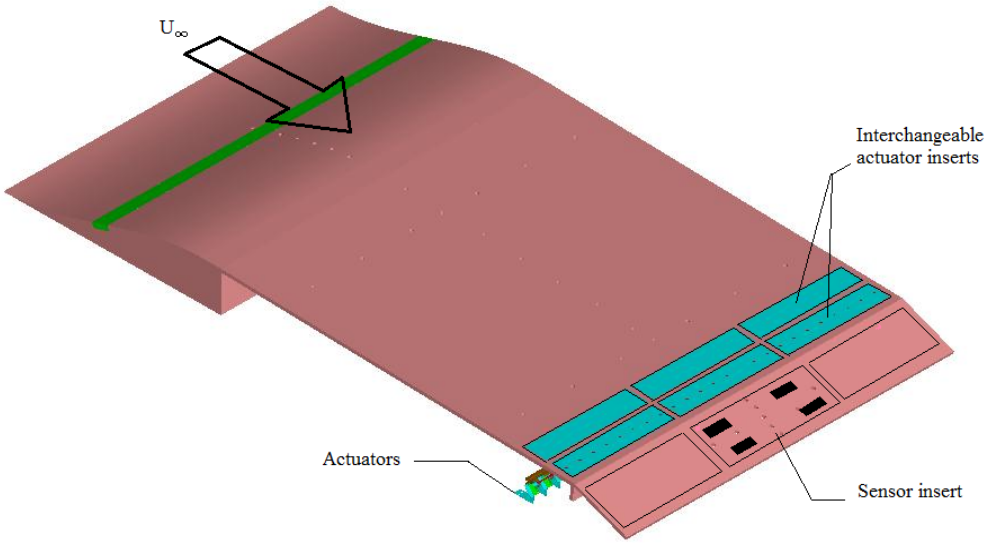

Figure 4.3: Isometric view of the model

separated on the flap. The transverse homogeneity was checked by Cuvier et al. [2010] within 80% on the flat plate using pressure taps, also the separation was checked to be 2D within 70% of the flap span. The boundary layer characteristics on the flat plat of the model at $U_\infty = 10m/s$ was checked by Cuvier et al. [2010] using hot wire probes at five stations as depicted in figure 4.5.

4.3 Fluidic Actuators

In this section the design and the set-up of the actuator is explained. The air supply and the measuring devices are described. This section section gives a brief description of the actuator and it's working range.

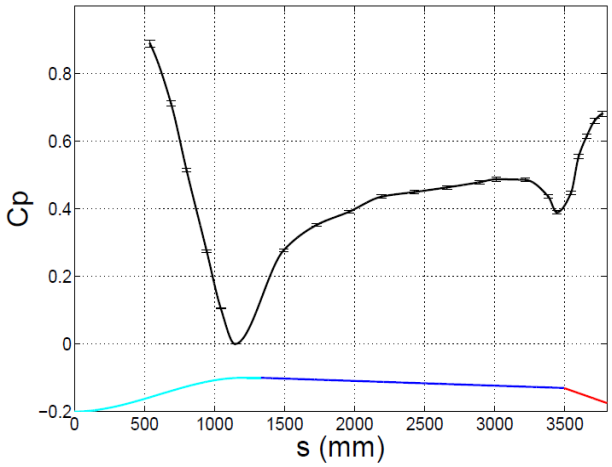

Figure 4.4: Pressure coefficient distribution along the model for $U_\infty = 10m/s$, $\alpha = -2$ and $\beta = -22$ (Cuvier et al. [2010])

4.3.1 Design

The actuator described in chapter 2 consists mainly from a tube, throat and FESTO valve. The tube is $20\,cm$ length with $L/D = 33.3$. The time delay corresponds to this tube length is $1.5\,ms$ that can be seen easily in figure 2.8. For tubes with $L/D < 40$, the reflected wave interacts with the jet before it touches the tube, which make the first peak cut before it reaches its maximum, this mean that the transient behavior described in chapter 2 at the exit of the jet is significantly damped (Braud and Dyment [2011]). The throat were used in the flow control experiments can be seen in figure 4.6, with two nozzle diameters $D = 0.8\,mm$ and $D = 1.3\,mm$ to cover different ranges of the exit velocity as shown in table 4.3 (computed using equation 2.5). Further details on the throat can be found in subsection 2.2.1.

Figure 4.7 shows the Festo valve mounted on small reservoir that is connected to the input pressure line, while the throat with the tube are connected to exit of the valve.

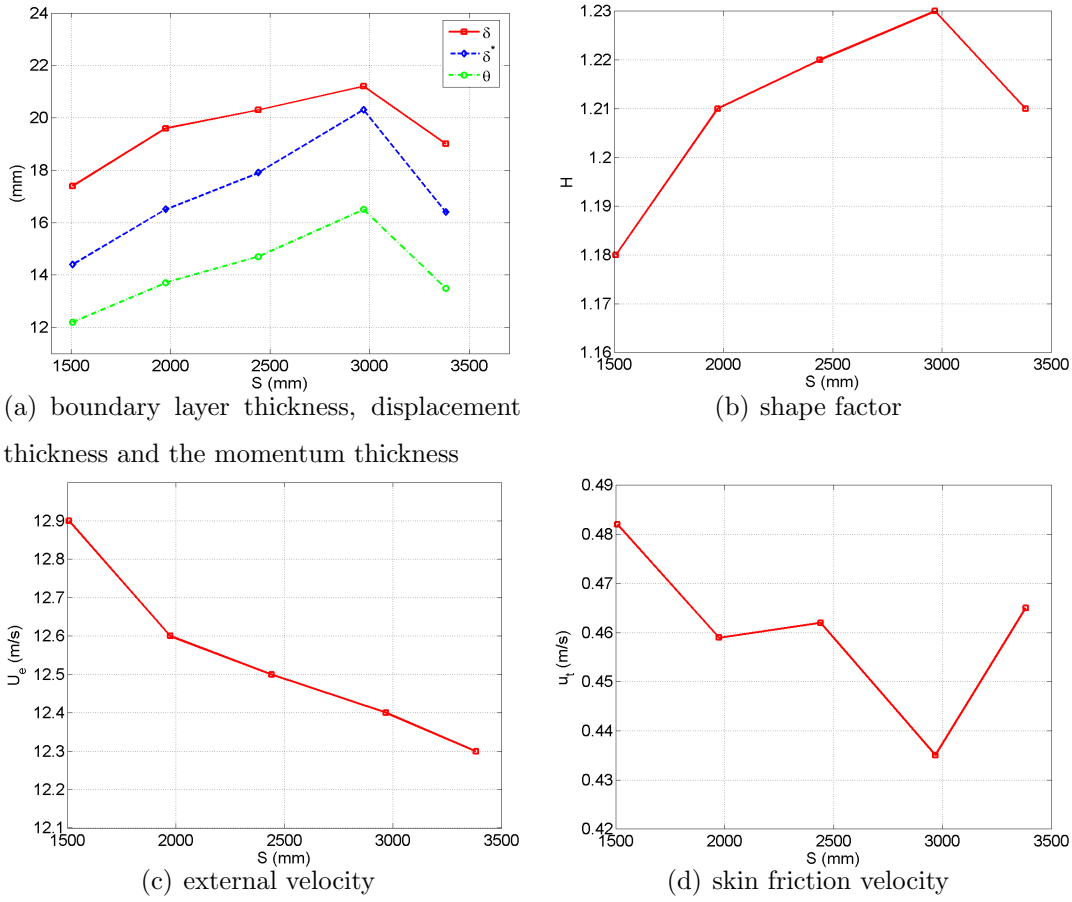

(a) boundary layer thickness, displacement thickness and the momentum thickness

(b) shape factor

(c) external velocity

(d) skin friction velocity

Figure 4.5: Boundary layer characteristics along the model at $U_\infty = 10m/s$, $\alpha = -2$ and $\beta = -22$, Cuvier et al. [2010]

4.3.2 Set-up

The actuators were mounted on interchangeable plates in order to have a wide range of configurations, such as blowing down stream, upstream, perpendicular to the flow, blowing at specific angle,..., etc. In the present work, only one configuration was used. Three interchangeable plates were installed on the flat plate of the model, having 8 holes each, in which a tube of internal diameter $\Phi = 6\,mm$ was installed. The hole was drilled at angles

Throat Diameter	$D = 0.8\,mm$	$D = 1.3\,mm$
$\frac{S}{S_c}$	56.25	21.3
Pressure(bar)	Velocity (m/s)	Velocity (m/s)
7	24.5	64.5
2	7	18.5

Table 4.3: Exit jet velocity ranges for the two throat diameters with respect to the working pressure

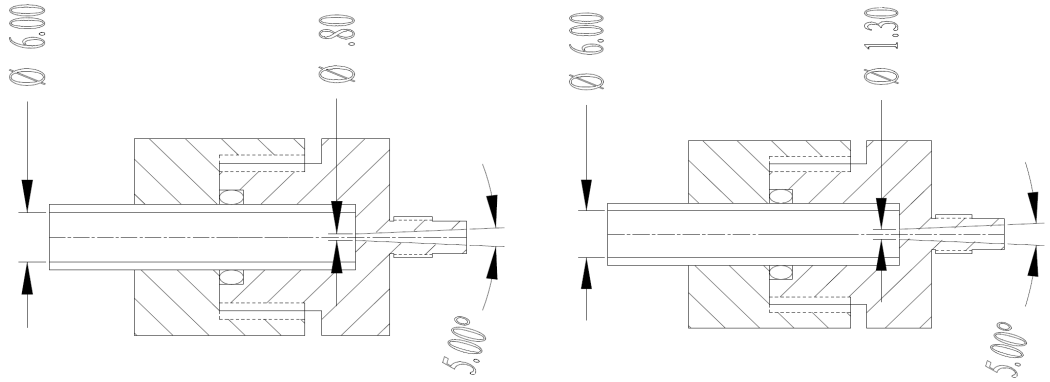

(a) Throat with $\frac{S}{S_c} = 56.25$ (b) Throat with $\frac{S}{S_c} = 21.3$

Figure 4.6: The two throats used in the separation control experiments

$\alpha = 135°$ and $\beta = 45°$. The actuators were distributed spanwise, spaced by $\lambda/\Phi = 13.6$ and located at $\Delta X_{VG}/\Phi = 47$ from the separation line, which is the intersection between the flat plate and the flap. The previous parameters were chosen to match the optimal parameters found by Cuvier et al. [2010]. Flexible tubes were mounted in these holes, while the other side was connected to the throat as depicted in figure 4.8. In summery, 22 co-rotating jets blowing at 45° and upstream have been installed.

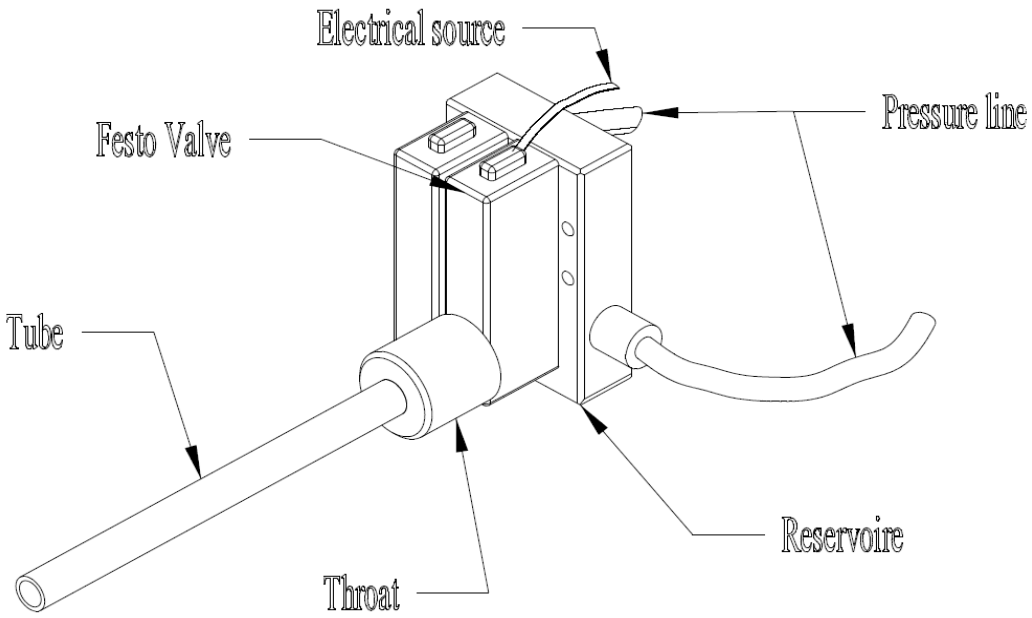

Figure 4.7: scheme of the actuator used in the separation control experiments

Figure 4.8: Actuators installed on the interchangeable plates

4.3.3 Supply air

A $75\,kW$ compressor delivers $880\,m^3/h$ at $7.5\,bars$ (gauge) in a $2\,m^3$ tank. Before this tank, the compressed air is filtered and passes through dryer so that it is exempted of water and particles. The system is automatically purged. The compressor regulates the pressure in the tank between 6.5 and $7.5\,bars$ (gauge). The $2\,inch$ output of the tank is connected to a pressure regulator, which can regulate the pressure between 0.5 and $12\,bars$ (gauge). (see figure 4.9)

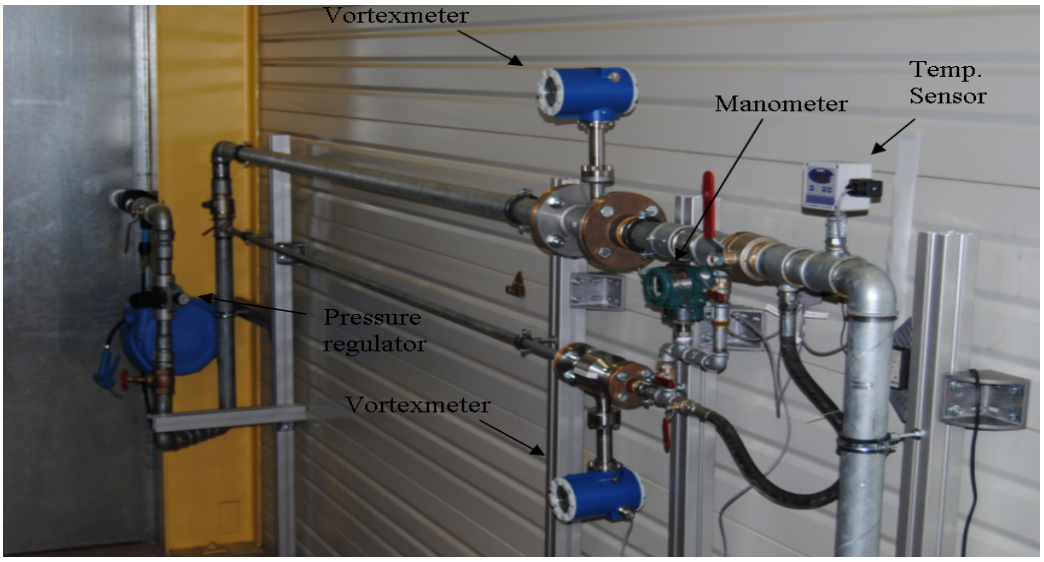

Figure 4.9: Compressed air pipings

After that pressure regulator, the system is equipped with two vortexmeters supplied by Bopp & Reuther to measure the value of the flow rate. They have two complementary ranges $15 - 560\,m^3/h$ and $2 - 25\,m^3/h$ that can be selected using manual valves. Then, the density is evaluated through a manometer which measures the absolute pressure in the range 0 to 10 bars with an uncertainty of $\pm 0.1\%$ of the full scale,and a temperature sensor to

access the air temperature ranging from -50 to $400\,C^o$ with an uncertainty of $\pm 0.2C^o$. Finally, the pipe is connected to a $90\,l$ tank with a $2\,inch$ tube. The final tank has threaded holes to be able to connect the 22 flexible pipes to the small reservoirs of the solenoid valves.

The measurements for the whole experiments carried out will be explained in the following. The pressure at the jets exit is the atmospheric pressure, with the ideal gas assumption $P = \rho r T$. That is, the mean jet velocity is given by, $V_j = \frac{Q_v P}{N_j S_j P_a}$, where Q_v is the volumetric flow rate that measured by the vortex meter, P_a the atmospheric pressure, P the pressure at the vortex meter, N_j the number of jets and S_j the cross section area of one jet. The velocity ratio is then given by $VR = \frac{V_j}{U_e}$, where U_e is the free-stream velocity at the position of the actuators. The mass flow rate is simply given by $Q_m = Q_v \rho$, where ρ in this case is the air density at the vortex meter.

4.4 Sensors

Senflex SF9902 hot film probes were used to asses the wall friction. They are $1.5\,mm$ long and they are deposited on a polyamyde substrate with a thickness less than $0.2\,mm$. They were glued directly on the surface with $60\,\mu m$ double-sided tape. The probes were connected to a four channels constant temperature anemometer AN 1003 manufactured by AAlabSystems. From the previous results (Cuvier et al. [2010]), the hot-film probe located at $x = 10\Phi$, $y = 0$ and $z = 27\Phi$ as shown in figure 4.10, gives the best observation of the state of the flow (separated and attached). This probe is sensitive to the absolute value of the skin friction $|\tau|$. Under control action, the skin friction gain increases i.e. $|\tau| - |\tau_0| > 0$ with $|\tau_0|$ the skin friction in the non-actuated case. In the following, only the voltage E will be used,

since the calibration introduces non-linearities. E_o denotes the voltage in the non actuated case.

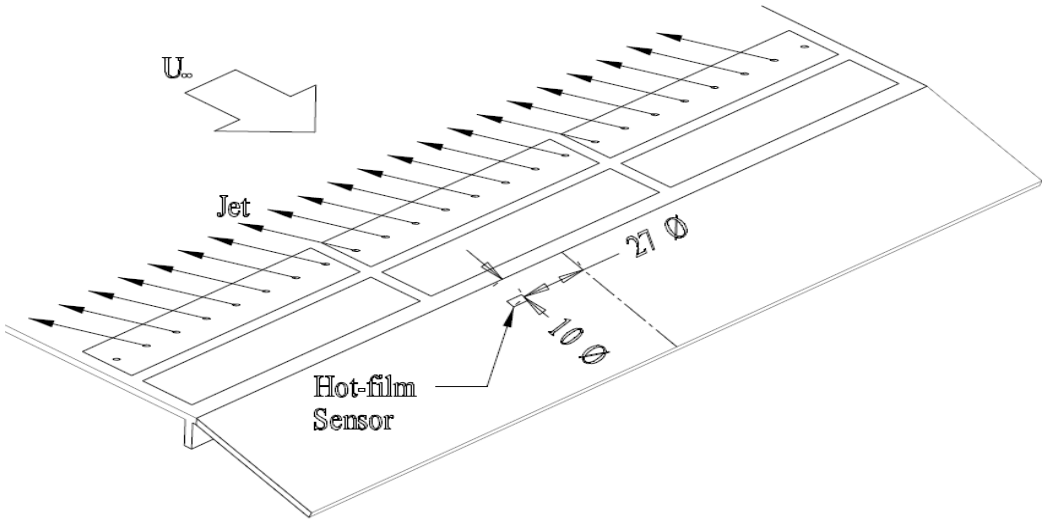

Figure 4.10: Hot-film sensor that have been used in separation control experiments

4.5 Control Set-up

The input signal from the hot film sensor was low-pass filtered by anti-aliasing filter with a cutting frequency f_c (see table 4.4). Then it was digitized with sampling frequency f_{aq} (see table 4.4), using a PCI-DA56036 acquisition board for measurement and computing. This board was mounted on a PC with Linux Ubuntu Studio operating system. Comedi drivers were used together with home made C++ programs to acquire the sensor signal and to send the signal to the valves in the open and closed loop configurations. The

	Open-loop	Closed-loop
f_c	5 KHZ	50 Hz
f_{aq}	20 KHZ	200 Hz

Table 4.4: Acquisition frequency and cut-off frequency for open-loop and closed-loop experiments

open-loop experiments are simply depicted in figure 4.11. For closed-loop control described in figure 4.12, the signal was filtered with a digital low-pass filter to remove oscillations due to the actuation frequency f, f was chosen to be $15\,Hz$ for all closed-loop experiments as will be explained in chapter 5. Therefore, f_c for the digital low-pass was selected to be $2\,Hz$. This induces a strong attenuation of high frequency range and thus removes the possibility to have an indication of the control action.

It was checked that a control order can be send every $10\,ms$ without ant jitters from the management of the operating system. This control speed was found fast enough compared to the time scales separation/reattachment mechanism of the present model as explained in chapter 5. The continuous output signal from the PCI board is then sent to a home made electronic board. Using the ATmega1280 microcontroller of the Arduino mega board, The continuous signal is converted to a square signal. Then, it is distributed towards the 22 solenoid valves using a rapid commutation components. Two power supply ($24V/5A$ and $24V/20A$) were used to provide the necessary start-up current for the opening of the 22 valves ($1A$/valve). In the closed loop configurations the control laws are implemented in the C++ home made program.

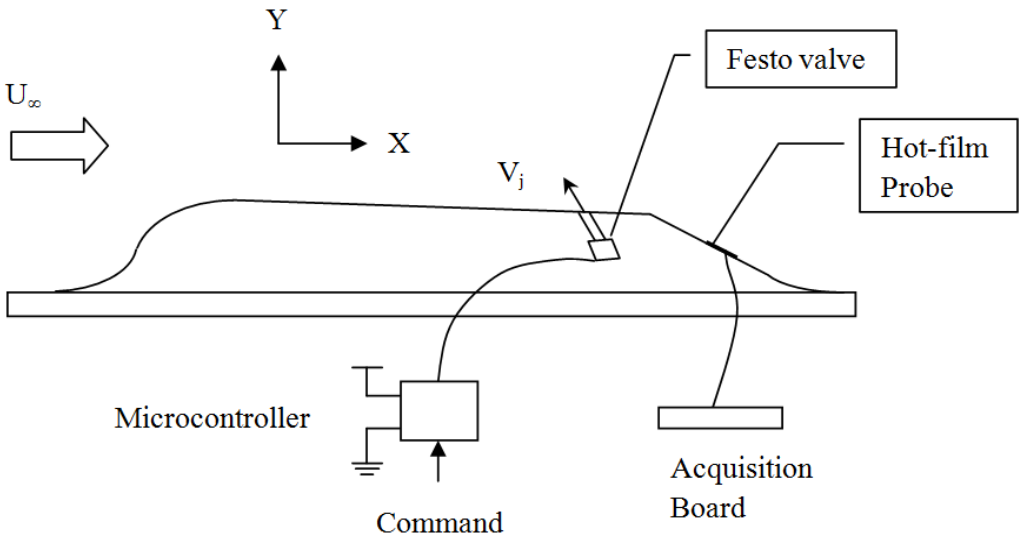

Figure 4.11: Scheme for the open-loop control using pulsed jet actuator over the ramp model

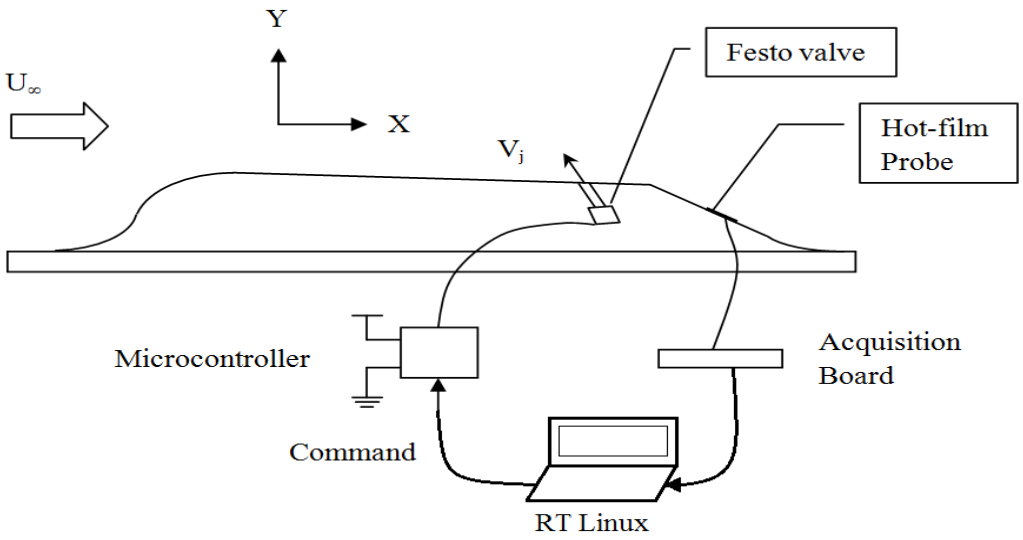

Figure 4.12: Scheme for the closed-loop control using pulsed jet actuator over the ramp model

Chapter 5

Experimental Results

In this chapter open-loop and closed-loop separation control using pulsed jet actuators will be implemented on the ramp model. Open-loop control experiments were performed mainly to assist the design of the linear controllers that will be used in the feed-back control. They were done for Reynolds numbers Re_θ =7500, 10500 and 12600 corresponding to three free stream velocities: 5, 8 and 10 m/s respectively, so as to analyse the effect of the Reynolds number on the separation/reattachment process over this model. Three sets of closed-loop control experiments were performed, i.e. at a constant free stream velocity, at variable free stream velocity with constant reference and at variable free stream velocity with variable reference updated by the free stream velocity.

5.1 Open-loop Results

Open-loop tests were performed using the set-up described in section 4.5. Two objectives were targeted for these experiments. The first one was to help in the design of closed-loop experiments by choosing the adequate in-

put/output variables (figure 5.1) and by extracting the different time scales involved in the system. The second objective was to demonstrate that the

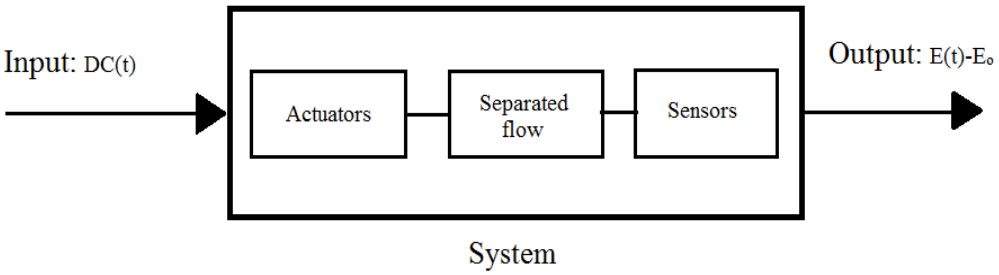

Figure 5.1: Diagram for open-loop control using pulsed jet actuator over the ramp model

efficiency can be improved by enhancement of separated shear layer instabilities using different excitation frequencies (Greenblatt et al. [2000]).

5.1.1 Input/output variables

In this work, the controlled variable for the system is $E - E_o$, where E is the hot-film signal under control actuation and E_o the same signal when the flow is separated, while the manipulated variable is the duty cycle at a specific frequency. This frequency was fixed based on the open-loop results as will be seen later in section 5.1.3. Justifications of the input/output selection for the system in hand are in the next few paragraphs. Three hot-film probes were available on the ramp, and were tested in order to select one for the control experiments. The location of the hot-film sensors is given in table 5.1. Preliminary experiment were performed to test the response of the three probes, one sample result at $U_\infty = 10\,m/s$ is given in figure 5.2. The

Hot-film Sensor	x	z
Number 1	10Φ	27Φ
Number 2	43Φ	0
Number 3	43Φ	-48Φ

Table 5.1: Location of the hot-film sensors on the ramp

difference in response from the probes when the actuator was opened for two seconds is clearly seen. The nonlinear response of probes (2) and (3) can be noticed. On the other hand, the response of probe (1) is linear and it is interesting for the use in closed-loop control. Probe (1) shown in figure 4.10 that is located on the centerline of one produced vortex, was thus chosen to be used in both open-loop and closed-loop experiment. The same probe was selected by Cuvier et al. [2010] to check flow reattachment for different reasons described in section 4.4.

A set of open-loop control experiments with continuous jet actuation at $U_\infty = 5\,m/s$ and different VR is listed in table 5.2. At $U_\infty = 5\,m/s$, the external velocity at the position of the actuator is $U_e = 6.2\,m/s$ (Cuvier et al. [2010]). These experiments were targeted to compare the continuous jet and the pulsed jet actuators and to emphasise the benefit of the pulsed jet actuator compared to the continuous one on the mass flow rate basis. Figure 5.3 shows the phase-averaged controlled variable $E - E_o$ due to continuous jet for the VR values of table 5.2. Figure 5.3(a) shows that the system is a first order one. Figure 5.3(b) shows the linearity of the relation between $E - E_o$ and VR. Despite this linearity, this variable cannot be a favorable input because of the slow response of the jet velocity which is set by a pressure regulator. Also, the linear law given in the figure shows that blowing with

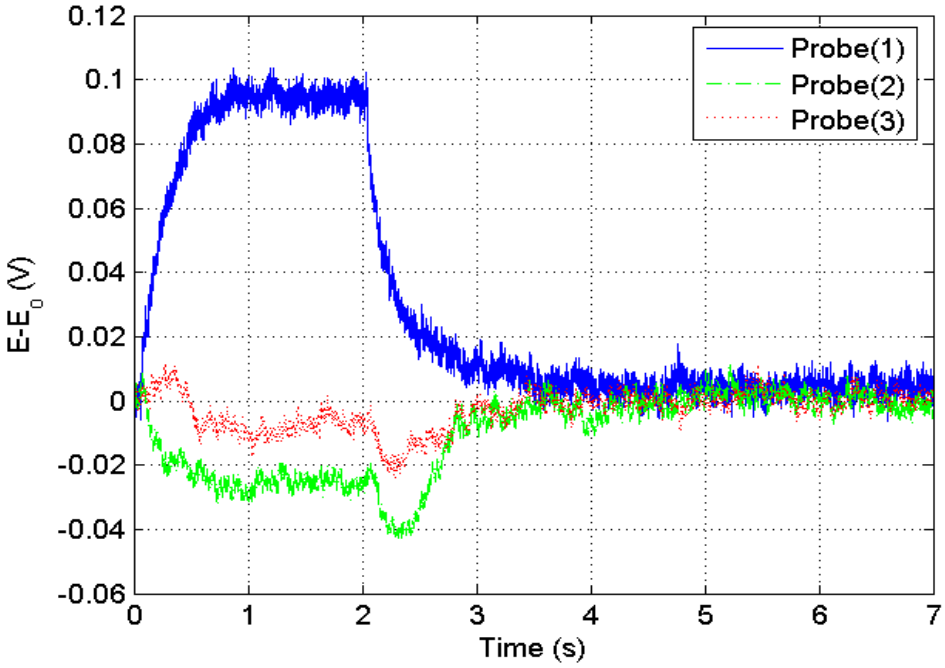

Figure 5.2: Phase averaged response of the hot-film sensors due to continuous blowing at $U_\infty = 10\,m/s$ and $VR = 3.7$

VR less than 2.1 will not affect the flow separation, which almost agrees with result found by Cuvier et al. [2010] that there is no effect for $VR < 1.5$ on the controlled flow as discussed in section 1.1.2. In this set of experiments, the range of VR between 2.78 and 3.58 was chosen because a significant reduction of the separation length was noticed based on the wool tufts visualization at $VR = 2.78$. While blowing with $VR = 3.58$ fully reattaches the flow.

Consequently, it was decided to investigate the effect of the duty cycle. Table 5.3 lists the open-loop control experiments with the pulsed jet actuators at $U_\infty = 5m/s$. The experiments cover the range of actuation frequency f from 6 to 100 Hz. Figure 5.4(a) shows the phase-averaged hot-film signal $E - E_o$ due to pulsed jet with $f = 10\,Hz$ at DC=20, 50, 60, 70 and 80%. It shows that, similarly to VR input variable, this is a first order system.

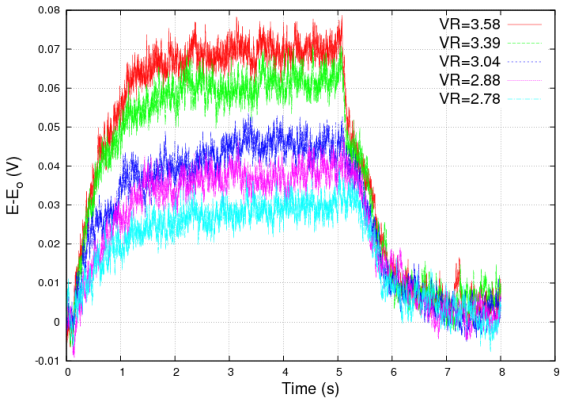

(a) Response of hot-film signal due to continuous jet of $5\,s$ duration

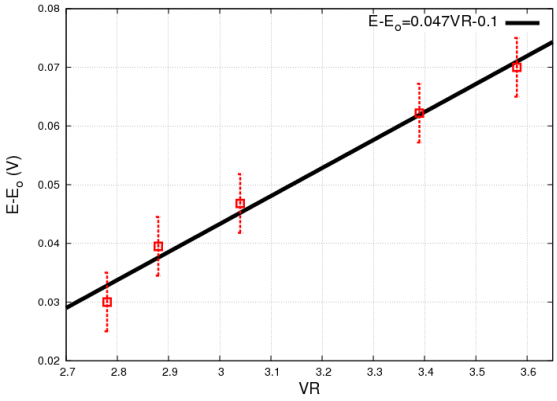

(b) Relation between hot film signal and VR in the steady state

Figure 5.3: Phase averaged open-loop response for continuous jet for different VR at $U_\infty = 5\,m/s$

$Q_m\ (kg/s)$	1.27×10^{-7}	1.32×10^{-7}	1.39×10^{-7}	1.55×10^{-7}	1.64×10^{-7}
VR	2.78	2.88	3.04	3.39	3.58

Table 5.2: Open loop experiments for continuous jet at various VR, for $U_\infty = 5\,m/s$. Each test was 50 packets of 10 s at $f_{acq} = 20KHz$.

Figure 5.4(b) shows the relation between $E - E_o$ and DC at $f = 10\,Hz$. As can be seen, this relation is linear. This is very crucial since DC can be regulated instantaneously, which makes it a favourable input for the closed-loop control. It should be said that this linearity was an unexpected result as the relation between the hot-film signal and the skin friction is nonlinear. Therefore, the signal was not calibrated to get skin friction as it introduces nonlinearities. Consequently, a linear controller can be implemented.

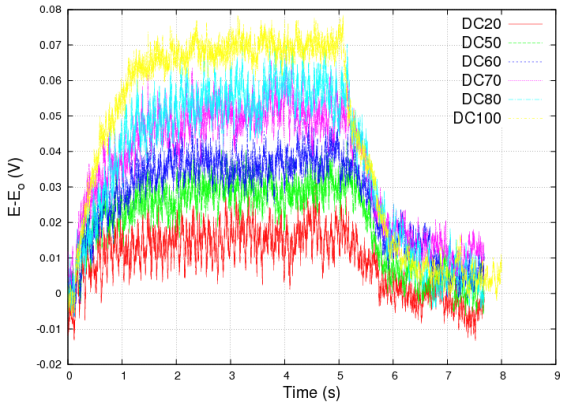

(a) Response of hot-film signal due to pulsed jet at $10\,Hz$ of $5\,s$ duration

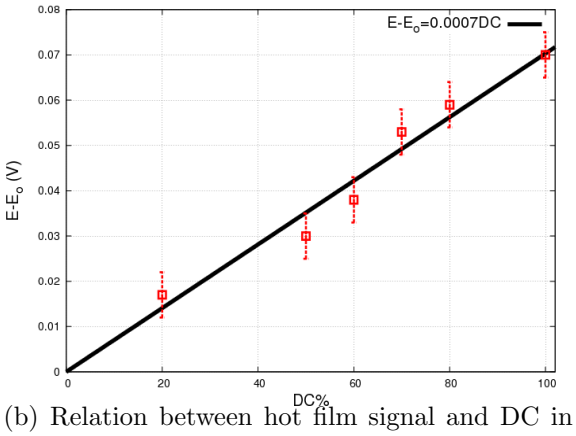

(b) Relation between hot film signal and DC in the steady state

Figure 5.4: Phase averaged open-loop response for pulsed jet with different DC at $f = 10\,Hz$ and $U_\infty = 5\,m/s$

f (Hz)	DC%	Q_m (kg/s)	f (Hz)	DC%	Q_m (kg/s)
10	20	0.33×10^{-7}	15	50	0.82×10^{-7}
10	50	0.82×10^{-7}	15	70	1.15×10^{-7}
10	60	0.98×10^{-7}	50	50	0.82×10^{-7}
10	70	1.15×10^{-7}	50	70	1.15×10^{-7}
10	80	1.31×10^{-7}	80	50	0.82×10^{-7}
6	50	0.82×10^{-7}	80	70	1.15×10^{-7}
6	70	1.15×10^{-7}	100	50	0.82×10^{-7}
13	50	0.82×10^{-7}	100	70	1.15×10^{-7}
13	70	1.15×10^{-7}			

Table 5.3: Open-loop experiments for pulsed jet at at various DC at $U_\infty = 5\,m/s$ and $VR = 3.58$. Each test was 50 packets of 10 s at $f_{acq} = 20KHz$.

5.1.2 Time Scales

The time scales of flow attachment and separation are fundamental in closed-loop control, since the knowledge of these typical time scales and the associated dynamical behavior of the entire process are mandatory to act correctly on the flow. Table 5.4 shows that the typical time scales that can be found in the literature for characterizing the attachment and separation processes are quite different. It appears that no universal value exists for neither the attachment nor the separation time scales. This can be attributed to several factors: the initial state of the flow whether it is attached or separated, the method of actuation and the type of flow configuration (Siauw et al. [2010]).

Two important dimensionless properties were defined in the introduction. The reduced jet actuation frequency:

$$F^+ = \frac{f L_{sep}}{U_\infty}$$

and the time scale

$$t^+ = \frac{t U_\infty}{L_{sep}}$$

.

The separation length $L_{sep} = 0.8\,m$ was measured by wool tufts visualisations at $U_\infty = 10\,m/s$, but at lower free stream velocities this separation length was not that clear. Therefore, $L_{sep} = 0.8\,m$ will be assumed for all free stream velocities.

In this study, two important time scales are defined in figure 5.5: t_{set} and t_{Delay}. They where characterized in detail by open-loop tests at $U_\infty =$ 5, 8 and 10 m/s. t_{set} is found the same for the separation and attachment process for all free stream velocities. This is a significant difference from the previous studies given in table 5.4, where the attachment time scales are much shorter than separation ones (except Darabi and Wygnanski [2004]).

Authors	Amitay and Glezer [2002b]	Darabi and Wygnanski [2004]	Mathis et al. [2009]	Siauw et al. [2010]	present study
Test Configuration	Modified wing profile	Generic flap	Beveled splitter plate	Naca airfoil 0015	Ramp
Reynolds number	3.1×10^5 (scaled by wing chord and U_∞)	1.24×10^5 (scaled by flap length and U_∞)	1.44×10^5 (scaled by bevel length and U_∞)	10^6 (scaled by wing chord and U_∞)	2.6×10^5 to 5.1×10^5 (scaled by L_{sep} and U_∞)
Actuator type	Synthetic jet	Synthetic jet	Steady jet	Fluidic vortex generator	Fluidic vortex generator
$C_\mu = \frac{\rho_j U_j^2 S_j}{\frac{1}{2}\rho_\infty U_\infty^2 S_{ref}}$	3.5×10^{-3}	5×10^{-4} to 8×10^{-4}	9×10^{-2} to 2.2×10^{-2}	0.67×10^{-2}	9.2×10^{-4}
t^+ (attachment)	∼9.5	16-70 (16 is the optimal value)	5	10	13.8 to 20
t^+ (separation)	∼14	20	25	20	13.8 to 20

Table 5.4: Typical separation/attachment time scales. In the definition of the momentum coefficient C_μ; ρ_j is the actuator flow density, U_j denotes peak jet velocity, S_j is the total area of the actuators, ρ_∞ and U_∞ are the free stream density and velocity respectively and, S_{ref} is usually taken as the length of the body under consideration (e.g. chord, or flap length$\times 1\,m$) for two-dimensional configuration or total wing area for three-dimensional configurations. (Siauw et al. [2010])

This result was carefully verified for all tested free stream velocity. Therefore, t_{set} refers here to both separation and attachment process. The calculation for t_{set} was carried out using the following formula

$$t_{set} = -\tau \ln(0.01) + t_{Delay} \tag{5.1}$$

where t_{Delay} is the time delay of the response. Equation 5.1 was derived by assuming that the response resembles the solution of linear first order system having the form given in equation 3.4, as was discussed in section 3.2. Calculation of the time constant (τ) was done by least square fitting of the signal at $U_\infty = 5$, 8 and 10 m/s. The results are given in table 5.6. The uncertainty on the settling time ($u(t_{set})$) is calculated by:

$$u(t_{set}) = \sqrt{(-\ln(0.01)u(\tau))^2 + u(t_{Delay})^2} \tag{5.2}$$

The delay t_{Delay} in the response of the hot-film signal observed in figure 5.5 has three main sources. The convective time from the actuator to the hot-film probe (t_{conv}), which will be defined below. The delay due to the valve (dt_a) discussed in section 2.4.2. Finally, the delay due to the treatment of the signal in the closed-loop case. This response delay will be discussed later in this section. The convective time is defined as

$$t_{conv} = t_{Delay} - dt_a = \frac{L_{conv}}{U_{conv}} \tag{5.3}$$

where $L_{conv} = 0.44\,m$ is the distance between the actuator and the hot-film probe and U_{conv} is the convective velocity.

Table 5.5 lists two pulsed jet experiments with $f = 10\,Hz$ and a variable DC at $U_\infty = 5\,m/s$. The results are shown in figures 5.6(a) and 5.6(b) for increasing DC and decreasing DC respectively. It can be seen that the time scales for separation and attachment are equal, which agrees with the results

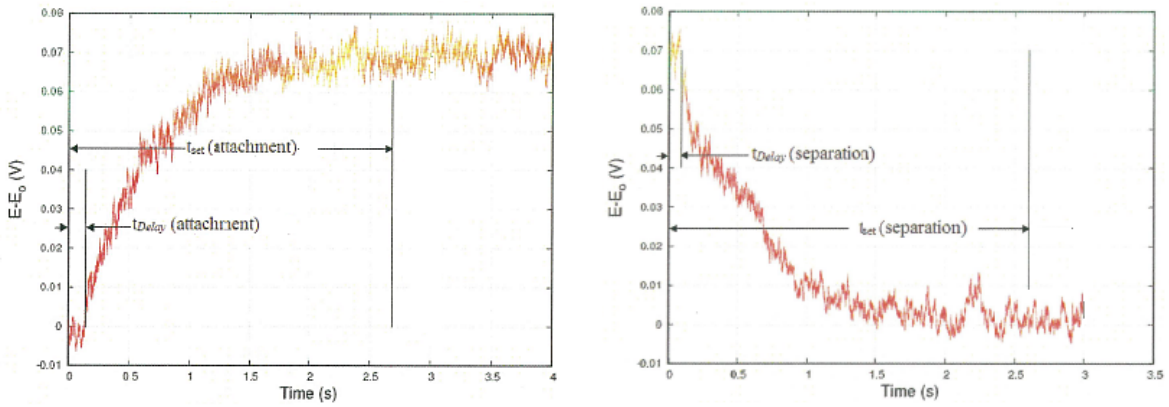

(a) Attachment time scales (b) Separation time scales

Figure 5.5: Definitions of the separation and attachment time scales at $U_\infty = 5\,m/s$ and $VR = 3.58$.

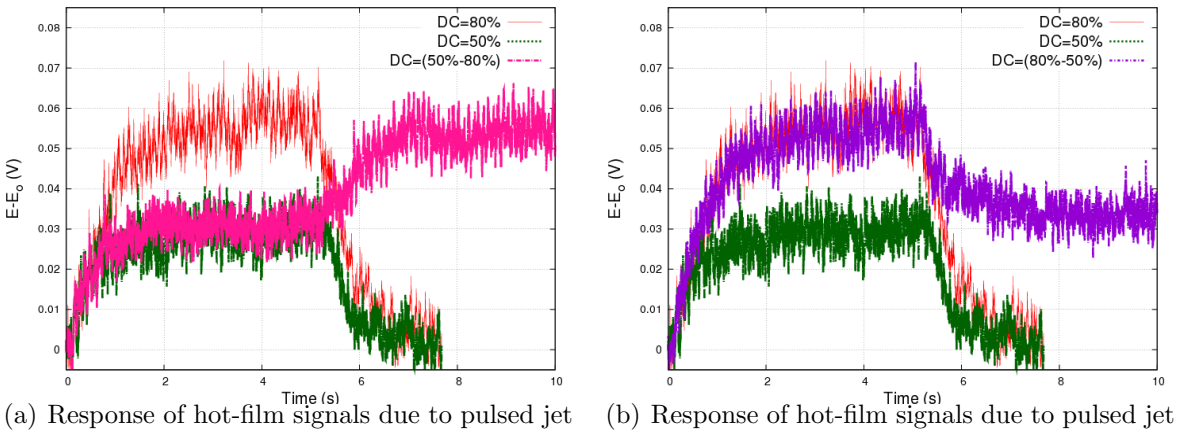

(a) Response of hot-film signals due to pulsed jet with increasing DC (b) Response of hot-film signals due to pulsed jet with decreasing DC

Figure 5.6: Phase averaged open-loop response for pulsed jet with variable DC at $U_\infty = 5\,m/s$ and $VR = 3.58$

shown in figures 5.4(a) and 5.5. Also, the time scales towards separation and attachment are equal.

The effect of VR on the time scales at $U_\infty = 5\,m/s$ can be seen in figure

$f\ (Hz)$	DC%	$Q_m\ (kg/s)$
10	(50-80)	$(0.82 - 1.31) \times 10^{-7}$
10	(80-50)	$(1.31 - 0.82) \times 10^{-7}$

Table 5.5: Open loop experiments for pulsed jet at 5 m/s with variable DC, $U_\infty = 5\,m/s$ and $VR = 3.58$, each test was 50 packets of $10\,s$ at $f_{acq} = 20KHz$.

5.3(a). It is found that blowing with VR=2.78 the time scale $t_{set} = 3.4\,s$ and with VR=3.58 $t_{set} = 2.8\,s$. The higher VR the shorter the time scales, since blowing with higher velocity ratios gives more control authority to the actuator.

In order to judge whether the flow is attached or not, the hot-film signal from probe (1) gives a good criteria for the separation/reattachment process. Above a certain level of $E - E_0$ the flow is attached, estimated from the wool tufts visualizations. This value varies with free stream velocity as can be seen in figure 5.7. This is obtained with DC$\simeq$ 50% and VR$\simeq$ 3.6

Table 5.7 and 5.8 list the open-loop control experiments with the pulsed jet actuators at $U_\infty = 8\,m/s$ and $10\,m/s$ respectively. At $U_\infty = 10\,m/s$, the external velocity at the position of the actuator is $U_e = 12.4\,m/s$ (Cuvier et al. [2010]), but at $U_\infty = 8\,m/s$, U_e was estimated to be $9.92\,m/s$. The experiments cover the range of actuation frequencies between 10 and 100 Hz. Figure 5.8 and 5.9 show the hot-film signal $E - E_o$ as a function of time at $U_\infty = 8\,m/s$ and $10\,m/s$ respectively, for pulsed jet with f = 10, 30, 50 ,70 and 100 Hz and DC= 10, 50 and 80. It can be seen that the t_{set} at specific free stream velocity do not depend on the actuation frequency. While the steady state value of the hot film-signal vary with the actuation frequency.

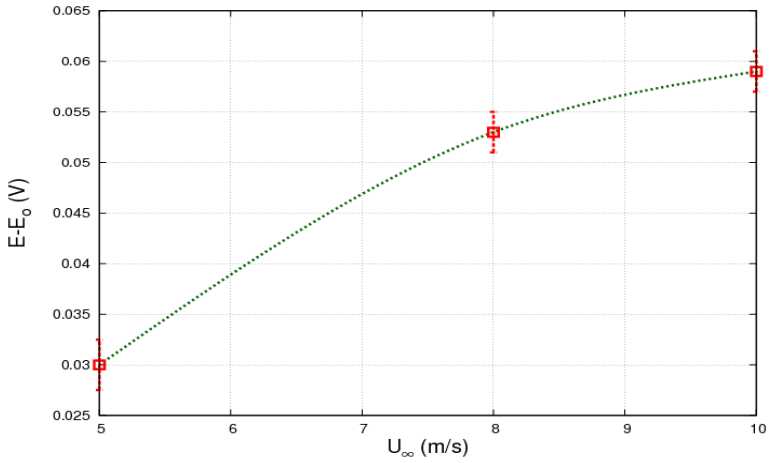

Figure 5.7: Threshold of the relative value of $E - E_0$, observed from one hot-film signal, over which the flow is attached on the flap (with DC$\simeq$ 50%, VR$\simeq$ 3.6 and $f = 15\,Hz$).

The linear fit is given in figures 5.4(b), 5.8(f) and 5.9(f) at $U_\infty = 5$, 8 and $10\,m/s$ respectively, it is clear that the static gain is increasing with the free stream velocity.

Table 5.6 summarizes the major time scales of the open-loop control experiments. The delay of response of the hot-film signal t_{Delay} was investigated and averaged for all the tests at each free stream velocity (U_∞= 5, 8 and 10 m/s). The valve delay of $0.0015\,s$ is calculated using equation 2.7 for a tube length of $20\,cm$.It is much less than the convective time. The measured delay t_{Delay} is thus mainly due to the convective time. Further investigations should be done in the future work, to check why the convective velocity does not depend linearly on the free stream velocity. The time scale for the separation/reattachment process (t_{set}) is varying with the free stream velocity in a logical way (table 5.6). The higher the free stream velocity the shorter t_{set}.

$U_\infty\,(m/s)$	$t_{Delay}\,(s)$	$t_{conv}\,(s)$	$U_{conv}\,(m/s)$	$\tau\,(s)$	$t_{set}\,(s)$	t_{set}^{+}
5	0.149 ± 0.008	0.147	3	0.575 ± 0.001	2.8 ± 0.01	17.5
8	0.132 ± 0.008	0.13	3.4	0.407 ± 0.008	2 ± 0.04	20
10	0.107 ± 0.008	0.106	4.2	0.206 ± 0.008	1.06 ± 0.04	13.8

Table 5.6: Summary of the time scales of the open-loop experiments

$f\ (Hz)$	DC%	$Q_m\ (kg/s)$
Cont.	100	2.64×10^{-7}
10	10	0.26×10^{-7}
10	50	1.32×10^{-7}
10	80	2.11×10^{-7}
30	10	0.26×10^{-7}
30	50	1.33×10^{-7}
30	80	2.12×10^{-7}
50	10	0.26×10^{-7}
50	50	1.33×10^{-7}
50	80	2.12×10^{-7}
70	10	0.26×10^{-7}
70	50	1.33×10^{-7}
70	80	2.12×10^{-7}
100	10	0.26×10^{-7}
100	50	1.33×10^{-7}
100	80	2.12×10^{-7}

Table 5.7: open loop experiments for pulsed jet at $U_\infty = 8\,m/s$ and $VR = 3.65$. Each test was 100 packets of 5 s at $f_{acq} = 20KHz$.

$f\ (Hz)$	DC%	$Q_m\ (kg/s)$
Cont.	100	3.2×10^{-7}
10	10	0.32×10^{-7}
10	50	1.6×10^{-7}
10	80	2.65×10^{-7}
30	10	0.32×10^{-7}
30	50	1.6×10^{-7}
30	80	2.65×10^{-7}
50	10	0.32×10^{-7}
50	50	1.6×10^{-7}
50	80	2.65×10^{-7}
70	10	0.32×10^{-7}
70	50	1.6×10^{-7}
70	80	2.65×10^{-7}
100	10	0.32×10^{-7}
100	50	1.6×10^{-7}
100	80	2.65×10^{-7}

Table 5.8: open loop experiments for pulsed jet at $U_\infty = 10\,m/s$ and $VR = 3.5$.Each test was 100 packets of 5 s at $f_{acq} = 20KHz$.

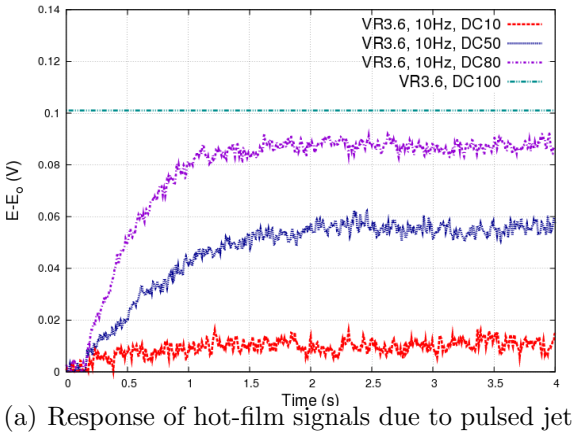

(a) Response of hot-film signals due to pulsed jet at $10Hz$

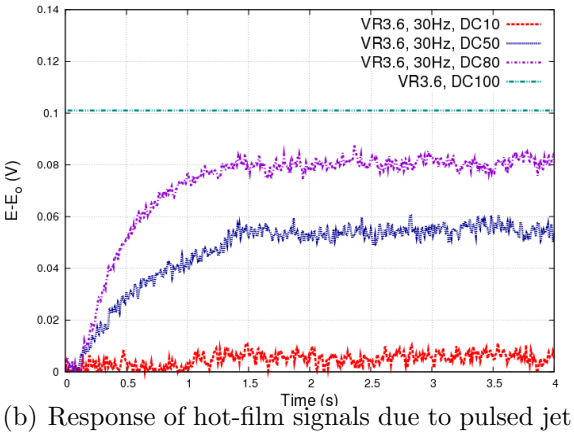

(b) Response of hot-film signals due to pulsed jet at $30Hz$

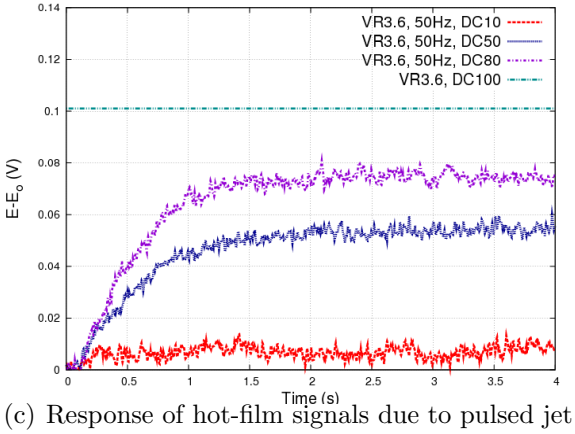

(c) Response of hot-film signals due to pulsed jet at $50Hz$

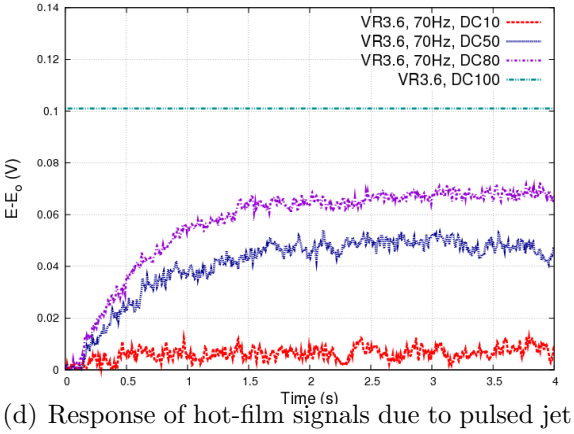

(d) Response of hot-film signals due to pulsed jet at $70Hz$

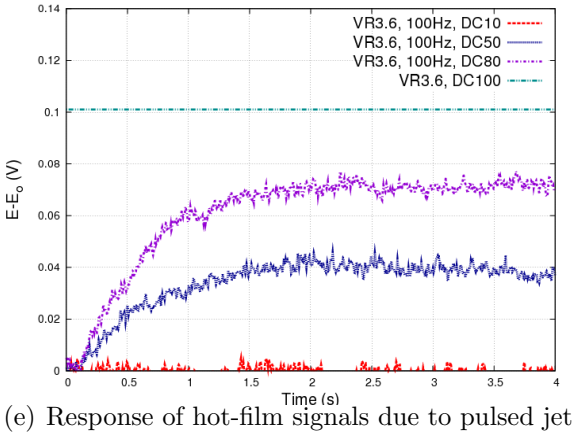

(e) Response of hot-film signals due to pulsed jet at $100Hz$

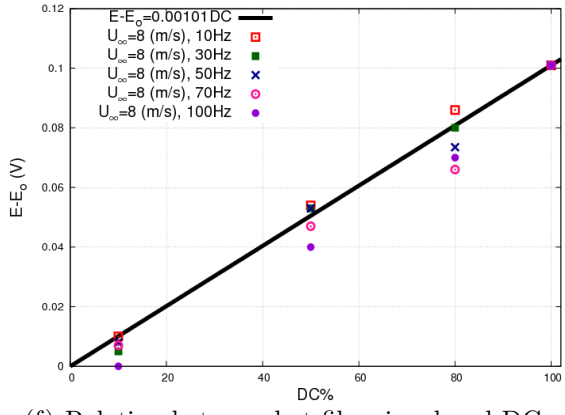

(f) Relation between hot film signal and DC

Figure 5.8: Phase averaged Open-loop response for pulsed jet with different actuation frequency and DC at $U_\infty = 8m/s$

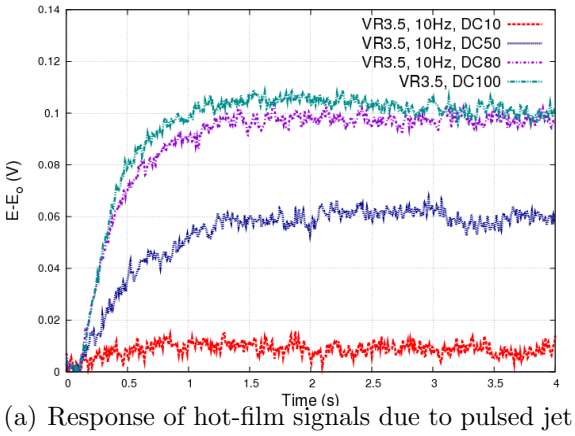

(a) Response of hot-film signals due to pulsed jet at $10Hz$

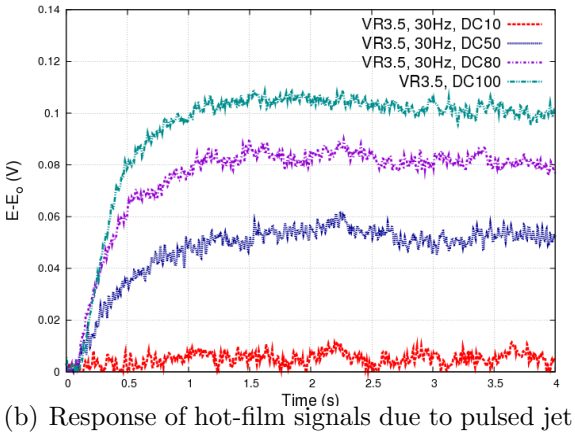

(b) Response of hot-film signals due to pulsed jet at $30Hz$

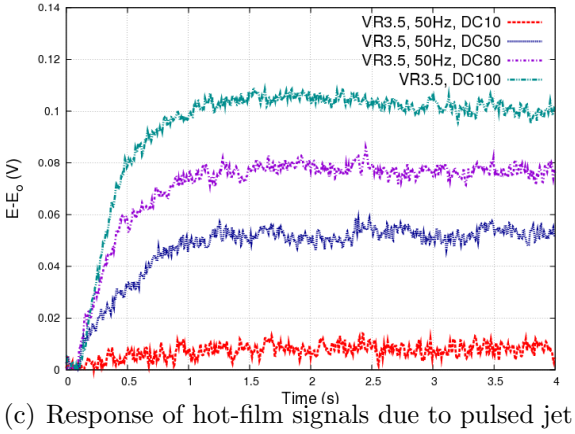

(c) Response of hot-film signals due to pulsed jet at $50Hz$

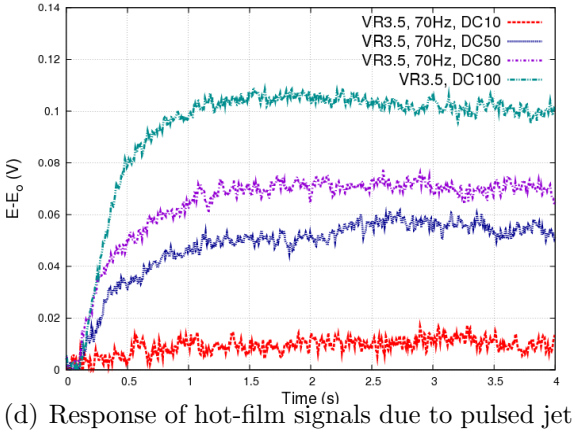

(d) Response of hot-film signals due to pulsed jet at $70Hz$

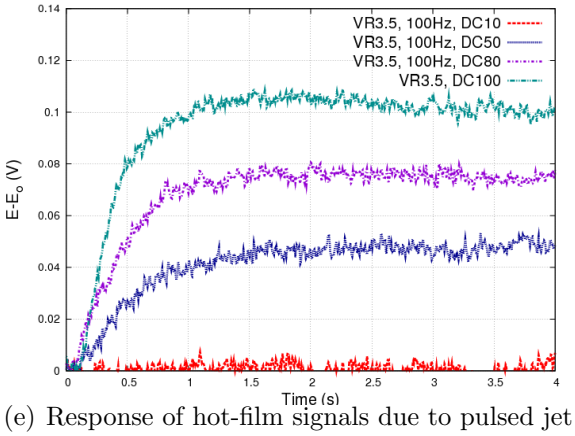

(e) Response of hot-film signals due to pulsed jet at $100Hz$

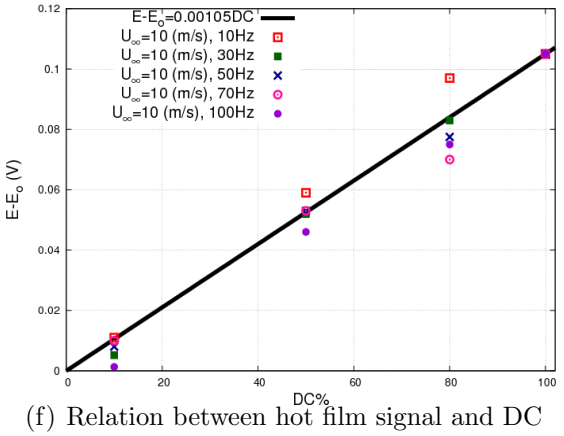

(f) Relation between hot film signal and DC

Figure 5.9: Open-loop response for pulsed jet with different actuation frequency and DC at $U_\infty = 10m/s$

5.1.3 Influence of the actuation frequency

The open-loop experiments were targeted to check the influence of the actuation frequency on the gain of the hot-film signal, and to compare the continuous jet and pulsed jet actuators. When comparing the hot-film signal at $DC = 50\%$, $f = 10\,Hz$ and $VR = 3.58$ with hot-film signal with $VR = 2.78$ from the continuous jet experiments in figure 5.10, it can be seen easily that both signals correspond to almost the same voltage. But with a mass flow rate equal to $0.82 \times 10^{-7}\,kg/s$ in the pulsed jet case and $1.27 \times 10^{-7}\,kg/s$ in the continuous jet case. Which means more than 35% reduction on the mass flow rate when using the pulsed jet actuator in this case. Furthermore, the settling time is shorter in the pulsed jet case, where $t_{set} = 2.8\,s$. But in the continuous jet case $t_{set} = 3.4\,s$, due to blowing with lower VR than the pulsed jet case.

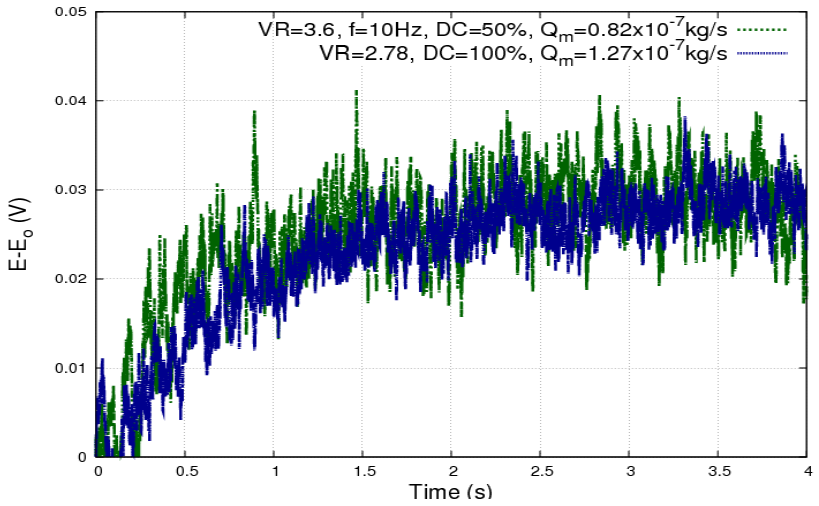

Figure 5.10: Pulsed jet vs. continuous jet at $U_\infty = 5\,m/s$

Figure 5.11 depicts the effect of the actuation frequency on the gain on wall friction at $U_\infty = 5\,m/s$. This figure shows that for two different DC, two

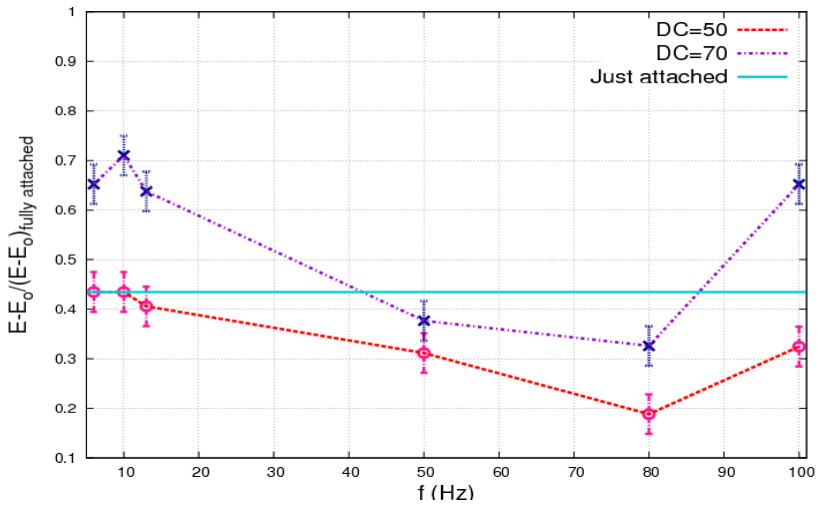

Figure 5.11: Influence of actuation frequency at $U_\infty = 5\,m/s$

ranges of frequencies around $10\,Hz$ and $100\,Hz$ can be optimal (in the range of the present investigation), based on the maximum gain of the hot film signal (skin friction) with the same mass flow rate of the jet. It was verified from the wool tufts visualisations that at $E - E_o/(E - E_o)_{fully\,attached} = 0.44$ the flow at $U_\infty = 5\,m/s$ is just attached, while below this value the flow is separated.

It is visible from figures 5.8(f) and 5.9(f) at $U_\infty = 8$ and $10\,m/s$ respectively, that some frequencies give more gain in skin friction such as 10 and 30 Hz, and also at 30 Hz the response is linear for both cases.

Figure 5.12 shows the effect of the actuation frequency on the reattachment mechanism at $U_\infty = 8m/s$. The figure shows that the range of frequencies from $10Hz$ to $30Hz$ can be optimal, based on the maximum gain of the hot film signal (skin friction) with the same mass flow rate of the jet. It was verified from the wool tufts visualisations that at $E - E_o/(E - E_o)_{fully\,attached} = 0.52$ the flow at $U_\infty = 8\,m/s$ is just attached.

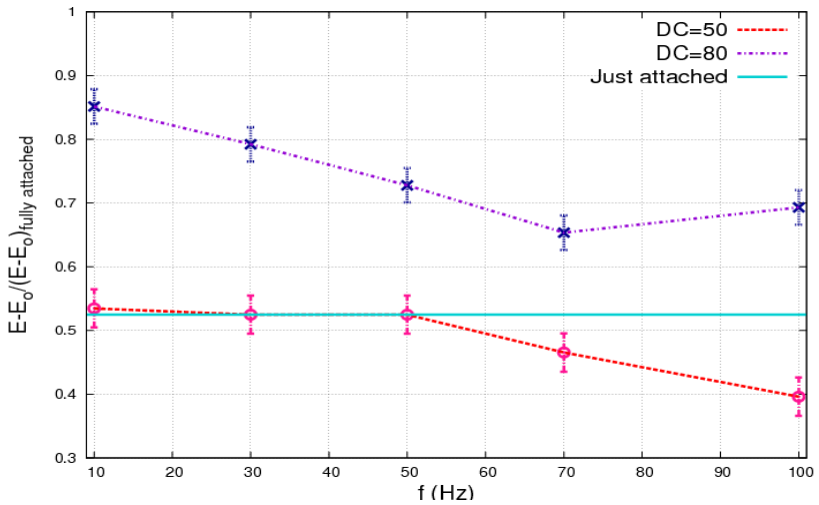

Figure 5.12: Influence of actuation frequency at $U_\infty = 8\,m/s$

The effect of the actuation frequency on the gain of the hot film signal at $U_\infty = 10m/s$ is shown in figure 5.13. The figure shows that the range of frequencies around $10Hz$ can be optimal, based on the maximum gain of the hot film signal (skin friction) with the same mass flow rate of the jet. It was verified from the wool tufts visualisations that at $E - E_o/(E - E_o)_{fully\,attached} = 0.56$ the flow at $U_\infty = 10\,m/s$ is just attached.

One generalization that can be made based on table 5.9, is that the actuation frequency within the range $0.8 \leq F^+ \leq 1.6$ can be optimal regardless of the free stream velocity. For the closed-loop experiments in the next section, f was chosen to be $15\,Hz$ which is in the optimal range of the actuation frequency for all tested free stream velocities.

From figures 5.11 to 5.13, it is clear that the influence of the frequency as a function of free stream velocity (and thus Reynolds number) is complex. It is not possible, based on the present results to go into an interpretation. What is clear is that when the frequency goes to infinity, the results should

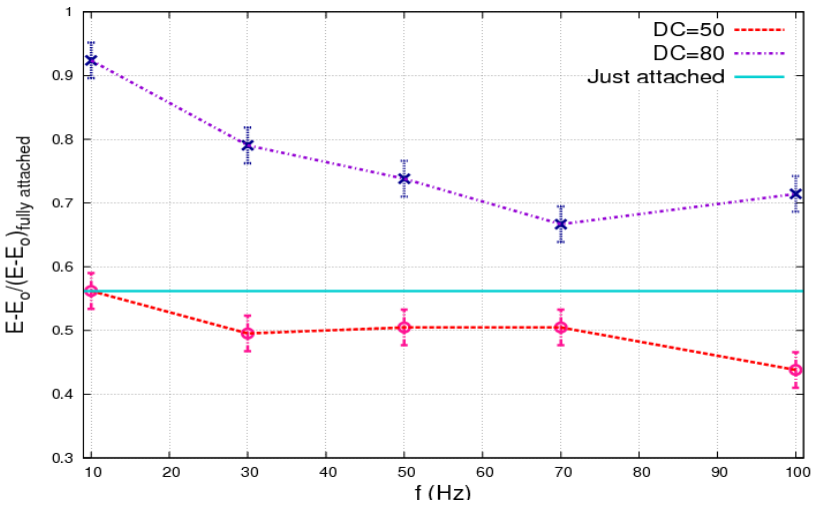

Figure 5.13: Influence of actuation frequency at $U_\infty = 10\,m/s$

$U_\infty(m/s)$	optimal $f\,(Hz)$	optimal F^+
5	10 , 100	1.6 , 16
8	10 , 30	1 , 3
10	10	0.8

Table 5.9: Optimal actuation frequency at $U_\infty = 5$, 8 and 10 (m/s)

approach the continuous blowing. The effect of low frequencies is much less clear and would need a more detailed investigation with a wider range and finer sampling and characterization of the interaction by PIV. This is out of the scope of the present work.

5.1.4 Conclusion on open-loop experiments

Open-loop control experiments have been conducted for the separated flow by means of pulsed jet actuator. As a first step, adequate input/output for

the control problem was selected, in order to get linear response $(E - E_o)$ for experimentally feasible control input (DC). The time scales of the separation/attachment process have been identified and compared to the literature. These time scales were found varying with VR and the free stream velocity (Reynolds number), but independent of the duty cycle. The influence of the actuation frequency have been studied, and optimal frequencies were identified for each free stream velocity, that will be used in closed-loop control.

5.2 Closed-loop Results

From open-loop results in section 5.1, it was clear that the actuation frequency can improve the control efficiency when it is adapted to the baseline flow. However, the closed-loop adaptation in the time domain is not straight forward and more knowledge of the control mechanisms is needed. Therefore, in the present closed-loop experiments, two objectives were targeted. The first one was to improve the control reactivity using different types of controllers (PI, LQR) for a given free stream velocity. The second one was to adapt the control under variations of the free stream velocity. The fact that the system for the separated flow under actuation can be represented by a linear first order model (discussed in the next chapter) facilitates closed-loop control design using linear theory.

The control problem is to tune the controllers in order to minimize the settling time that was found by open-loop tests, with 10% as the maximum percentage overshoot. Accurate evaluation of the settling time was carried out using sliding averaging of the response.

A detailed description of the closed-loop experiments can be found in section 4.5 with the closed-loop experimental set-up depicted in figure 4.12. The theory of the PI and LQR controllers was explained in sections 3.2 and 3.3 respectively. The structure of the closed-loop system with PI controller and LQR controller are depicted in figures 3.2 and 3.4 respectively.

5.2.1 Improvement of the control reactivity

Table 5.10 lists the closed-loop control experiments with the pulsed jet actuators at $U_\infty = 5\,m/s$. As for the open loop tests, the results are averaged on 100 realizations of 15 s in order to minimize the fluctuations induced by

Controller	Gain	Reference (V)	U_∞ (m/s)	VR
I	$K_i = 1$	0.0335	5	3.58
I	$K_i = 2$	0.0335	5	3.58
I	$K_i = 5$	0.0335	5	3.58
P	$K_p = 0.5$	0.0335	5	3.58
P	$K_p = 1$	0.0335	5	3.58
P	$K_p = 2$	0.0335	5	3.58
PI	$K_p = 1,\ K_i = 1$	0.037	5	3.58
PI	$K_p = 0.9,\ K_i = 1.5$	0.037	5	3.58
LQR	$K = 2.3$	0.0356	5	3.58
LQR	$K = 8$	0.0356	5	3.58
P	$K_p = 1$	0.064	10	3.5
LQR	$K = 8$	0.05	10	3.5

Table 5.10: Closed-loop experiments at constant U_∞ for pulsed jet with $f = 15\,Hz$, each test was 100 packets of 15 s at $f_{acq} = 200Hz$

the turbulent flow. Several types of controllers were used, such as integral controller with $k_i = 1$, 2 and 5, proportional controller with $k_p = 0.5$, 1 and 2, proportional and integral controller with (k_p, k_i) = (1, 1) and (0.9, 1.5) and finally, LQR controller with $K = 2.3$ and 8. LQR gains were calculated based on the system 6.5 that will be discussed in the next chapter, using equations 3.14 and 3.15, with $R = 1$ and $Q = 6700$ and 23500 respectively. Table 5.10 also lists the closed-loop control experiments with the pulsed jet actuators at $U_\infty = 10m/s$. Two types of controller were used, the P controller with $k_p = 1$, and LQR controller with $K = 8$.

Figure 5.14 depicts the closed-loop experiments with the P controller at $U_\infty = 5m/s$. It shows how the settling time decreased by increasing k_p, for example, at $k_p = 2$, $t_{set} \simeq 1.1\,s$ with a slight overshoot. While at $k_p = 1$, $t_{set} \simeq 1.2\,s$ and at $k_p = 0.5$, $t_{set} \simeq 1.6\,s$. For all results with the proportional controller, the settling time is improved compared to the open-loop control case, where $t_{set} = 2.65\,s$. Due to the steady state error from the P controller (as was discussed in subsection 3.2.1), the reference shown in figure 5.14(a) is not the actual reference that was compared with feedback signal. This steady state error was taken into account using equation 3.9, to have almost the same output for each case. Figure 5.14(b) shows the proportional controller output. It demonstrates the penalty of faster response, for example at $k_p = 2$, it has the highest control effort. Also it can be noticed from that figure that the steady state values for the controllers have a slight difference, due to some experimental calibration problems.

Figure 5.15 shows the closed-loop response with the I controller with different k_i gains at $U_\infty = 5m/s$. The figure clearly shows that the controller is not able to improve the reactivity of the system in terms of settling time. The settling time is not affected by changing k_i, that is; $t_{set} \simeq 7\,s$ for all

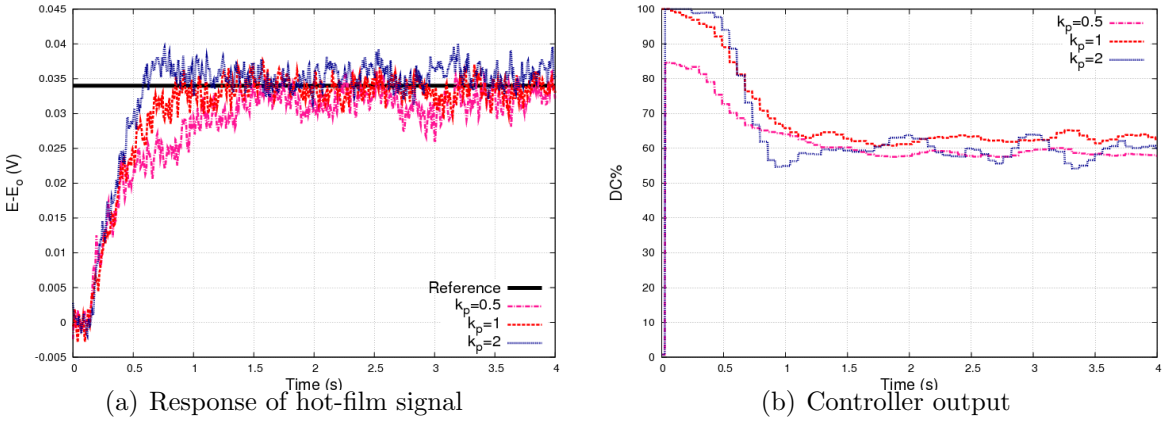

(a) Response of hot-film signal (b) Controller output

Figure 5.14: Closed-loop system response using P controller with $k_p = 0.5$, 1 and 2 at $U_\infty = 5m/s$

tested values of k_i, which is higher than the time scales found in the open-loop case. But on the other hand, the overshoot is increased by increasing the k_i gain. Figure 5.15(b) shows more oscillations associated with increasing the gain in the controller output. Again, it can be noticed that the steady state values for the output have a slight difference.

Figure 5.16 shows the closed-loop response with the PI controller at $U_\infty = 5m/s$. As illustrated by figure 5.16, for ($K_p = 1$, $K_i = 1$), the settling time is $t_{set} \simeq 5.4\,s$. While for the other case ($K_p = 0.9$, $K_i = 1.5$), $t_{set} \simeq 2.8\,s$. For both cases the settling time is longer than in the open-loop case. Figure 5.16(b) shows the PI controller output, it is clear that the PI controller with $K_p = 0.9$, $K_i = 1.5$ consumes more in the transient state. But in the steady state specially after $t = 4\,s$, the controller outputs for both controllers do not converge to the same steady state value. Even though, the responses converge to the same one. Which maybe explained by their reaction to the flow perturbations.

Figure 5.17 shows the closed-loop response with the LQR controller at

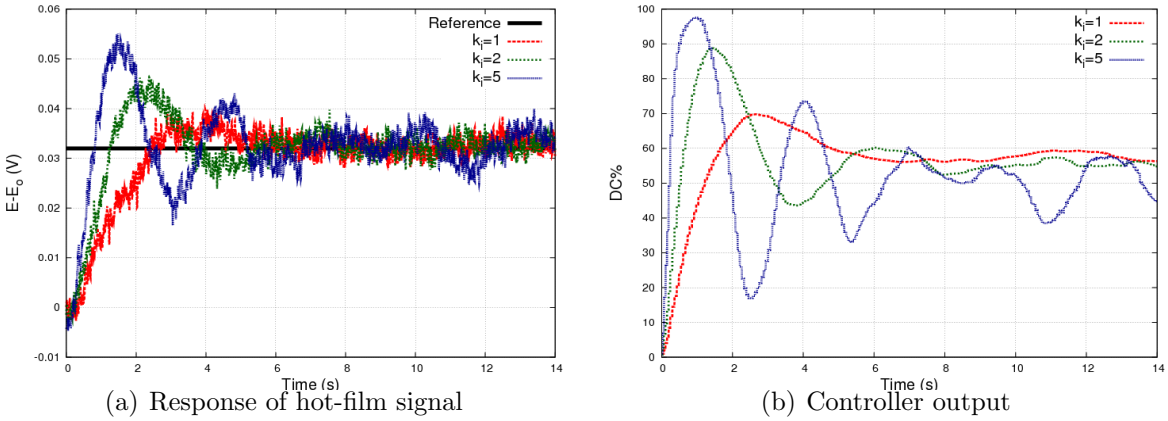

(a) Response of hot-film signal (b) Controller output

Figure 5.15: Closed-loop system response using I controller with $k_i = 1$, 2 and 5 at $U_\infty = 5m/s$

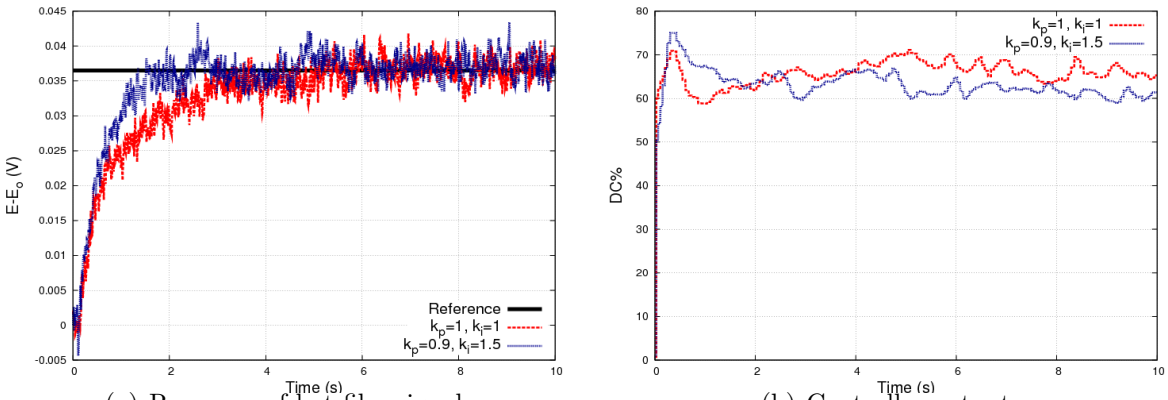

(a) Response of hot-film signal (b) Controller output

Figure 5.16: Closed-loop system response using PI controller with $K_p = 1$, $K_i = 1$ and $K_p = 0.9$, $K_i = 1.5$ at $U_\infty = 5m/s$

$U_\infty = 5\,m/s$. As can be seen from the figure, for the state-feed back gain $K = 2.3$, $t_{set} \simeq 1.5\,s$ and at $K = 8$, $t_{set} \simeq 0.8\,s$. Furthermore, there is no overshoot for both cases. In the case of LQR controller with $K = 8$, we have the best performance in terms of settling time and percentage over-shoot.

Figure 5.17(b) shows the LQR controller output, it shows the penalty of faster response, which is higher control effort.

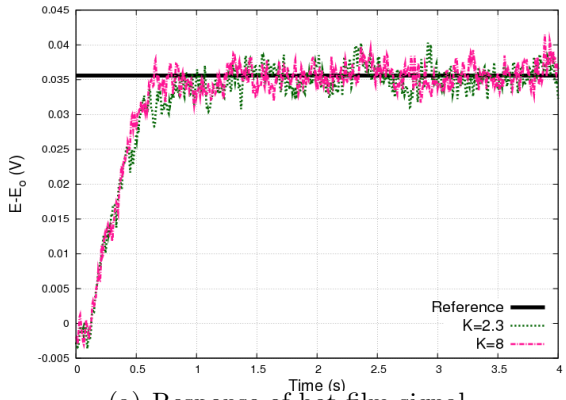

(a) Response of hot-film signal

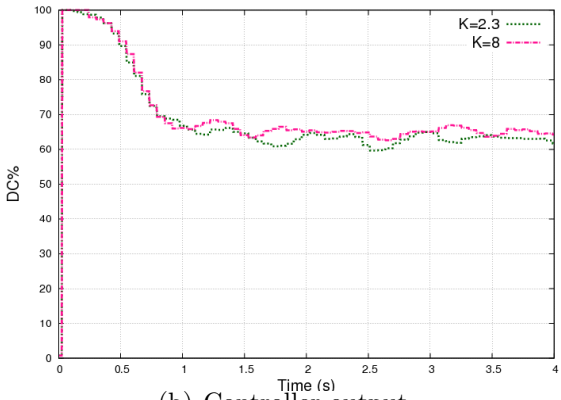

(b) Controller output

Figure 5.17: Closed-loop system response using LQR controller with $K = 2.3$ and 8 at $U_\infty = 5\,m/s$

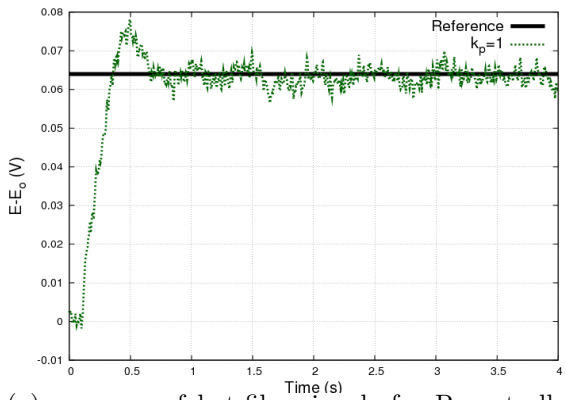

(a) response of hot-film signals for P controller with $k_p = 1$

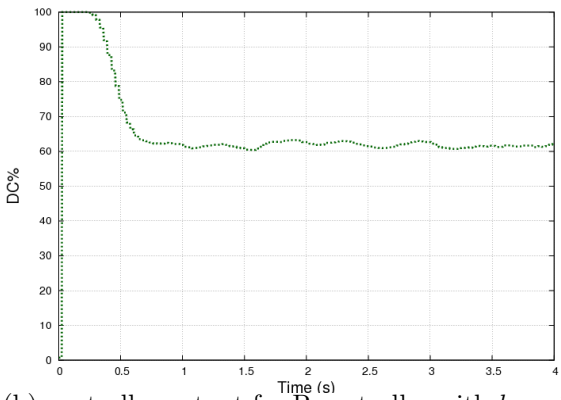

(b) controller output for P controller with $k_p = 1$

Figure 5.18: Closed-loop system response for P controller with $k_p = 1$ at $U_\infty = 10m/s$

In order to test the reactivity to the free stream velocity, a few tests were

performed at $U_\infty = 10\,m/s$. Figure 5.18 shows the closed-loop response for P controller at $U_\infty = 10\,m/s$ with $k_p = 1$. It can be seen that $t_{set} \simeq 0.7\,s$ with a 17% overshoot. Figure 5.19 shows the closed-loop response for LQR controller at $U_\infty = 10\,m/s$ with $K = 8$. The figure shows that $t_{set} \simeq 0.75\,s$ with a 18% overshoot. The settling time is again improved compared to the open-loop control at $U_\infty = 10m/s$, for which $t_{set} \simeq 0.95\,s$. It is clear that the gains k_p and K should be reduced in both P and LQR cases in order to have better performance in terms of reducing the overshoot. The gains were selected based on the previous results at $U_\infty = 5\,m/s$.

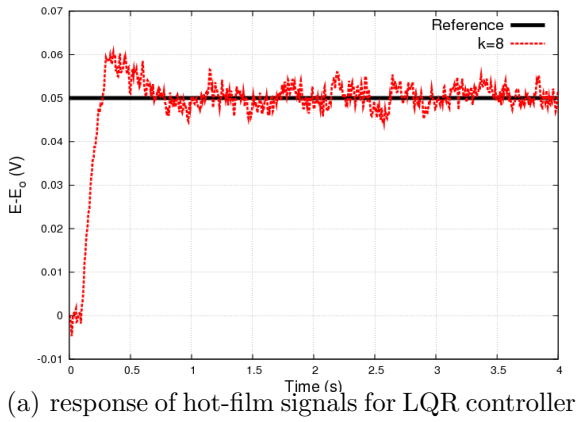

(a) response of hot-film signals for LQR controller with $K = 8$

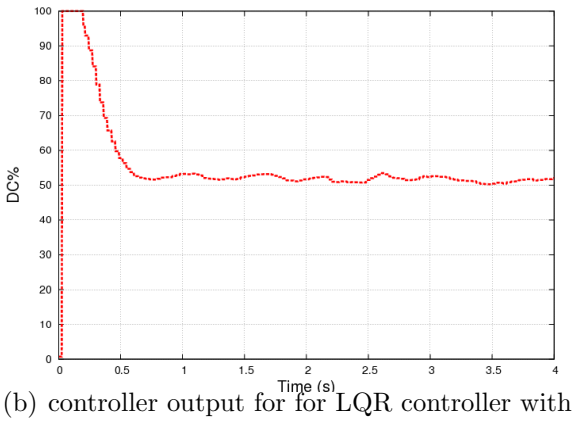

(b) controller output for for LQR controller with $K = 8$

Figure 5.19: Closed-loop system response for LQR controller with $K = 8$ at $U_\infty = 10m/s$

5.2.2 Adaptation to variations of free stream velocity

The velocity variation was introduced to check the robustness of the tested controllers due to external disturbances. Two types of disturbances were tested. The first one is a small variations of the free stream velocity with a constant reference. The second one introduces larger variations of free stream

Controller	Gain	U_∞ (m/s)	Reference
P	$K_p = 1$	4.2-5.8	0.0355
LQR	$K = 8$	4.2-5.8	0.0355

Table 5.11: Closed-loop experiments for pulsed jet with $f = 15\,Hz$ and $VR = 3.58$, at variable free stream velocity around $U_\infty = 5m/s$, each test was 100 packets of 25 s at $f_{acq} = 200Hz$

velocity while the reference is updated by the free stream velocity. In the following, only the best controllers will be used; P controller with $k_p = 1$ and LQR controller with $K = 8$.

Small variations

Table 5.11 lists the closed-loop experiments at variable free stream velocity around $U_\infty = 5m/s$. The small fluctuations were obtained by varying the wind-tunnel fan. The velocity range was $4.2\ m/s < U_\infty < 5.8\ m/s$. The free stream velocity was acquired simultaneously with the controller output and the controlled variable, in order to compare results.

Figure 5.20 shows the closed-loop response for P controller with $k_p = 1$. The free stream velocity perturbation is shown in figure 5.20(a). This is a multi-parameter problem, because the hot-film response depends on the free stream velocity and also VR, since the jet velocity is constant during the experiments. The last parameter is the controller output, that is the duty cycle DC. It is clearly seen in figure 5.20(b) that the response is stabilised for the first 5 s due to no free stream velocity change. Then the free stream velocity starts to increase which consequently makes the hot-film response to increase. Meanwhile, VR is decreasing and is trying to decrease the hot-

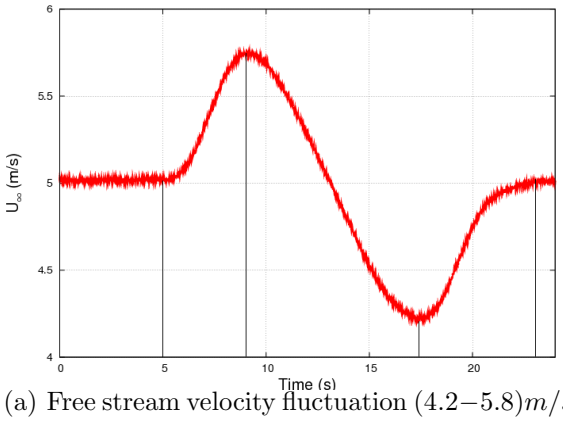

(a) Free stream velocity fluctuation $(4.2-5.8) m/s$

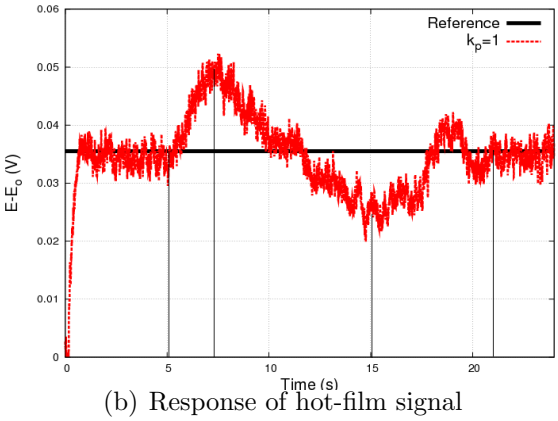

(b) Response of hot-film signal

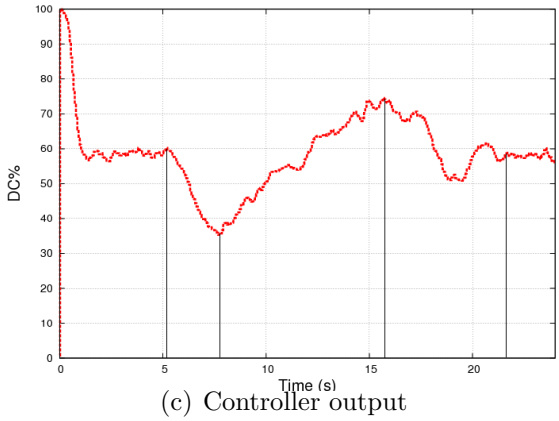

(c) Controller output

Figure 5.20: Closed-loop system response for P controller with $k_p = 1$ at variable free stream velocity $4.2\, m/s < U_\infty < 5.8\, m/s$

film signal (section 5.1.1). Therefore the controller reacts for this change by decreasing the DC to force the response to follow the reference. However, this reaction from the controller is much slower than the one at the beginning of the signal. And so, the response starts to decrease at $t = 7\, s$, just before the peak of the free stream velocity, which corresponds to $t = 9\, s$. Then the free stream velocity decreases that pushes the response to decrease further. Meanwhile, the controller is increasing the DC to track the reference, that

makes the reference again increase at $t = 15\,s$, just before the peak of the free stream velocity, which corresponds to $t = 17.5\,s$. Finally, the controller succeed only to stabilise the response when the perturbation is finished. The same experiment was repeated with the LQR controller with $K = 8$, and we had almost the same results.

Large variations

When there is a variation of the free stream velocity, the shear at the location of the separation is modified. Hence, when varying from one free stream velocity to a lower one, the mass flow rate introduced is over estimated. In order to keep the control action in optimal condition under large variation of free stream velocity ($U_\infty > 1\,m/s$), the reference has to be updated. A closed-loop experiment was performed as a demonstrator using a rough calibration of the evolution of the reference with the free stream velocity based on wool tufts visualisations as depicted in figure 5.21(b). Results of the control presented in figure 5.21 shows that the controller is able to track the reference in the presence of large velocity variations. But at $t > 18\,s$, there is a slight steady state error, even though the controller starts to react for this error by increasing the DC as can be seen in figure 5.21(d). It is clear that the controller output almost converged to DC=50% with this specific reference law. Other reference laws can be imposed to adapt the controller output to variations of free stream velocity. For example, the reference law can be modified to have easily, DC=50%, 60% and 70% at $U_\infty = 7\,,8$ and $9\,m/s$, respectively.

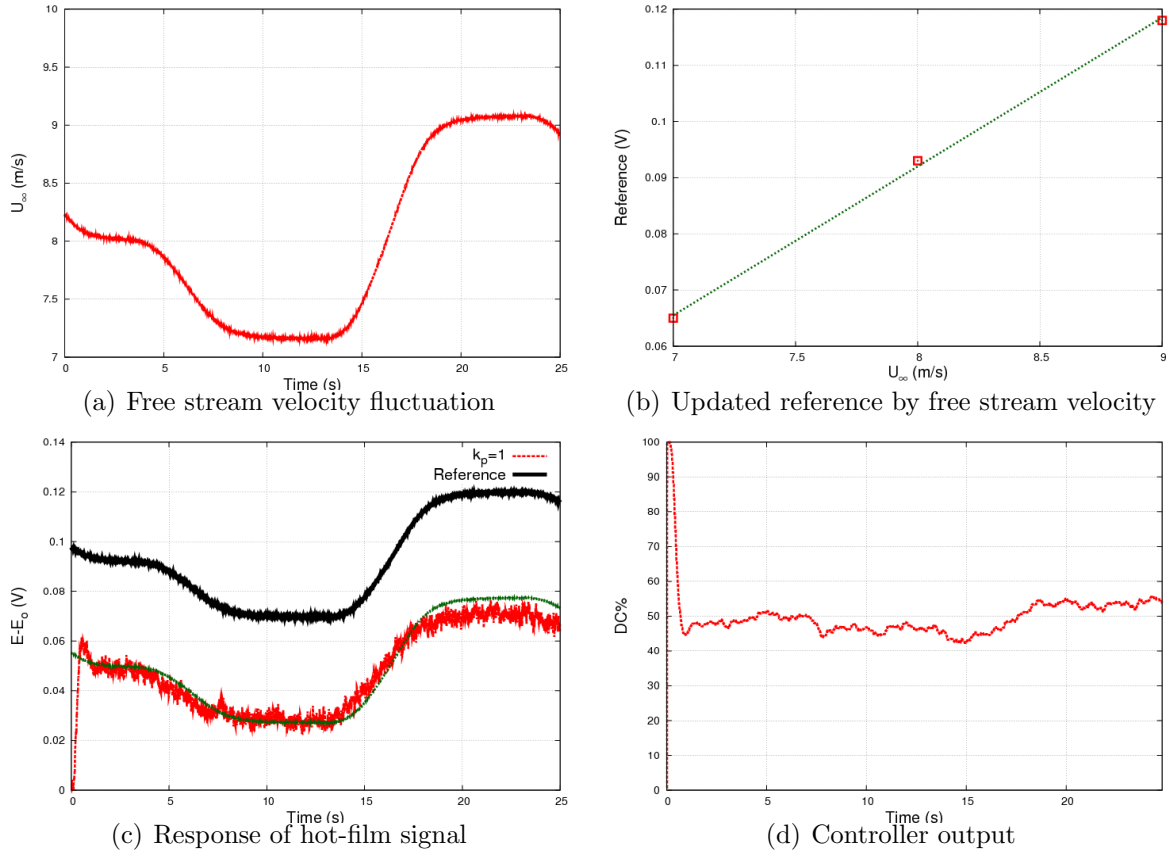

(a) Free stream velocity fluctuation

(b) Updated reference by free stream velocity

(c) Response of hot-film signal

(d) Controller output

Figure 5.21: Closed-loop system response for P controller with $k_p = 1$ at variable free stream velocity $U_\infty = (7 - 9)m/s$ and with variable reference

5.2.3 Conclusion on closed-loop

Closed-loop separation control experiments have been conducted over the ramp using pulsed jet actuators. The control reactivity at constant free stream velocity is improved compared to open-loop control. The robustness of the controller is tested under variations of the free stream velocity. For small velocity variations, the controller reacts to the velocity perturbations, but it is not fast enough to track the reference, nevertheless it succeeds to stabilize the response when the perturbations is finished. Further improvement

on the controller will be done in the next chapter to have better tracking. For large velocity variations, the reference is updated as a function of the velocity. Consequently, the controller is successful to track the reference.

In the present work, we have selected the actuation frequency in the optimal range for all tested free stream velocities. The present actuator would enable us to adapt simultaneously both parameters (f and reference) which opens some possibilities for future investigations.

Chapter 6

Modeling and Simulation

In this chapter, we formulate the control problem for the separated flow over the ramp model and find the mathematical representation of the system based on experimental data. Experimentally, the parametric variation was limited by necessity and time. Having identified the system, it is interesting to perform simulations in order to assess the performance of the different controllers used and to investigate possibilities to improve them. Several types of controller will be designed, and then the closed loop system will be simulated for each controller. The designed controllers range from the conventional PID to the modern state feedback controller and then, the H_∞ controllers. Finally, a general linear parameter varying model will be proposed to improve the robustness. It will be formulated and an LMI-based H_∞ LPV controller will be implemented in that model.

6.1 System Modeling

In this section a mathematical model is formulated in order to use model based control techniques that provides control laws to delay separation. The

controlled variable is $E - E_o$, and the manipulated variable is the duty cycle of the actuator as was explained in section 5.1.1. The input-output linearity was also checked in that section.

At $U_\infty = 5\,m/s$, the whole system behaves like a linear first order system as shown in figure 6.1(a), and can be fitted using equation 6.1.

$$y(t) = -0.069(e^{-1.739t} - 1) \tag{6.1}$$

The system will be formulated in state space representation as given by equation 6.2. Where x is the state variable $(E - E_0)$, u is the controller output (DC), $A \in \mathbb{R}$ and $B \in \mathbb{R}$.

$$\begin{aligned} \dot{x} &= Ax + Bu \\ y &= x \end{aligned} \tag{6.2}$$

Equation 6.1 can be compared to equation 6.3, which is the solution of the state space system represented in equation 6.2 with a step input of u =100. This input was selected in order that u varies from 0 to 100.

$$y(t) = \frac{100B}{A}(e^{At} - 1) \tag{6.3}$$

which leads to $A = -1.739$ and $B = 0.0012$.

Similarly, the system at $U_\infty = 10\,m/s$, as shown in figure 6.1(b), can be fitted using equation 6.4. This gives $A = -4.846$ and $B = 0.00501$.

$$y(t) = -0.105(e^{-4.846t} - 1) \tag{6.4}$$

Now we can write the transfer function of both systems

$$G(s)_5 = \frac{0.0012}{s + 1.739} = \frac{6.9 \times 10^{-4}}{0.575s + 1} \tag{6.5}$$

$$G(s)_{10} = \frac{0.00501}{s + 4.846} = \frac{10.34 \times 10^{-4}}{0.206s + 1} \tag{6.6}$$

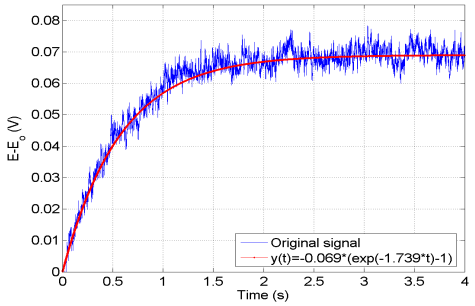

(a) $U_\infty = 5\,m/s$, VR=3.58 and DC=100%

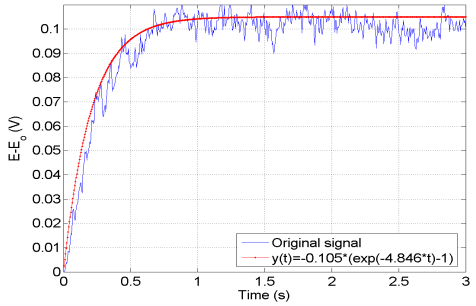

(b) $U_\infty = 10\,m/s$, VR=3.6 and DC=100%

Figure 6.1: Comparison between the original signal and curve fitting

where $G(s)_5$ is the transfer function at $U_\infty = 5\,m/s$ and $G(s)_{10}$ is the transfer function at $U_\infty = 10\,m/s$. It is clear that both systems have different time constants and steady state values which are discussed in chapter 5. The models 6.5 and 6.6 do not take into account the delay that was discussed in subsection 5.1.2. But the effect of that delay will be investigated in the next sections using Matlab Simulink.

6.2 PI Simulation Results

Consider the system $G(s)$ in equation 6.5 with the PI controller $K(s)$ in equation 3.3. Figure 6.2 gives the complete block diagram of the system; that is the model and the PI controller implementation. Also, to mimick the reality, a saturation block is added to the actuator (i.e. once the valve is selected, it has a fixed upper bound on its duty cycle). Then, another block diagram of the closed-loop model with a block for the system delay was added,in order to analyse its influence and compare it with the original model simultaneously. The closed-loop system was simulated with different k_p and k_i gains. The reference was selected to match the references chosen

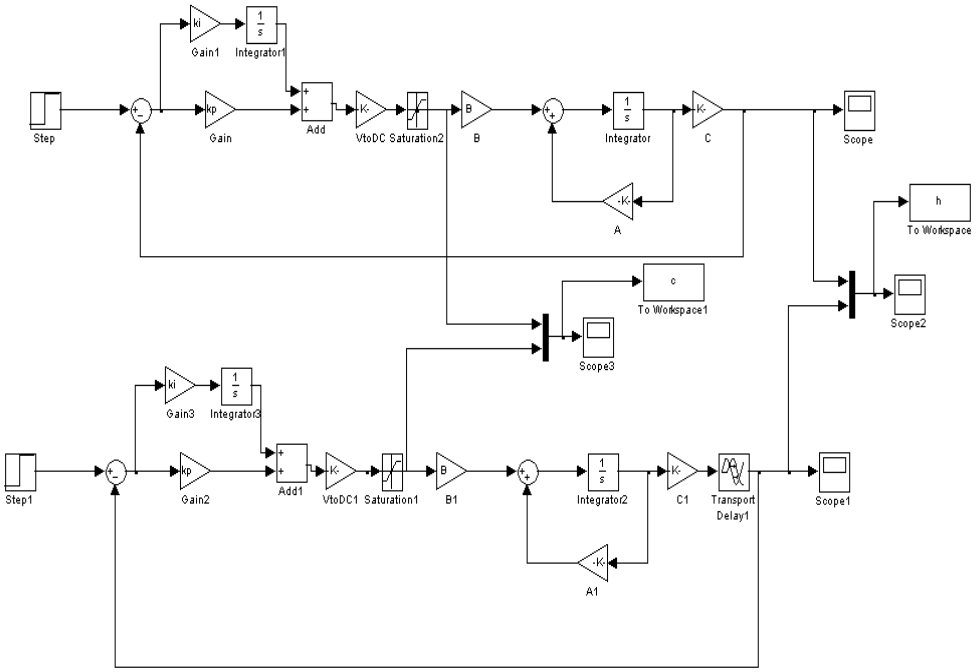

Figure 6.2: Simulink model of system with PI controller with and without system delay

in section 5.2, in order to compare the simulation results with experimental ones. Figure 6.3 shows how the settling time is decreased by increasing k_p. For example, at $k_p = 2$ the settling time is around $0.7\,s$, which is much less than in the open loop case. Figure 6.3 also shows the effect of a system delay ($0.1\,s$) on the closed loop response. That appears for $k_p = 2$, where the response has a slight overshoot.

Figure 6.4 shows how the settling time is not affected by changing k_i, it is around $5\,s$ for all tested values of k_i, which is higher than the open loop case. Figure 6.4 also shows the effect of the system delay ($0.1\,s$) on the closed loop response. The response overshoot and the settling time are increased for all

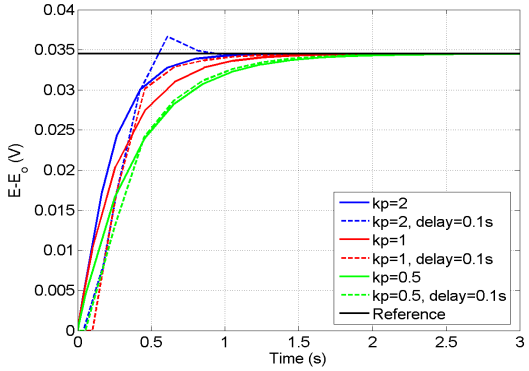

(a) response of hot-film signals due to various k_p gains

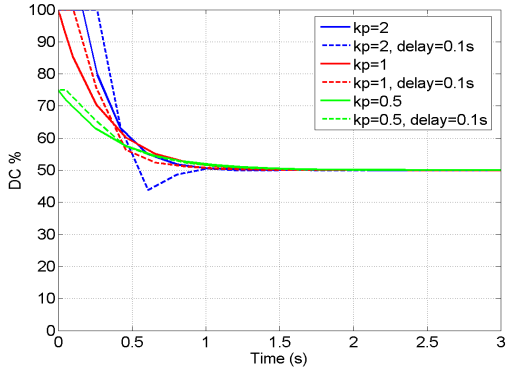

(b) controller output due to various k_p gains

Figure 6.3: Closed-loop system response for different k_p gains with and without 0.1 s system delay

tested k_i.

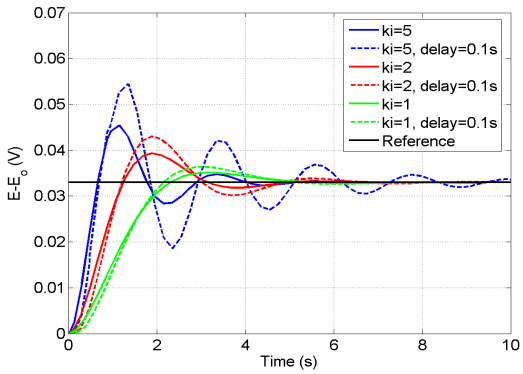

(a) response of hot-film signals due to various k_i gains

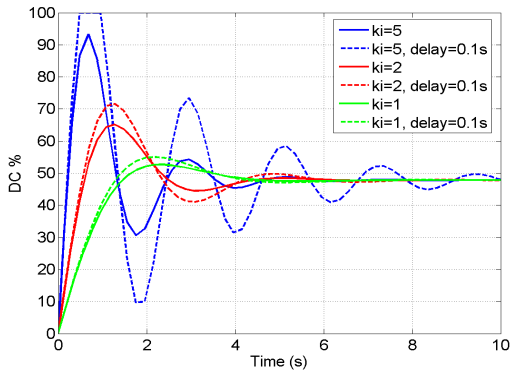

(b) controller output due to various k_i gains

Figure 6.4: Closed-loop system response for different k_i gains with and without 0.1 s system delay

As illustrated by figure 6.5, the settling time is reduced by increasing k_i and k_p. That is, for example at $k_p = 1$ and $k_i = 5$ the settling time was

around 2.5 s but accompanied with overshoot. Figure 6.5 also shows the effect of system delay (0.1 s) on the closed loop response. This is significant only for one case ($k_p = 1$ and $k_i = 5$), in which the overshoot is increased.

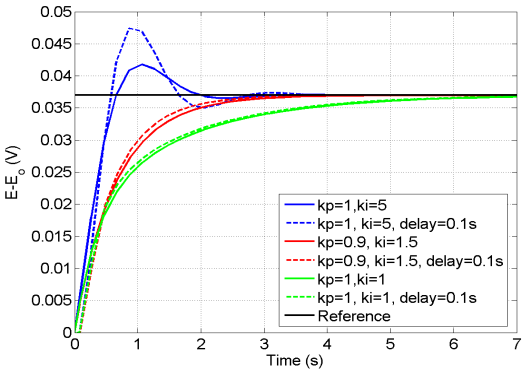

(a) response of hot-film signals due to various k_p and k_i gains

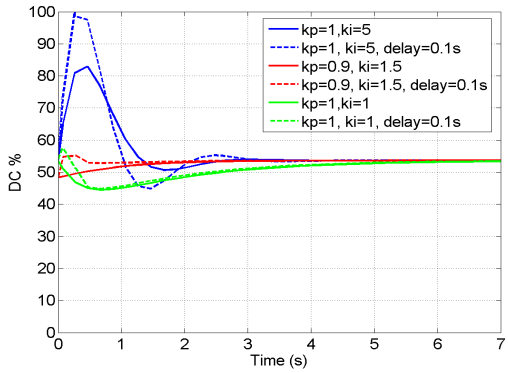

(b) controller output due to various k_p and k_i gains

Figure 6.5: Closed-loop system response for different k_p and k_i gains with and without 0.1 s system delay

When comparing figures (6.3, 5.14), (6.4, 5.15) and (6.5, 5.16), we can see that the simulation results for the system with delay almost match the experimental results. To make a better comparison, the experimental and simulation results are plotted together in figure 6.6. It is clear that the response from both experimental and simulation results are almost the same, as given in figures 6.6(a), 6.6(c) and 6.6(e). But it can be noticed that the controller output given in figures 6.6(b), 6.6(d) and 6.6(f), have some differences up to 10% between experiments and simulation, especially in the steady state. It is obvious that the linear model overestimates $E - E_o$ in the range of DC from 45 to 65%. This comes from the limitations of the linear model approximation of the input/output relation that is given in figure 5.4(b).

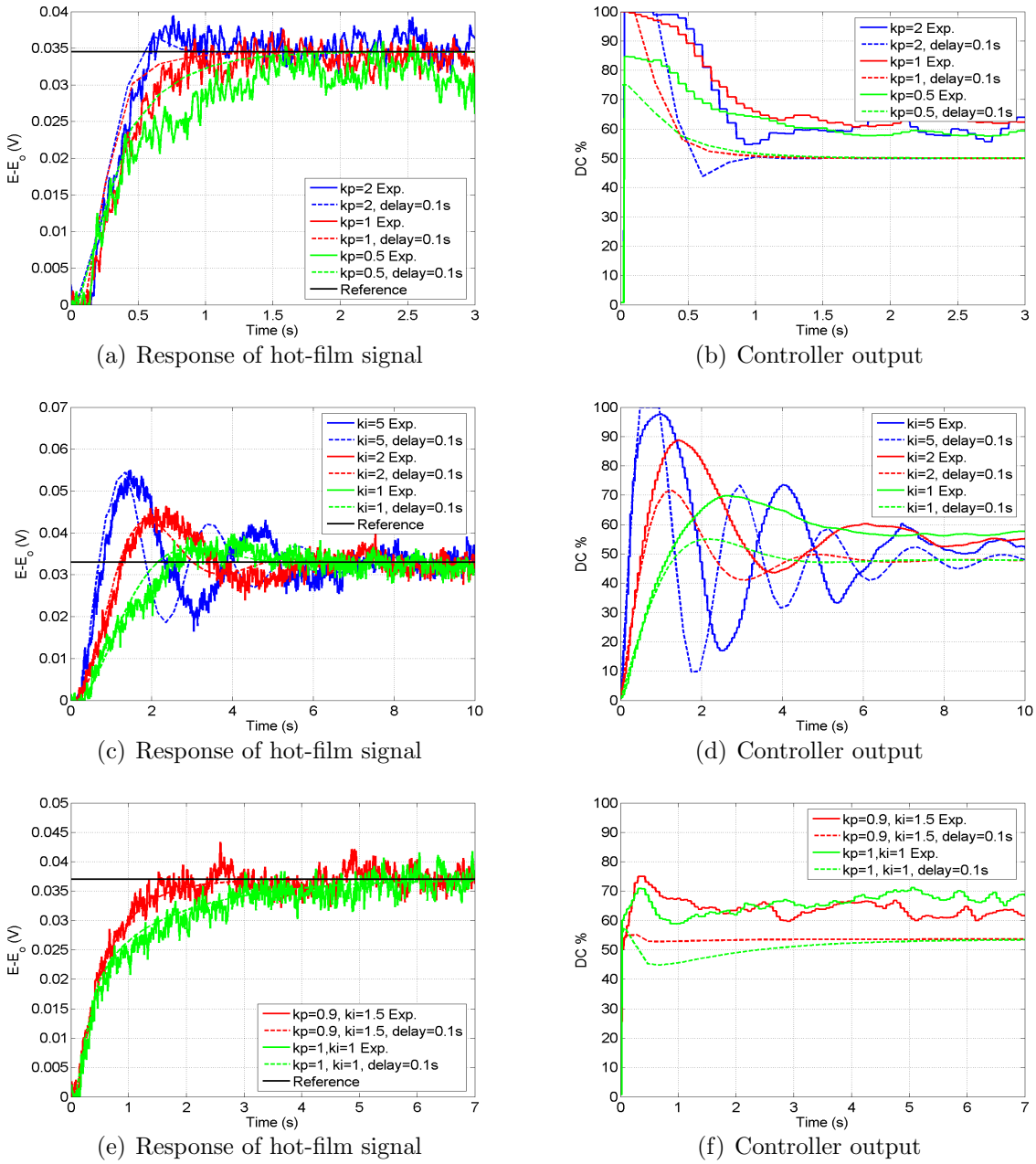

(a) Response of hot-film signal

(b) Controller output

(c) Response of hot-film signal

(d) Controller output

(e) Response of hot-film signal

(f) Controller output

Figure 6.6: Comparison between experimental and simulation results for the closed-loop system with PI controller

To summarize, in this section the closed-loop system with PI controller was simulated for different values of k_p and k_i. Comparison was done between the original model and the model with time delay. The model with time delay was found to be much more descriptive of the real separated flow system. The gains and references were selected to match the ones used for the experiments. Then, the experimental and simulated closed-loop response were compared and validated. For the controller output, differences up to 10% between experiments and simulation are observed in the steady state. This was already explained previously. This emphasises the practical interest of uncertain models in the future work, to take into account of the model uncertainties.

6.3 LQR Simulation Results

LQR is an efficient tool for stabilizing the system and improving systems performance. It has the ability to modify the response by choosing different values for the weighting matrices (Q, R), depending on the demands of the application, such as fast closed-loop response or minimum control effort. In the present work, minimum settling time is the major objective. The theory of LQR was reviewed in chapter 3. Consider the system $G(s)$ in equation 6.5, which has the state space realization 6.2, with the state feedback controller K in equation 3.14 that results from choosing the weighing matrices Q and R and solving the Riccati equation 3.15. In very simple cases, the Riccati equation can be solved directly, but usually numerical solution is required. In this work MATLAB code "lqr" was used to solve the LQR problem as depicted by the block diagram in figure 6.7. Figure 6.7 illustrates the complete block diagram of the system, including the model and the LQR

controller implementation.

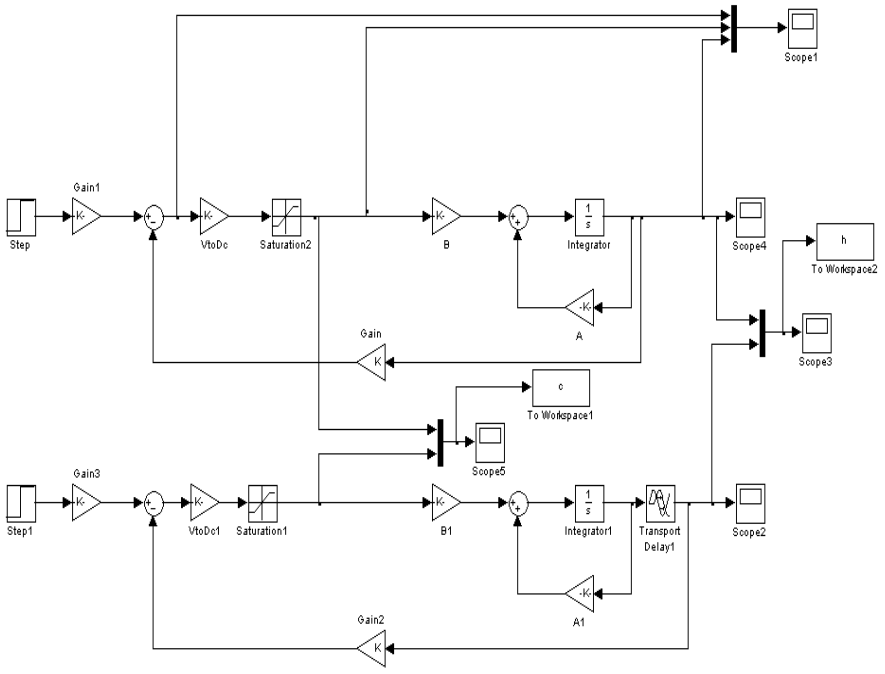

Figure 6.7: Simulink model of system with LQR controller with and without sensor delay

Several values of (Q, R) were tested to design a controller that achieves the objective. Only the most interesting results are presented. The simulation was carried out with $Q = 6700$ and 23500, while fixing $R = 1$, which means that we were seeking fast response. Consequently, the corresponding state feed-back gain K was 2.3 and 8 respectively, resulting from solving Ricatti equation 3.15. Figure 6.8 shows how the settling time decreased by increasing K, for example, at $K = 8$ the settling time is $0.6\,s$ and at $K = 2.3$ it is $0.9\,s$. Figure 6.8 also shows the effect of system delay ($0.1\,s$) on the closed-loop response. It reduces the stability margins of the closed-loop sys-

tem. This appears clearly for $K = 8$, where the response has a 7% overshoot and starts to oscillate.

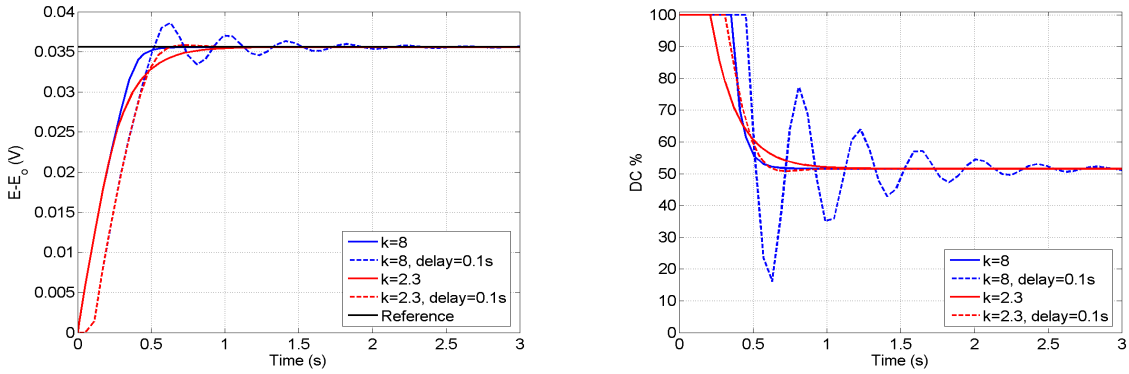

(a) Response of hot-film signal (b) Controller output

Figure 6.8: Closed-loop system response for different LQR controllers with and without 0.1 s system delay

The closed-loop experimental and simulation results for the system with time delay are plotted together in figure 6.9. For $K = 2.3$, the closed-loop response is almost the same for both cases, while the controllers output shows differences which have the same origin as for the PI controller. But for $K = 8$, the response and the controller output look different. The simulation leads to more oscillations.

The closed-loop system with LQR controller was simulated for different K. The simulations show that the response is relatively sensitive to the delay, which induces a strong oscillations for $K = 8$. As a conclusion, the linear model gives a good approximation of the real system, but further investigations of the effect of the system delay should be done in the future.

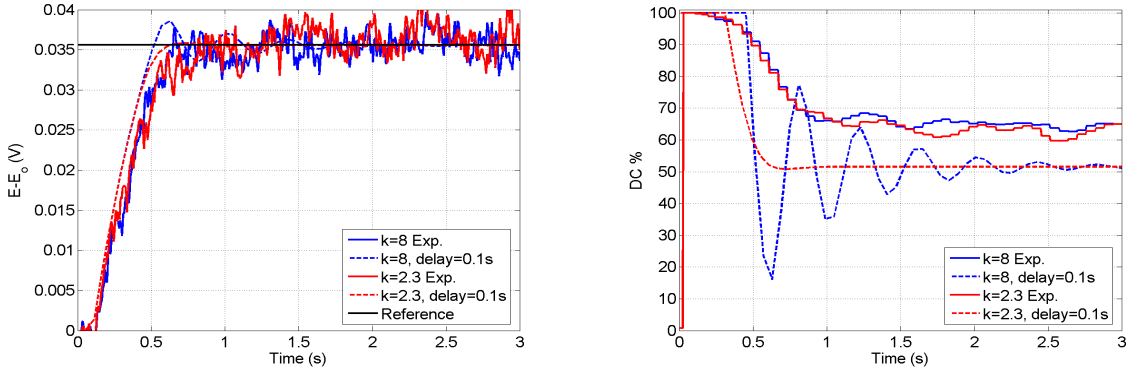

(a) Response of hot-film signal (b) Controller output

Figure 6.9: Comparison between experimental and simulation results for LQR controller

6.4 H_∞ Simulation Results

In order take into account for the noise and the external disturbances, a robust control structure can be used as was explained in section 3.4. In the following, a set of H_∞ controllers are designed for both systems; at $U_\infty = 5\,m/s$ and $U_\infty = 10\,m/s$. The general state space representation in equation 3.21 is listed below for both systems.

At $U_\infty = 5\,m/s$,

$$\begin{aligned} \dot{x}_p &= [-1.739]\,x_p + \begin{bmatrix} 0.04419 & 0 & 0 \end{bmatrix} w + [0.04419]\,u \\ z &= \begin{bmatrix} 0.02715 \\ 0 \end{bmatrix} x_p + \begin{bmatrix} 0 & 0 & 0 \\ 0 & 0 & 0 \end{bmatrix} w + \begin{bmatrix} 0 \\ 1 \end{bmatrix} u \\ y_p &= \begin{bmatrix} -0.02715 \end{bmatrix} x_p + \begin{bmatrix} 0 & -1 & 1 \end{bmatrix} w + [0]\,u \end{aligned} \tag{6.7}$$

and at $U_\infty = 10\,m/s$,

$$\begin{aligned}
\dot{x}_p &= [-4.846]\, x_p + \begin{bmatrix} 0.0884 & 0 & 0 \end{bmatrix} w + [0.0884]\, u \\
z &= \begin{bmatrix} 0.0576 \\ 0 \end{bmatrix} x_p + \begin{bmatrix} 0 & 0 & 0 \\ 0 & 0 & 0 \end{bmatrix} w + \begin{bmatrix} 0 \\ 1 \end{bmatrix} u \\
y_p &= \begin{bmatrix} -0.0576 \end{bmatrix} x_p + \begin{bmatrix} 0 & -1 & 1 \end{bmatrix} w + [0]\, u
\end{aligned} \tag{6.8}$$

The aim is to design a controller so that the H_∞ norm from w to z is minimized. A suboptimal Riccati-based H_∞ controller can be computed by using the Matlab command "hinfsyn" which solves the existence conditions for the suboptimal H_∞ controller in theorem 3.4.1. For the system 6.7 at $U_\infty = 5\, m/s$ we get the suboptimal $\gamma = 0.0008$ and the suboptimal controller

$$\begin{aligned}
\dot{x_c} &= [-0.7418]x_c + [-8.3783 \times 10^{-6}]y_p \\
u &= [-2.8020 \times 10^{-5}]x_c + [0]y_p
\end{aligned}$$

Figure 6.10 shows the closed loop response, controller output, feed-back signal which is corrupted by noise and frequency response of S, T, KS, and SP, where $KS = K \times S$ and $SP = S \times P$. S (sensitivity function), T (complementary sensitivity function) and P (plant) were defined in subsection 3.4.1. The noise used in the simulation for all the H_∞ controllers, is a white noise with $\sigma = 3.14\, V$, where σ is the standard deviation. It was selected to be much stronger than the fluctuations of the real hot-film signal where $\sigma = 0.03\, V$. As can be seen from figure 6.10 that settling time is around $7\, s$, which is much longer than the open-loop case. But as a difference to PI and LQR, the controller is efficient to overcome the effect of system delay, as the $0.1\, s$ time delay has no effect on the settling time.

For the system 6.8 at $U_\infty = 10\, m/s$ we get the suboptimal $\gamma = 0.0011$

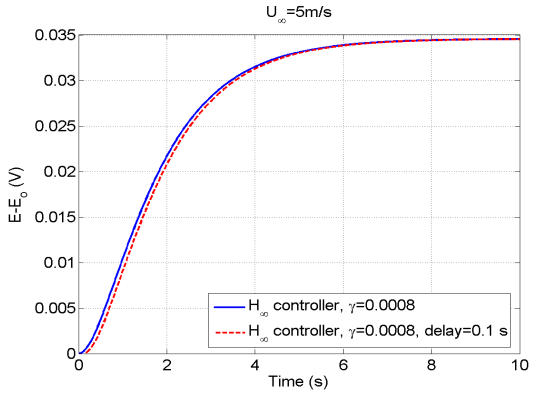

(a) Response of hot-film signal

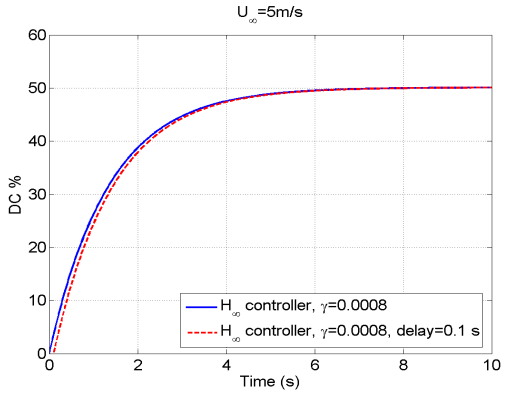

(b) Controller output

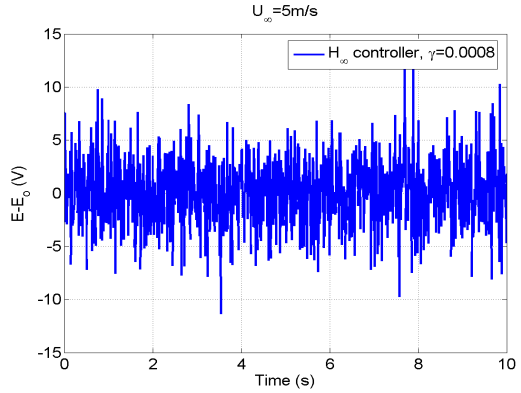

(c) Measured signal that is fed back to the controller

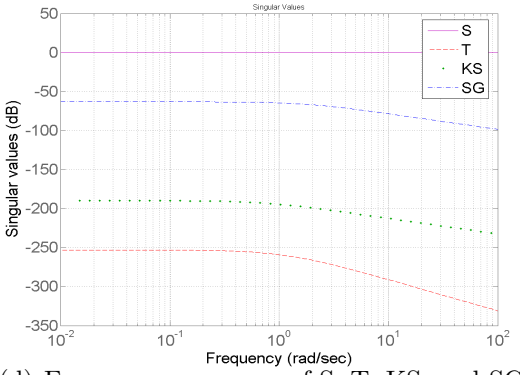

(d) Frequency responses of S, T, KS, and SG

Figure 6.10: Closed-loop system response at $U_\infty = 5m/s$ for H_∞ controller solved by "hinfsyn" with and without $0.1\,s$ system delay

and the suboptimal controller

$$\dot{x_c} = [-0.8887]x_c + [-3.1646 \times 10^{-5}]y_p$$
$$u = [-2.0420 \times 10^{-4}]x_c + [0]y_p$$

Figure 6.11 shows the closed loop response, controller output, feed-back signal corrupted by noise and frequency response of S, T, KS, and SP. The figure shows that the settling time is around $5\,s$ which does not bring improvements on the performance compared to open-loop.

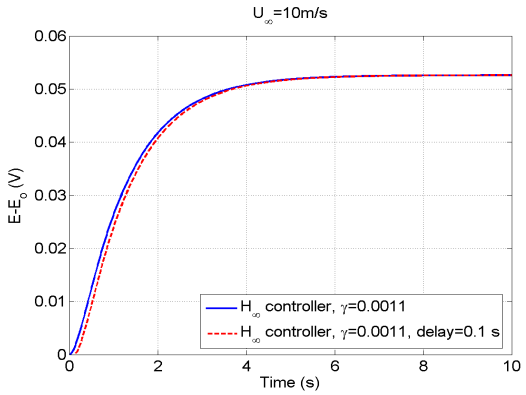

(a) Response of hot-film signal

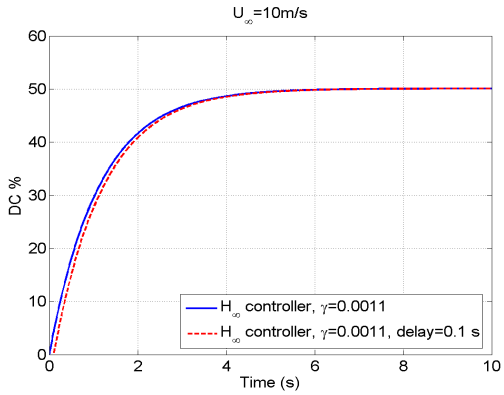

(b) Controller output

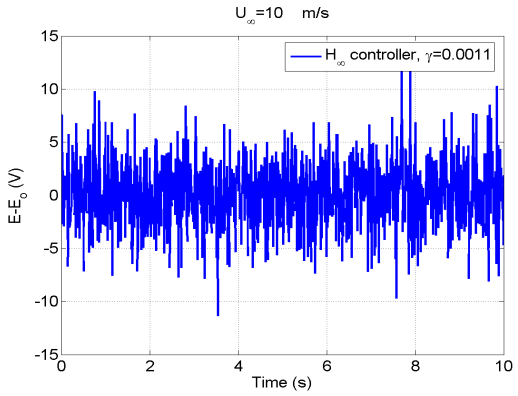

(c) Measured signal that is fed back to the controller

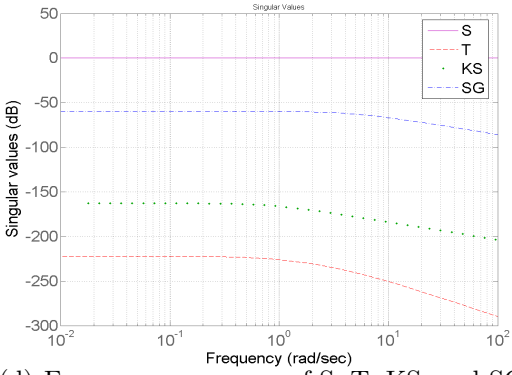

(d) Frequency responses of S, T, KS, and SG

Figure 6.11: Closed-loop system response at $U_\infty = 10m/s$ for H_∞ controller solved by "hinfsyn" with and without $0.1\,s$ system delay

A suboptimal LMI-based H_∞ controller can be computed by solving the existence conditions for the suboptimal H_∞ controller in theorem 3.4.2. A code was generated for this purpose with aid of LMI toolbox in Matlab. The code was used for the system 6.7 at $U_\infty = 5\,m/s$, and we get the suboptimal

$\gamma = 0.0098$ and the suboptimal controller

$$\dot{x_c} = [-1.7348]x_c + [3.7139 \times 10^{-6}]y_p$$
$$u = [2.8868 \times 10^{-5}]x_c + [0]y_p$$

Figure 6.12 shows the closed loop response, controller output, feed-back signal corrupted by noise and frequency response of S, T, KS, and SP. The settling time is around $4\,s$, it is improved compared to the previous controller but still higher than in the open-loop case.

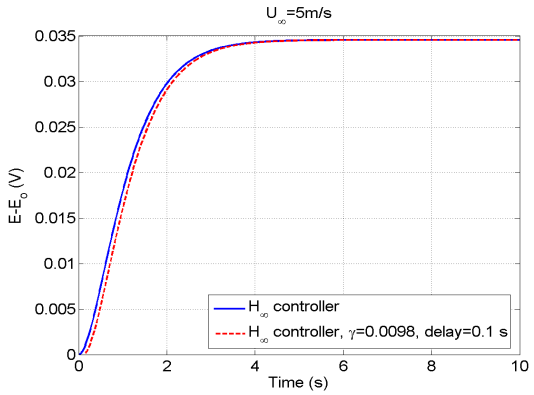

(a) Response of hot-film signal

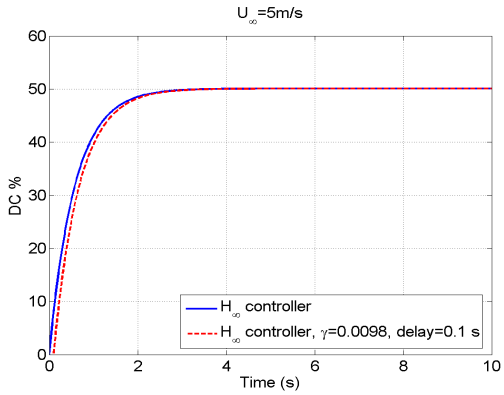

(b) Controller output

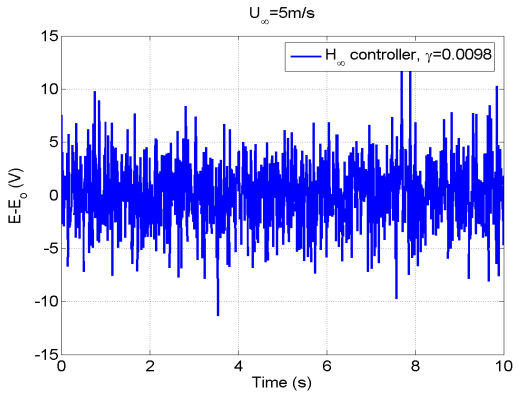

(c) Measured signal that fed back to the controller

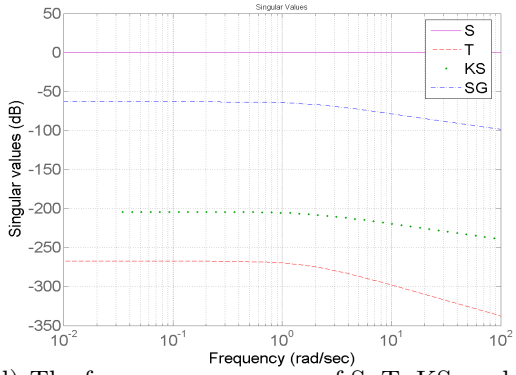

(d) The frequency responses of S, T, KS, and SG

Figure 6.12: Closed-loop system response at $U_\infty = 5\,m/s$ for the LMI-based H_∞ controller with and without $0.1\,s$ system delay

Also the code was used for the system 6.8 at $U_\infty = 10\,m/s$, and we get the suboptimal $\gamma = 0.0098$ and the suboptimal controller

$$\dot{x_c} = [-7.0521]x_c + [2.8588 \times 10^{-6}]y_p$$
$$u = [0.0025]x_c + [1.1969 \times 10^{-21}]y_p$$

Figure 6.13 shows the closed loop response, controller output, feed-back signal corrupted by noise and frequency response of S, T, KS, and SP. The settling time is now around $1.3\,s$, which is an improvement compared to the previous controller but still longer than the open-loop case.

By comparison of the frequency response of all the H_∞ controllers, it is obvious that they all behave the same approximately. They all have the ability to attenuate the high frequency disturbances (noise), which is important matter in the separated flow problem. But on the other hand, they have poor ability of attenuating low frequency disturbance, which is evident from the frequency response of the sensitivity transfer function for all the controllers. Regarding the time response of the controllers, it is clear that the LMI-based H_∞ controller have the fastest response with respect to other H_∞ controllers. It can be noticed that the tested H_∞ controllers did not improve the performance in terms of settling time compared to PI and LQR controllers. But it has more ability to attenuate high frequency disturbances and to overcome the system delay.

The performance and robustness of the H_∞ controllers can be further improved by taking into account the uncertainty of the model and by using weighted H_∞ controllers. This can be interesting when implementing these controllers experimentally in the future.

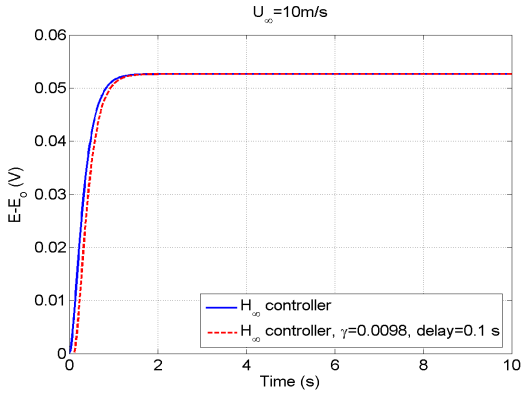

(a) Response of hot-film signal

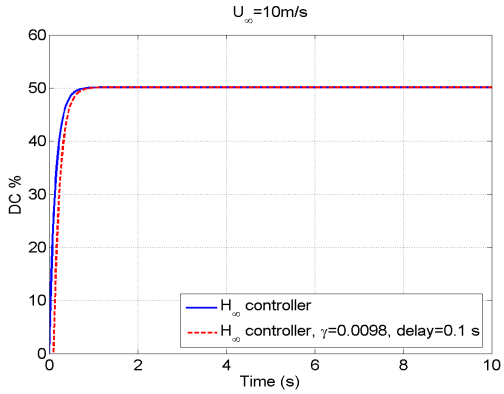

(b) Controller output

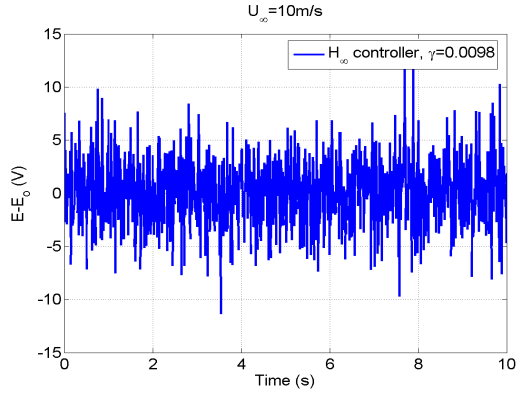

(c) Measured signal that fed back to the controller

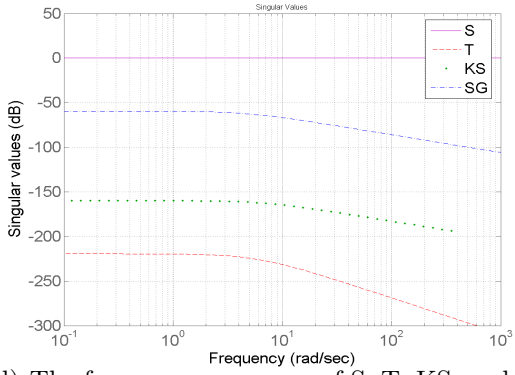

(d) The frequency responses of S, T, KS, and SG

Figure 6.13: Closed-loop system response at $U_\infty = 10\,m/s$ for the LMI-based H_∞ controller with and without $0.1\,s$ system delay

6.5 Linear Parameter Varying control

The tested models in the previous section and consequently the controllers, are only valid for fixed free stream velocity. During the experiments, the robustness of the controllers (PI and LQR) was tested by varying the free stream velocity. The results showed that the controller was able recover from such perturbation but with significant delay. This can be partially explained by the fact that we have a different model at each different free

stream velocity. So it is worth making a more general model that will be valid for a certain range of free stream velocities. In the LML wind tunnel the maximum velocity is $10\,m/s$, so the range from $5\,m/s$ to $10\,m/s$ can be satisfactory. One way to make a generic model that takes into account the free stream velocity as a parameter is the linear parameter varying (LPV) system.

Plants often depend on parameters that may vary during the operation. Thus, the plant can have varying dynamics over the operating range. The models discussed before, are linear time-invariant (LTI) models that produce LTI controllers. LTI controller cannot maintain performance over the entire operating range, while LPV model produces LPV controller that takes into account the variable dynamics of the plant and perform well over the entire operating range. One of the main reasons for LPV control theory being the subject of increasing interest is that performance analysis and controller synthesis for these systems can be formulated as linear matrix inequalities. LMIs pose convex problems and can be efficiently solved by numerical software such as the MatLab LMI toolbox (Gahinet et al. [1995]). The separated flow system depends on the free stream velocity as was discussed in section 5.1.2, in which the system will be reformulated as LPV system.

6.5.1 LPV Systems

LPV systems are linear time-varying plants whose system matrices are functions of a varying vector of parameters (Abdalla et al. [2000]). Physical models of a system often lead to a state-space description of its dynamical behaviour. The resulting state-space equations typically involve physical parameters whose value is only approximately known, as well as approximations of complex and possibly non-linear phenomena. In other words, the system

is described by an uncertain state-space model:

$$\begin{aligned} \dot{x} &= Ax + Bu \\ y &= Cx + Du \end{aligned} \tag{6.9}$$

where the state-space matrices A, B, C and D depend on uncertain and/or time-varying parameters or vary in some bounded sets of the space of matrices (Gahinet et al. [1995]). One type of LPV system is the Polytopic systems, Polytopic system is a linear parameter varying system of the form

$$\begin{aligned} \dot{x} &= A(P)x + B(P)u \\ y &= C(P)x + D(P)u \end{aligned} \tag{6.10}$$

where the time-varying parameter P, varies in a polytope Θ of vertices $\theta_1, ..., \theta_r$; that is,

$$P \in \Theta := Co\{\theta_1, ..., \theta_k\} := \{\sum_{i=1}^{r} \alpha_i \theta_i : \alpha_i \geq 0, \sum_{i=1}^{r} \alpha_i = 1\}$$

and the state-space matrices $A(p)$, $B(p)$, $C(p)$ and $D(p)$ range in a polytope of matrices whose vertices are the images of the vertices $\theta_1, ..., \theta_r$. In other words,

$$\begin{pmatrix} A(P) & B(P) \\ C(P) & D(P) \end{pmatrix} \in Co\left\{ \begin{pmatrix} A_i & B_i \\ C_i & D_i \end{pmatrix} := \begin{pmatrix} A(\theta_i) & B(\theta_i) \\ C(\theta_i) & D(\theta_i) \end{pmatrix}, i = 1, ..., r \right\}$$

Two conditions should be satisfied for a general LPV control design: That the parameters should be measurable and slowly varying (Apkarian et al. [1995]).

6.5.2 Mathematical Formulation

Consider the plants given in equations 6.7 and 6.8 for the systems at $U_\infty = 5$ and $10\,m/s$ respectively, which can be reformulated in one LPV plant as

following:

$$\begin{aligned} \dot{x}_p &= A(P)x_p + B_1(P)w + B_2(P)u \\ z &= C_1(P)x_p + D_{11}(P)w + D_{12}(P)u \\ y_p &= C_2(P)x_p + D_{21}(P)w + D_{22}(P)u \end{aligned} \tag{6.11}$$

with the assumption that $D_{22} = 0$. The LPV controller will have the form

$$\begin{aligned} \dot{x_c} &= A_c(P)x_c + B_c(P)y_p \\ u &= C_c(P)x_c + D_c(P)y_p \end{aligned} \tag{6.12}$$

The LMI based H_∞ controller for linear time-invariant (LTI) systems can be generalized for LPV systems (Apkarian et al. [1995]). As a consequence the theorem 3.4.2 will be generalized for LPV systems.

Theorem 6.5.1 *Let a scalar $\gamma > 0$ be given and consider the system 6.11. Then the following statements are equivalent:*

(i) There exists a controller of order n_c which stabilizes the system and yields $\|T_{zw}\|_\infty < \gamma$ along all parameter trajectories in the polytope $P \in \Theta := Co\{\theta_1, ..., \theta_k\} := \{\sum_{i=1}^r \alpha_i\theta_i : \alpha_i \geq 0, \sum_{i=1}^r \alpha_i = 1\}$.

(ii) There exists a matrix pair $(X, Y) \in \Re^{(n_p+n_c)\times(n_p+n_c)} \times \Re^{(n_p+n_c)\times(n_p+n_c)}$ such that

$$X > 0,\ Y > 0,\ XY = \gamma^2 I$$

$$\begin{bmatrix} \bar{B}_i \\ H_i \end{bmatrix}^{\perp} \begin{bmatrix} \bar{A}_i X + X\bar{A}_i^T + \bar{D}_i\bar{D}_i^T & X\bar{C}_i^T + \bar{D}_i F_i^T \\ \bar{C}_i X + F_i\bar{D}_i^T & F_i F_i^T - \gamma^2 I \end{bmatrix} \begin{bmatrix} \bar{B}_i \\ H_i \end{bmatrix}^{\perp T} < 0$$

$$\begin{bmatrix} M_i^T \\ E_i^T \end{bmatrix}^{\perp} \begin{bmatrix} Y\bar{A}_i + \bar{A}_i^T Y + \bar{C}_i^T\bar{C}_i & Y\bar{D}_i + \bar{C}_i^T F_i \\ \bar{D}_i^T Y + F_i^T\bar{C}_i & F_i^T F_i - \gamma^2 I \end{bmatrix} \begin{bmatrix} M_i^T \\ E_i^T \end{bmatrix}^{\perp T} < 0$$

for all $i = 1, ..., r$.

(iii) There exists a matrix pair $(X_p, Y_p) \in \Re^{n_p \times n_p} \times \Re^{n_p \times n_p}$ *such that*

$$\begin{bmatrix} X_p & \gamma I \\ \gamma I & Y_p \end{bmatrix} > 0$$

$$\begin{bmatrix} B_{2i} \\ D_{12i} \end{bmatrix}^{\perp} \begin{bmatrix} A_i X_p + X_p A_i^T + B_{1i} B_{1i}^T & X_p C_{1i}^T + B_{1i} D_{11i}^T \\ C_{1i} X_p + D_{11i} B_{1i}^T & D_{11i} D_{11i}^T - \gamma^2 I \end{bmatrix} \begin{bmatrix} B_{2i} \\ D_{12i} \end{bmatrix}^{\perp T} < 0$$

$$\begin{bmatrix} C_{2i}^T \\ D_{21i}^T \end{bmatrix}^{\perp} \begin{bmatrix} Y_p A_i + A_i^T Y_p + C_{1i}^T C_{1i} & Y_p B_{1i} + C_{1i}^T D_{11i} \\ B_{1i}^T Y_p + D_{11i}^T C_{1i} & D_{11i}^T D_{11i} - \gamma^2 I \end{bmatrix} \begin{bmatrix} C_{2i}^T \\ D_{21i}^T \end{bmatrix}^{\perp T} < 0$$

for all $i = 1, ..., r$. *In this case, all such controllers are given by*

$$\bar{G}_i = -R_i^{-1} \Gamma_i^T \Phi_i \Lambda_i^T (\Lambda_i \Phi_i \Lambda_i^T)^{-1} + S_i^{1/2} L_i (\Lambda_i \Phi_i \Lambda_i^T)^{-1/2}$$

where L_i *is an arbitrary matrix such that* $\|L_i\| < 1$ *and* R_i *is an arbitrary positive definite matrix such that* $\Phi_i = (\Gamma_i R_i^{-1} \Gamma_i^T - \Theta_i)^{-1} > 0$

and $S_i = R_i^{-1} - R_i^{-1} \Gamma_i^T [\Phi_i - \Phi_i \Lambda_i^T (\Lambda_i \Phi_i \Lambda_i^T)^{-1} \Lambda_i \Phi_i] \Gamma_i R_i^{-1}$,

$$\Theta_i = \begin{bmatrix} Y\bar{A}_i + \bar{A}_i^T Y & Y\bar{D}_i & \bar{C}_i^T \\ \bar{D}_i^T Y & -\gamma^2 I & F_i^T \\ \bar{C}_i & F_i & -I \end{bmatrix}, \ \Gamma_i = \begin{bmatrix} Y\bar{B}_i \\ 0 \\ H_i \end{bmatrix}, \ \Lambda_i = \begin{bmatrix} M_i & E_i & 0 \end{bmatrix}$$

6.5.3 LPV Controller Design

Consider the LPV plant given in equation 6.11, with the controller in equation 6.12. P is the vector of parameters and since we have only one parameter (U_∞) in the present case, the parameter range is a line with two vertices ($5\,m/s$) and ($10\,m/s$). A MATLAB code was generated to solve the LMIs in theorem 6.5.1 using LMI toolbox, and the Bisection method was used to minimize γ. The optimal value for the H_∞ performance index γ was found to be 0.0098. The closed-loop frequency response is given in Figure 6.14. The corresponding feasible matrix pair (X, Y) that satisfies the LMIs in theorem 6.5.1 at the two vertices is given by:

$$X = \begin{bmatrix} X_p & X_{pc} \\ X_{pc}^T & X_c \end{bmatrix} = \begin{bmatrix} 0.0355 & -0.0034 \\ -0.0034 & 0.0004 \end{bmatrix}$$

$$Y = \begin{bmatrix} Y_p & Y_{pc} \\ Y_{pc}^T & Y_c \end{bmatrix} = \begin{bmatrix} 0.0119 & 0.0960 \\ 0.0960 & 1.0000 \end{bmatrix}$$

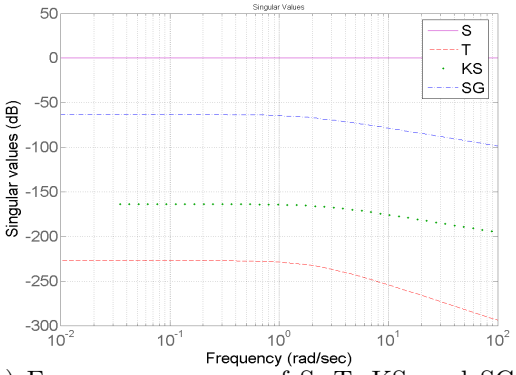

(a) Frequency response of S, T, KS, and SG at the first vertex when $U_\infty = 5m/s$

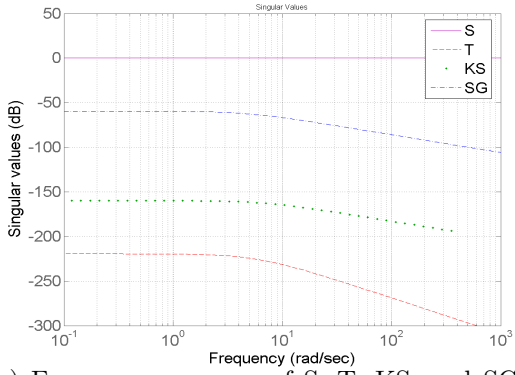

(b) Frequency response of S, T, KS, and SG at the second vertex when $U_\infty = 10m/s$

Figure 6.14: Closed-loop frequency response for LPV controller at the vertices

The controller matrices was also generated at the two vertices. The state-space matrices of the controller $K(p)$ are given by

$$\begin{pmatrix} A_c(P) & B_c(P) \\ C_c(P) & D_c(P) \end{pmatrix} := \sum_{i=1}^{2} \alpha_i K_i = \sum_{i=1}^{2} \alpha_i \begin{pmatrix} A_{ci} & B_{ci} \\ C_{ci} & D_{ci} \end{pmatrix}$$

While the vertex controllers K_i can be computed off-line, the LPV controller matrices $A_c(P)$, $B_c(P)$, $C_c(P)$, $D_c(P)$ must be updated in real time based on the parameter measurement P. The scheduling technique in hand is for

updating the controller matrices depending on the varying parameters, but we have to define α, which is

$$\alpha_1 = \frac{P_{max} - P}{P_{max} - P_{min}}, \quad \alpha_2 = 1 - \alpha_1$$

where

$$P_{max} = 10\,m/s, \quad P_{min} = 5\,m/s$$

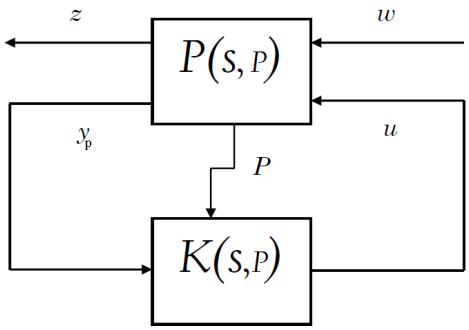

Figure 6.15: LFT scheme of the LPV system

Then by solving the controller at the vertices the LPV controller will be

$$\begin{pmatrix} A_c(P) & B_c(P) \\ C_c(P) & D_c(P) \end{pmatrix} = \alpha_1 \begin{pmatrix} -2.611 & 1.348 \times 10^{-5} \\ 0.0012 & 0 \end{pmatrix} + \alpha_2 \begin{pmatrix} -7.052 & 2.859 \times 10^{-5} \\ 0.0025 & 1.197 \times 10^{-21} \end{pmatrix}$$

6.5.4 LPV Simulation Results

The closed-loop system with the LPV controller is simulated for different free stream velocity trajectories, since the model offers the ability to simulate any velocity path, as long as it satisfies the slowly varying condition.

LPV simulation of small velocity variation

In comparison to section 5.2.2, the same velocity variation is introduced here. but since the LPV model is only valid from the 5 to $10\,m/s$, the mean of

this velocity variation has been changed to $7.5\,m/s$ instead of $5\,m/s$. The closed-loop system is simulated as shown in figure 6.16. The LPV controller performs well against velocity perturbations and it successfully tracks the reference. Compared to the experimental results obtained in section 5.2.2 with the simple PI and LQR controllers, the control efficiency is here much better, although a stronger noise is introduced in the model.

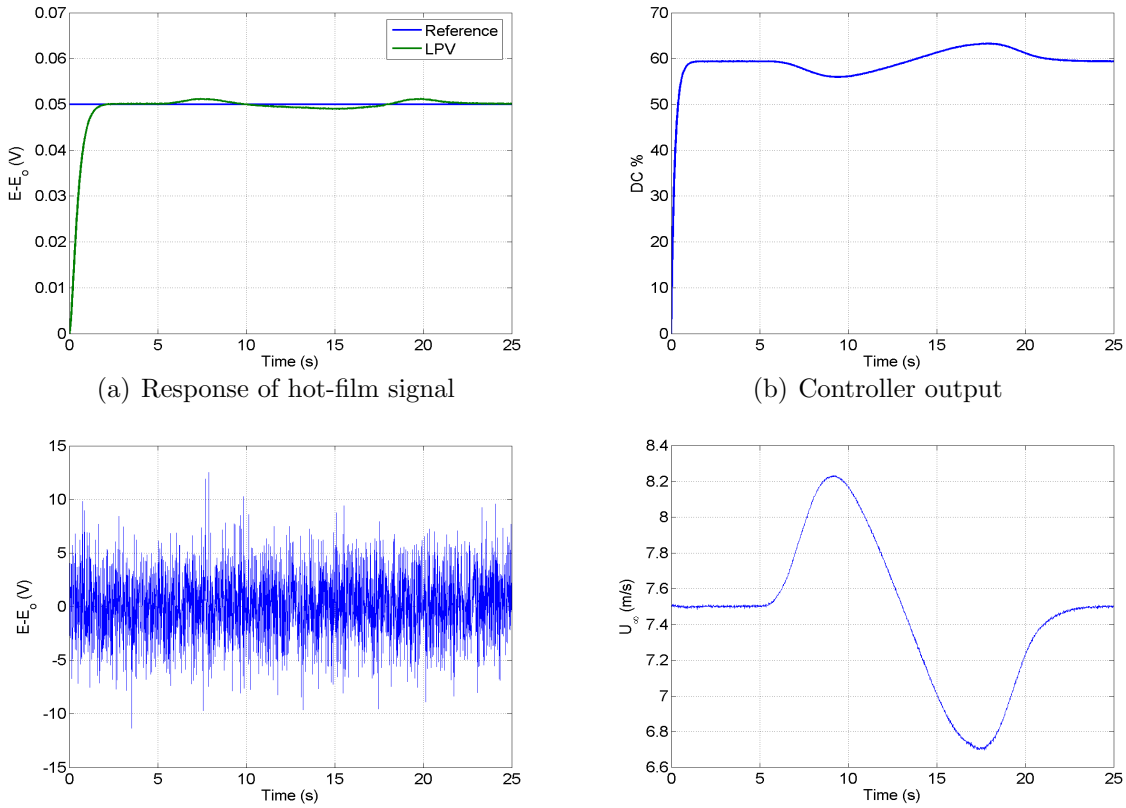

(a) Response of hot-film signal

(b) Controller output

(c) Measured signal that is fed back to the controller

(d) Free stream velocity

Figure 6.16: Closed-loop system response for LPV controller with small velocity variation

LPV simulation of large velocity variation

Different velocity trajectories are tested here (i.e increasing, decreasing and sinusoidal). As shown in figure 6.17, the simulation was performed with decreasing free stream velocity from $10\,m/s$ to $5\,m/s$, which illustrates how the controller reacts to velocity variations and also shows how the speed of response alters with velocity variation.

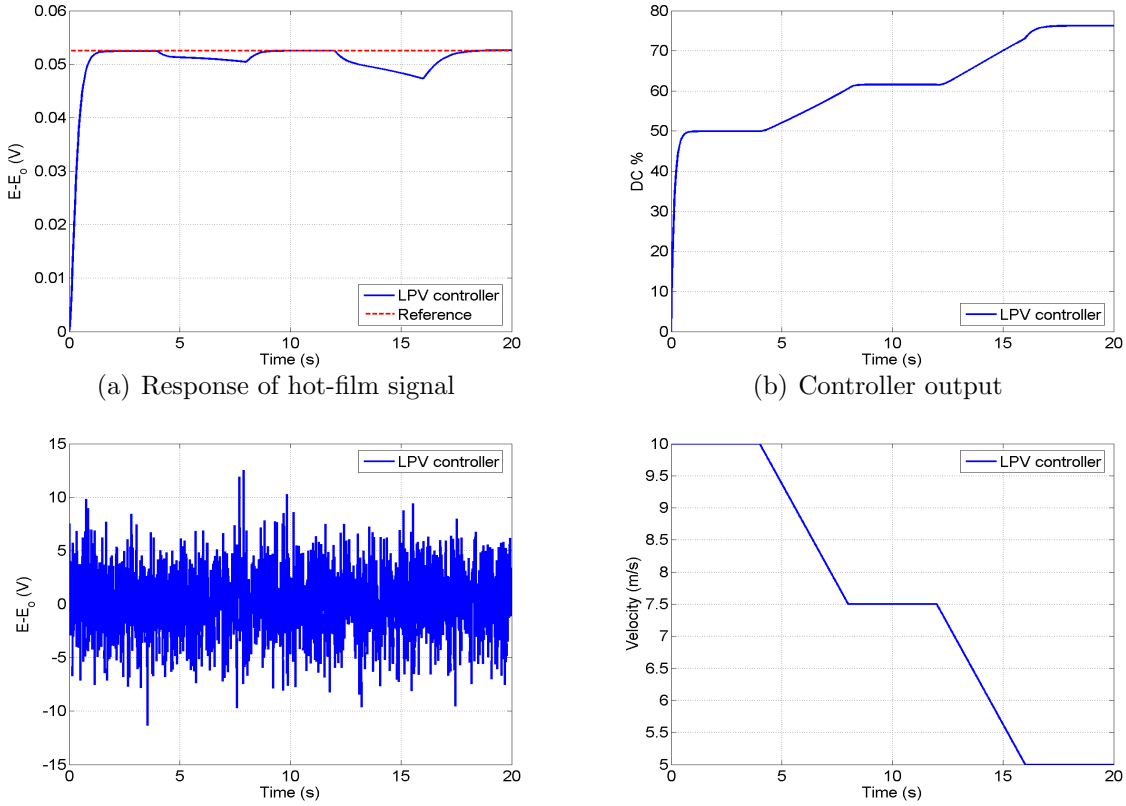

(a) Response of hot-film signal

(b) Controller output

(c) Measured signal that is fed back to the controller

(d) Free stream velocity

Figure 6.17: Closed-loop system response for LPV controller with constant reference and decreasing velocity

In figure 6.18, the simulation was performed with increasing velocity from

$5\,m/s$ to $10\,m/s$.

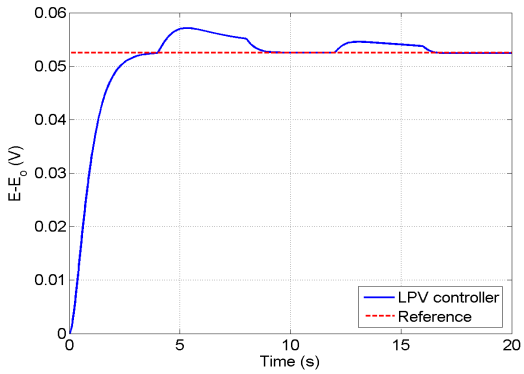

(a) Response of hot-film signal

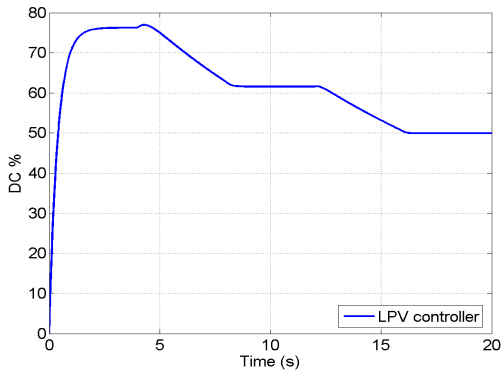

(b) Controller output

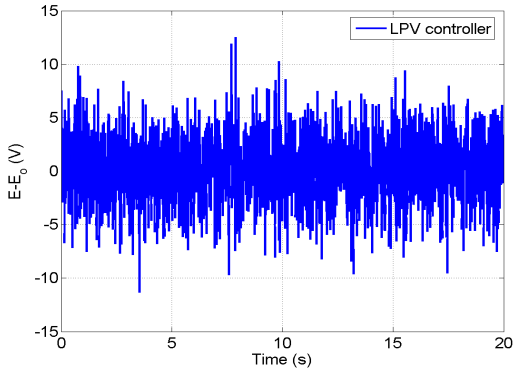

(c) Measured signal that is fed back to the controller

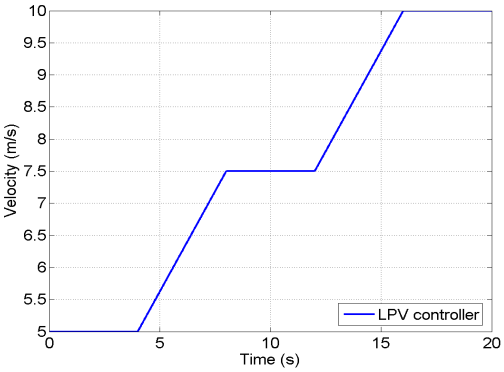

(d) Free stream velocity

Figure 6.18: Closed-loop system response for LPV controller with constant reference and increasing velocity

Figure 6.19 illustrates how the controller reacts to velocity variations around $7.5\,m/s$ and it clearly shows that the response is satisfactory.

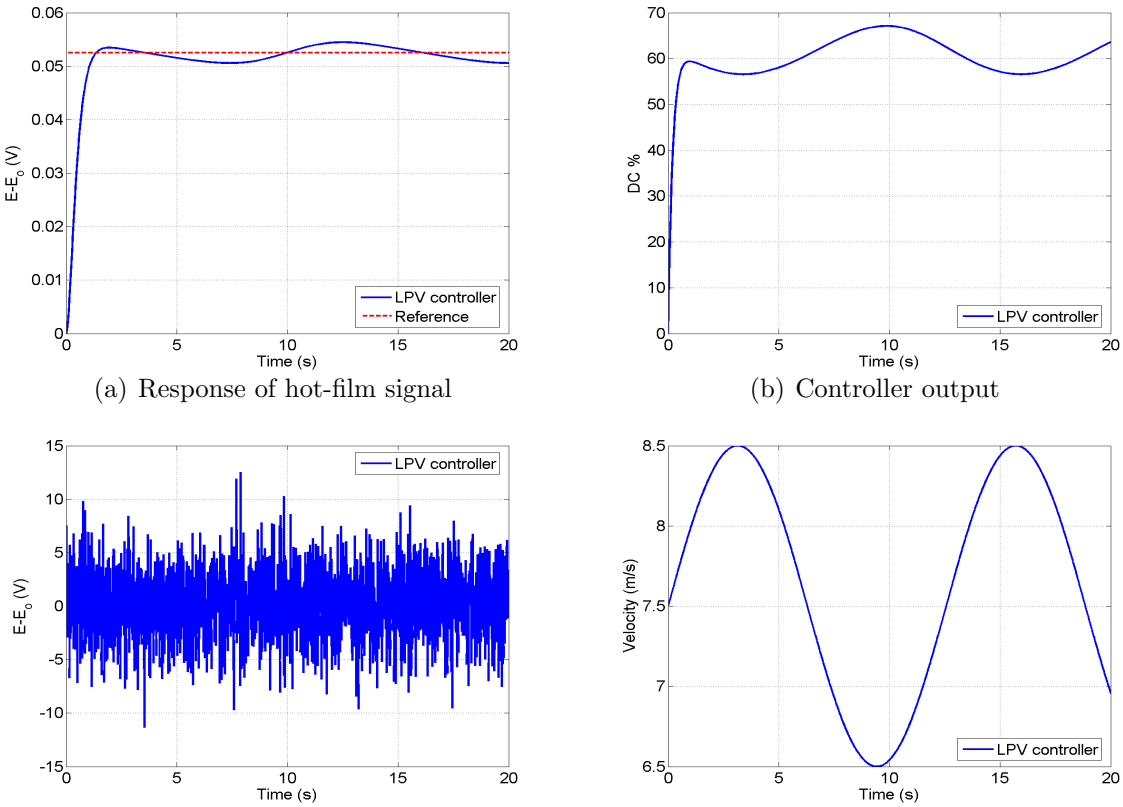

(a) Response of hot-film signal

(b) Controller output

(c) Measured signal that is fed back to the controller

(d) Free stream velocity

Figure 6.19: Closed-loop system response for LPV controller with constant reference and fluctuating velocity

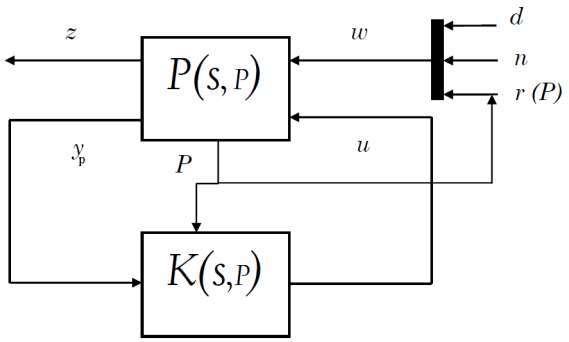

Figure 6.20: LFT scheme of the LPV system with varying reference

In the above simulations, the LPV model was based on two LTI models identified with constant velocity ratio ($VR = \frac{V_j}{U_e}$) at two free stream velocities 5 and 10 m/s. Consequently, this LPV model assumes constant VR over all free stream variation. Hence, to get the same simulation results (figures 6.17, 6.18 and 6.19) experimentally, the jet velocity has to change correspondingly with the free stream velocity in order to keep VR constant. Unfortunately, for practical implementation, this cannot be useful. One way to solve that, is to choose V_j such that it is able to attach the flow at the maximum free stream velocity. Then a new LPV model will be identified based on that.

For the previous simulations, the reference was constant. Which was chosen to attach the flow at the maximum free stream velocity in order to have an attached flow over the entire range of free stream velocities. This means that more energy is spent. Therefore, it is of interest to update the reference as a function of the free stream velocity as illustrated in figure 6.20. This can be achieved easily, since the free stream velocity is already acquired to update the LPV controller.

As depicted in figure 6.21, the simulation was performed with increasing velocity from $5\,m/s$ to $10\,m/s$ and a variable reference as a function of this velocity. The figure illustrates how the controller reacts for the velocity variation and how the speed of response alters with velocity variation. This simulation gives more realistic and optimal implementation. For this specific reference law, we assumed that blowing at $DC = 50\%$ is enough for reattaching the flow for all free stream velocities. This reference law is an example, and any other law can be implemented. In comparison to the experimental results in section 5.2.2, it should be recalled that the closed-loop response with P controller and updating the reference showed also good tracking performance (If we ignore the steady state error). It should be said, that the P

controller was tested under slow velocity variations. Whereas, for the LPV controller case, a wider range and faster variations of free stream velocity was tested, under which the controller showed good robustness. We expect that the P controller will not perform well against fast perturbations of free stream velocity, and more attention should be given for the LPV controller in the future to validate the results experimentally.

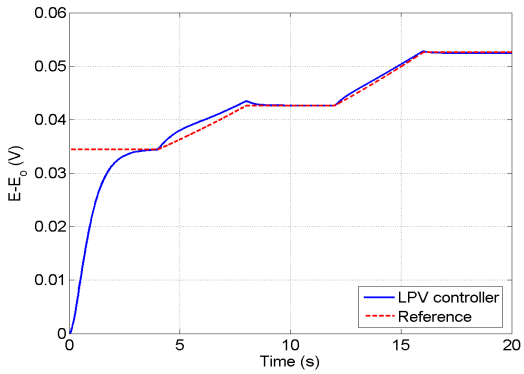

(a) Response of hot-film signal

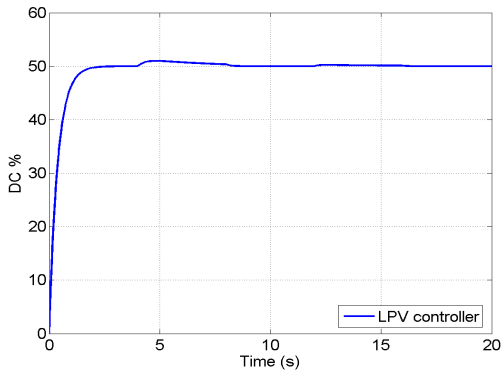

(b) Controller output

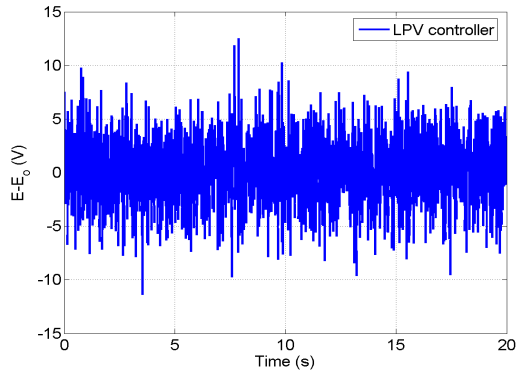

(c) Measured signal that is fed back to the controller

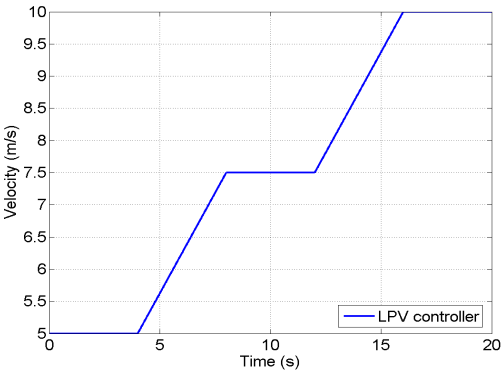

(d) Free stream velocity

Figure 6.21: Closed-loop system response for LPV controller with variable reference and increasing velocity

To summarize this simulation chapter, the system at constant free stream

velocity was first addressed as LTI system. Hence, LTI controllers were designed. Departing from the classical PI controller to the optimal LQR controller and the H_∞ controller. The closed-loop system was simulated using Simulink for all the controllers. Both PI and LQR controller do well in terms of performance, by having shorter settling time compared to open-loop system. While the H_∞ controller is more robust in terms of attenuating disturbances.

As illustrated by the experimental results with varying free stream velocity, the system dynamics changes with this variation. To try to solve this problem, LPV approach was investigated. The LMI optimal problem constrains were derived and formulated to get the controller dynamics. Finally, Simulink based simulations for the LPV system with the controller were used to verify the effectiveness of the LPV controller.

The simulated closed-loop control with the PI and LQR controllers was validated experimentally. But the simulation for Riccati-based and LMI-based H_∞ controllers still need such an experimental validation, as well as the LPV controllers. This can be a future work for more robust closed-loop control.

Chapter 7

Conclusion

Flow separation control experiments were performed to reattach a particularly thick turbulent boundary layer before separation, ($\delta = 20\,cm$), which induces high Reynolds numbers (Re_θ=12600) and large time scales. The control objective was to reattach the flow in the separated region with the minimum of mass flow rate. Open-loop tests were performed to choose the adequate Input/Output variables for closed-loop implementations and to identify the dynamic of the system for three free stream velocities. The chosen input variable was the Duty Cycle which enables us to send a control action at least 10 times faster than the time scale of the separation/reattachment process. This control action was sent using a spanwise line of 22 co-rotating jets. The chosen output variable was the voltage signal from a hot-film probe placed adequately on the flap of the wind tunnel model to give a linear response and represent the two states of the flow (i.e. attached/separated).

Thanks to the particularity of the present facility, it was possible to clearly extract the different time scales involved. The time scale of the actuators was found negligible regarding to the time scale of the separation/reattachment process, which was determined for three free stream velocities U_∞, using

open-loop experiments. For separation, the values obtained here: $t^+_{sep} = 13.8$, 20 and 17.5 at $U_\infty = 10$, 8 and 5 m/s respectively, are in good agreement in comparison to the literature, where the dimensionless time scale is $14 < t^+_{sep} < 25$. One significant difference here with the literature is that the time scales for the separation/reattachment process are found equal, while they are much shorter in the other existing experiments, but for flow configurations that are significantly different (Beveled splitter plate and airfoils). It appears that, with the existing scaling, no universal value comes out for the attachment and separation time scales as was found by Siauw et al. [2010].

The influence of velocity ratio (VR), free stream velocity (U_∞) and duty cycle (DC) on these time scales was studied in some detail. They appear dependent on VR and U_∞ and independent of DC. The higher VR (or U_∞) the shorter the time scales. The influence of the actuation frequency was also studied in the range of 6 to $100Hz$. Optimal frequencies were identified for each free stream velocity, and the most efficient and common for all cases was used in closed-loop control.

It was found that the convective time scales $t_{conv} = 0.147$, 0.13 and 0.106 s, at $U_\infty = 5$, 8 and 10 m/s respectively, are also much longer than the actuator time scale. This convective time could be reduced by moving the actuator further downstream towards the separation line. That would give more control authority to the actuator, decrease the time scales of the separation/reattachment process and improve the performance for the closed-loop system. This was not done in this work due to technical constraints, but it would be worth to test in the future.

Another important result of the open loop tests is that, for a constant free-stream velocity, the system can be modelled as a first order linear one. This result was not expected at the start of the study, as the turbulent

boundary layer flow is highly non-linear and its interaction with the actuator was expected to be even more complex.

Based on this analysis, different closed-loop controllers were implemented experimentally (PI and LQR). Two objectives were targeted: the first one was to reattach the flow with a minimum mass flow rate and a maximum reactivity, the second was to test the robustness of the control under variations of the free-stream velocities. Closed-loop configurations were able to increase the reactivity by more than 3 times compared to open-loop tests with an additional gain in terms of mass flow rate. In order to evaluate the robustness of the controller, the system was submitted to free stream velocity variations. Two types of tests were performed: small variations (i.e fast variations in time) with a fixed reference and large variations with an update of the reference based on the value of the free stream velocity. In both cases, the controller was found robust to maintain the desired state of the flow with, however, a larger delay in the time reactivity that needs to be improved in the case of small variations. For the case of large variations (i.e slow variations in time) the robustness was particularly good.

To comfort the experiments and thanks to the fact that the system could be modelled simply as a first order, extensive simulations were performed to better assess the performances and limitations of the different controllers. The system was addressed as an LTI system and so LTI controllers were designed (PI, LQR and H_∞). Simulink-based simulations are conducted for the closed-loop system. Both PI and LQR controllers performed well, by having shorter settling time compared to open-loop system. The general behaviour observed in the experiments was retrieved, although some quantitative differences appear. For example, the closed-loop simulation carried out at $U_\infty = 5\,m/s$, showed differences up to 10% compared to experimen-

tal results. This can be solved by selecting an actuation frequency which a better linear approximation, such as with $f = 30Hz$ at $U_\infty = 8$ and $10\,m/s$. Also the simulated closed-loop response of the system with time-delay and LQR controller with $K = 8$, showed strong oscillation which does not appear experimentally. This is unexpected, due to the fact that all other simulations were successful to predict the shape of response with sometimes slight differences.

The H_∞ controller was shown to be more robust in terms of attenuating disturbances. The performance and robustness of the H_∞ controllers can be further improved by taking into account the uncertainty of the model and by using weighted H_∞ controllers. This can be interesting when implementing these controllers experimentally in the future.

One important and limiting finding of the present work is that the system model is changing with the free stream velocity. This puts limitations to a small range of variation around the operating free stream velocity, with, as observed experimentally, delay in the response. In order to overcome this limitation, the system was treated as a linear parameter-varying (LPV) system. Then, a robust H_∞ LPV controller was proposed, that performs well for free stream velocity variations in all the operating range. In particular, it improves significantly the performances for small velocity variations compared to the experimental results and this coping with a strong noise.

Due to time limitation, only the simulated closed-loop control with the PI and LQR controllers was validated experimentally. The simulation allowed us to extend the study to Riccati-based and LMI-based H_∞ controllers which still need such an experimental validation. This is also true for the LPV controllers. This can be a future work for more robust closed-loop control which offers interesting possibilities toward real applications.

One important aspect which was not considered in the present contribution is the underlying physics behind the results observed. It would be of interest, in particular, to investigate the flow mechanisms linked to the attachment/separation control processes under the action of the actuators. This implies some sophisticated experiments based on time resolved PIV measurements synchronized with the control system and accompanying advanced data reduction approaches. This opens the route for future improvements of efficiency and robustness of the controller.

Appendix A

Linear Systems

This appendix reviews some basic system theoretical concepts. The notions of controllability, observability, stabilizability, and detectability are defined and summarized. More details can be found in Zhou and Doyle [1999].

A.1 Descriptions of Linear Dynamical Systems

Let a LTI dynamical system be described by the following linear constant coefficient differential equations:

$$\begin{aligned} \dot{x} &= Ax + Bu \quad x(t_0) = x_0 \\ y &= Cx + Du \end{aligned} \tag{A.1}$$

where $x(t) \in \mathbb{R}^n$ is called the system state, $x(t_0)$ is called the initial condition of the system, $u(t) \in \mathbb{R}^m$ is called the system input, and $y(t) \in \mathbb{R}^p$ is the system output. The $A\,, B\,, C$, and D are appropriately dimensioned real constant matrices.The corresponding transfer matrix from u to y is defined as

$$Y(s) = G(s)U(s) \tag{A.2}$$

where $U(s)$ and $Y(s)$ are the Laplace transforms of $u(t)$ and $y(t)$ with zero initial condition ($x(0) = 0$). Hence, we have

$$G(s) = C(sI - A)^{-1}B + D \tag{A.3}$$

Note that the system equations A.1 can be written in a more compact matrix form:

$$\begin{bmatrix} \dot{x} \\ \dot{u} \end{bmatrix} = \begin{bmatrix} A & B \\ C & D \end{bmatrix} \begin{bmatrix} x \\ u \end{bmatrix} \tag{A.4}$$

To expedite calculations involving transfer matrices, we shall use the following notation:

$$\left[\begin{array}{c|c} A & B \\ \hline C & D \end{array}\right] = C(sI - A)^{-1}B + D \tag{A.5}$$

Note that

$$\begin{bmatrix} \mathrm{A} & \mathrm{B} \\ \mathrm{C} & \mathrm{D} \end{bmatrix}$$

is a real block matrix, not a transfer function.

A.2 Controllability and Observability

Some very important concepts in linear system theory are introduced.

Definition A.2.1 *The dynamical system described by equation A.1 or the pair (A, B) is said to be controllable if, for any initial state $x(0) = x_0$, $t_1 > 0$ and final state x_1, there exists a (piecewise continuous) input $u(.)$ such that the solution of equation A.1 satisfies $x(t_1) = x_1$. Otherwise, the system or the pair (A,B) is said to be uncontrollable.*

The controllability (and the observability introduced next) of a system can be verified through some algebraic or geometric criteria.

Theorem A.2.1 *The following are equivalent:*
(i) (A, B) *is controllable.*
(ii) The controllability matrix

$$\mathcal{C} = \begin{bmatrix} B & AB & A^2B & \dots & A^{n-1}B \end{bmatrix}$$

has a full row rank.

Definition A.2.2 *An unforced dynamical system* $\dot{x} = Ax$ *is said to be stable if all the eigenvalues of* A *are in the open left half plane; that is,* $Re\lambda(A) < 0$. *A matrix* A *with such a property is said to be stable.*

Definition A.2.3 *The dynamical system of equation A.1, or the pair* (A, B), *is said to be stabilizable if there exists a state feedback* $u = -Kx$ *such that the system is stable (i.e.,* $A - BK$ *is stable).*

Theorem A.2.2 *The following are equivalent:*
(i) (C, A) *is observable.*
(ii) The observability matrix

$$\mathcal{O} = \begin{bmatrix} C \\ CA \\ CA^2 \\ \dots \\ CA^{n-1} \end{bmatrix}$$

has a full column rank.
(vii) (A^T, C^T) *is controllable.*

Definition A.2.4 *The dynamical system of equation A.1, or the pair* (C, A)*, is detectable if* $A + LC$ *is stable for some* L*.*

Theorem A.2.3 *The following are equivalent:*
(i) (C, A) *is detectable.*
(ii) There exists a matrix L *such that* $A + LC$ *is stable.*
(vii) (A^T, C^T) *is stabilizable.*

A.3 System Norms

The notion of system norm is the size of a transfer function or LTI system. In this appendix we explore some important systems norms.

Consider $G(s)$ in equation A.3, then the H_2 norm of G is defined as

$$\|G\|_2 = \sqrt{\frac{1}{2\pi}\int_{-\infty}^{\infty} trace\left\{G(j\omega)^* G(j\omega)\right\} d\omega} \tag{A.6}$$

and the H_∞ norm of G is defined as

$$\|G\|_\infty = \sup_{\omega} \bar{\sigma}\left\{G(j\omega)\right\} \tag{A.7}$$

where $\bar{\sigma}$ is the maximum singular value. $\|G\|_\infty$ is the distance in the complex plane from the origin to the farthest point on the Nyquist plot of G, and it also appears as the peak value on the Bode magnitude plot of $|G(j\omega)|$.

Appendix B

Fluidic Actuator Modeling and Numerical Solution

Equation of the acoustics used in chapter 2, were derived from the mass and momentum conservation equation, and recalled here. They were solved using numerical schemes also described in the following.

B.1 Equation of the Model

The derivation of the transient model of the actuator done by Braud and Dyment [2011] is explained below. Recalling the mass and momentum equations:

- Continuity equation (1D)

$$\frac{\partial \rho}{\partial t} + \frac{\partial (\rho u)}{\partial x} = 0 \tag{B.1}$$

- Momentum equation (1D)

$$\frac{\partial u}{\partial t} + u\frac{\partial u}{\partial x} + \frac{1}{\rho}\frac{\partial p}{\partial x} + \frac{\psi u^2}{2D} = 0 \tag{B.2}$$

where ψ the friction coefficient. The speed of sound in ambient air c_o is given by:

$$c_o^2 = \frac{\partial p}{\partial \rho} = \frac{p - p_o}{\rho - \rho_o}.$$

Introducing the dimensionless acoustic pressure, $(p - p_o)/\rho_o c_o$,

$$\partial\theta = \frac{\partial p}{\rho_o c_o} = \frac{c_o}{\rho_o}\partial\rho$$

By replacing ρ in equation B.1 using the previous relation, it follows:

$$\frac{\partial \theta}{\partial t} + \frac{\partial \theta}{\partial x} + \frac{\rho c_o}{\rho_o}\frac{\partial u}{\partial x} = 0$$

Neglecting the nonlinear term and assuming density variations are small (i.e $\rho \sim \rho_o$). Equation B.1 can be replaced by:

$$\frac{\partial \theta}{\partial t} + c_o\frac{\partial u}{\partial x} = 0$$

Equation B.2 can also be rewritten using the same assumptions:

$$\frac{\partial u}{\partial t} + c_o\frac{\partial \theta}{\partial x} + \frac{\psi u^2}{2D} = 0$$

For numerical implementation the dimensionless variables are introduced as follows: $\theta^* = \theta/U$, $v^* = u/U$, $x^* = x/L$ and $t^* = c_o t/L$, where U is the steady exit velocity and L the tube length. Then we get,

$$\frac{\partial \theta^*}{\partial t^*} + \frac{\partial v^*}{\partial x^*} = 0 \tag{B.3}$$

$$\frac{\partial v^*}{\partial t^*} + \frac{\partial \theta^*}{\partial x^*} + \frac{\psi U L}{2D c_o}v^{*2} = 0 \tag{B.4}$$

With the following initial and boundary conditions:

$\theta^* = v^* = 0$, for $t^* = 0$, $0 < x^* < 1$

$v^* = 1$, for $t^* > 0$, $x^* = \frac{Ut^*}{c_o}$

$\theta^* = 0$, for $t^* > 0$, $x^* = 1$

When there is no friction ($\psi = 0$), it can be expressed in a matrix form as follows:

$$\frac{\partial U^*}{\partial t^*} + A\frac{\partial U^*}{\partial x^*} = 0 \tag{B.5}$$

where, $A = \begin{pmatrix} 0 & 1 \\ 1 & 0 \end{pmatrix}$, and $U^* = \begin{pmatrix} v^* \\ \theta^* \end{pmatrix}$. For simplicity equation B.5 can be rewritten in the following form:

$$u_t + Au_x = 0 \tag{B.6}$$

where,

$u = \begin{pmatrix} v^* \\ \theta^* \end{pmatrix}$.

B.2 Numerical solution

In the following subsections, a description of the numerical techniques, used to solve equation B.6 is given. Further details can be found in Leveque [2008].

The linear hyperbolic system

Consider the linear system (B.6), where $A \in R^{m\times m}$ is a constant matrix. This system is called hyperbolic if A is diagonalizable with real eigenvalues, so that we can decompose

$$A = R\Lambda R^{-1} \tag{B.7}$$

150

where $\Lambda = diag(\lambda_1, \lambda_2, ..., \lambda_m)$ is a diagonal matrix of eigenvalues and $R = [r_1, r_2, ..., r_m]$ is the matrix of eigen vectors. Note that $AR = R\Lambda$, i.e.,

$$Ar_p = \lambda_p r_p, \forall \rightarrow p = 1, 2, ..., m. \tag{B.8}$$

The system is called strictly hyperbolic if the eigenvalues are distinct. The discretization of the $x - t$ plane was performed by choosing a mesh width Δx and a time step Δt, and define the discrete mesh points (x_i, t^n) by:

$$x_i = i\Delta x$$
$$t^n = n\Delta t$$

The pointwise values of the true solution (u) will be denoted by:

$$u_i^n = u(x_i, t^n)$$

B.2.1 Flux-Limiter Method

The numerical solution of equation B.6 can be viewed in conservative form (Leveque [2008]):

$$u_i^{n+1} = u_i^n - \frac{\Delta t}{\Delta x}[F(u_i^n, u_{i+1}^n) - F(u_{i-1}^n, u_i^n)] \tag{B.9}$$

or

$$u_i^{n+1} = u_i^n - \frac{\Delta t}{\Delta x}[F(u^n; i) - F(u^n; i-1)] \tag{B.10}$$

where $F(u^n; i)$ is called flux, two types of fluxes were used. The first one is the Lax-Wendroff, which is high order flux $(F_H(u^n; i))$.

$$F_H(u^n; i) = \frac{1}{2}A(u_i^n + u_{i+1}^n) - \frac{1}{2}\frac{\Delta t}{\Delta x}A^2(u_{i+1} - u_i) \tag{B.11}$$

The second one is the low order Upwind flux $(F_L(u^n; i))$:

$$F_L(u; i) = \frac{1}{2}A(u_i + u_{i+1}) - \frac{1}{2}|A|(u_{i+1} - u_i) \tag{B.12}$$

where

$$|A| = R|\Lambda|R^{-1} \tag{B.13}$$

with $|\Lambda| = diag(|\lambda_1, ..., |\lambda_m||)$ (Leveque [2008]).

The lax-Wendroff method was working well in smooth regions while the Upwind scheme behaved well near discontinuities. This highlight the Flux-limiter method, where a hybrid of these two methods can be used. We can view the high order flux as consisting of the low order flux plus a correction:

$$F_H(u^n; i) = F_L(u^n; i) + [F_H(u^n; i) - F_L(u^n; i)] \tag{B.14}$$

In a flux-limiter method, the magnitude of this correction depends on the data, so the flux becomes

$$F(u^n; i) = F_L(u^n; i) + \Phi(u^n; i)[F_H(u^n; i) - F_L(u^n; i)] \tag{B.15}$$

where $\Phi(u^n; i)$ is the limiter. If the data u is smooth near u_i then $\Phi(u^n; i)$ should be near 1, while in the vicinity of a discontinuity, $\Phi(u^n; i)$ should be near zero.

Bibliography

M. Abdalla, E. Nobrega, and K. Grigoriadis. Fault detection and isolation filter design for linear parameter varying systems. *ACC01-IEEE*, page 1310, 2000.

B. Allan, J. Juang, D. Raney, A. Seifert, L. Pack, and D. Brown. Closed-loop separation control using oscillatory flow excitation. *NASA Langley Research Center, NASA/CR, Tech.Rep.*, 2000.

M. Amitay and F. Cannelle. Evolution of finite span synthetic jets. *Physics of fluid*, 18, 2006.

M. Amitay and A. Glezer. Role of actuation frequency in controlled flow reattachment over a stalled airfoil. *AIAA*, 40:209–216, 2002a.

M. Amitay and A. Glezer. Controlled transient of flow reattachment over stalled airfoils. *Int. J. Heat Fluid Fl.*, 23:690–699, 2002b.

M. Amitay and A. Glezer. Flow transients induced in a 2d airfoil by pulse-modulated actuation. *Experiment in Fluid*, 40:329–331, 2006.

P. Apkarian, P. Gahinet, and G. Becker. Self scheduled h infinity control of linear parameter-varying systems: A design example. *Automatica*, 31: 1251–1261, 1995.

A.A. Barberopoulos and K.P. Garry. The effect of skewing on the vorticity produced by an airjet vortex generato. *The Aeronautical Journal*, (2275), March 1998.

J. F. Beaudoin, O. Cadot, J. L. Aider, and J.E. Wesfreid. Bluff-body drag reduction by extremum seeking control. *Journal of Fluids and Structures*, 22:973–978, 2006.

Ralf Becker and Rudibert King. Comparison of a robust and flatness based control for separated shear flow. In *16th IFAC World Congress*. International federation of automatic control, 2005.

Ralf Becker, Maiko Garwon, Carsten Gutknecht, Gunter Barwolf, and Rudibert King. Robust control of separated shear flows in simulation and experiment. *Journal of Process Control*, 15:691–700, 2004.

Ralf Becker, Rudibert King, Ralf Petz, and Wolfgang Nitsche. Adative closed-loop separation control on a high-lift configuration using extremum seeking. *AIAA*, 45:1382–1392, 2007.

Nicolas Benard, Eric Moreau, John Griffin, and Louis N. Cattafesta. Slope seeking for autonomous lift improvement by plasma surface discharge. *Experiment in Fluids*, 48:791–808, 2010.

J. P. Bons, R. Sondergaard, and R. B. Rivir. The fluid dynamics of lpt blade separation control using pulsed jets. In *ASME Journal of Turbomachinery*, volume 124, Jan 2002.

S. Boyd and C. Barratt. *Linear Controller Design: Limits of Performance*. Prentice-Hall, 1991.

C. Braud and A. Dyment. Model of an impulsive actuator for flow control applications. *Physics of fluid (submitted)*, 2011.

C. Braud, M. Andino, J. Pinier, J. Ausseur, H. Higuchi, M. Glauser, and D. Hunter. Separation control of flow over naca 4412 hydrofoil using zero net-mass flow actuators. In *In European Forum on Flow Control*, Poitiers - France, October 2004.

C. Braud, A. Dyment, D. Kostas, J.M. Foucaut, and M. Stanislas. Analysis and modelling of a fluidic actuator. In *ASME Summer Heat Transfer Conference*, Jacksonville, USA, August 10-14 2008.

T.P. Bray and K.P. Garry. Optimization of air-jet vortex generators with respect to system design parameters. *The aeronautical journal*, (2430), October 1999.

J. Carlier and M. Stanislas. Experimental study of eddy structures in a turbulent boundary layer using particule image velocimetry. *Journal of Fluid Mechanics*, 535(36):143–188, 2005.

L. Cattafesta and M. Sheplak. Control strategies - actuators and sensors. In *Flow Control: Fundementals, Advantages and Applications*, Lecture Series 2009-02. Von Karman Institute, March 2009.

J. Choi, A. M. Annaswamy, H. Lou, and F. S. Alvi. Active control of supersonic impingment tones using steady and pulsed microjets. *Exp. Fluids*, 41:841–855, 2006.

D.C. Mc Cormick. Boundary layer separation control with directed synthetic jets. *AIAA paper*, (2000-0519), January 2000.

C. Cuvier, C. Braud, J.M. Foucaut, and M. Stanislas. Flow characterisation and parametric study of passive and active vortex generators on the lml-avert ramp. European project, AVERT Consortium, 2010.

A. Darabi and I. Wygnanski. Active management of naturally separated flow over a solid surface. part 1. the forced reattachment process. *J. Fluid Mech*, 510:105–129, 2004.

J. Van de Vegte. *Feedback Control Systems*. Prentice-Hall, New Jersey, 1994.

M. GadelHak. *Flow Control : passive, active and reactive flow management*. Cambridge, 2000.

Mohamed GadelHak. Modern developments in flow control. *Applied Mechanics Reviews*, 49:365–379, 1996.

P. Gahinet, A. Nemirovski, A. Laub, and M. Chilali. *LMI Control Toolbox*. Mathworks Inc., 1995.

Greenblatt, D., and I. Wygnanski. The control of separation by period excitation. *Progress in Aerospace Science*, 36:487–545, 2000.

Lars Henning and Rudibert King. Multivariable closed-loop control of the reattachment length downstream of a backward-facing step. In *16th IFAC World Congress*, Praha, Czech Rep., July 2005.

Rudibert King-Ed. *Active Flow Control*. Springer-Verlag, nnfm 95 edition, 2007.

J. Kostas, J.M. Foucaut, and M. Stanislas. Investigation of the use of pulsed jets for boundary layer control on aircraft. European project, AEROMEMS II Advanced Aerodynamic Flow Control Using MEMS, 2005.

J. Kostas, J.M. Foucaut, and M. Stanislas. The flow structure produced by pulsed-jet vortex generators in a turbulent boundary layer in an adverse pressure gradient. *Flow Turbulence and Combustion: Special Issue on Air-jet Actuators and Their Use for Flow Control*, 78(3-4), June 2007.

J. Kostas, J.M. Foucaut, and M. Stanislas. The effects of pulse frequency and duty cycle on the skin friction downstream of pulsed jet vortex generators in an adverse pressure gradient turbulent boundary layer. *Aerospace Science and Technology*, 13:36–48, 2009.

Randall J. Leveque. *Numerical Methods for coservation laws*. Birkhauser Verlag, Basel, Switzerland, 2008.

R.S. Lin and N. Hariharan. Analysis of fluidic vortex valves for airflow control in combustors. In *AIAA paper*, number 2002-2946, St Louis, Missouri, June 2002.

F. Lundell. Pulse-width modulated blowing/suction as a flow control actuator. *Experiments in Fluids*, 35:502–504, 2003.

R. Mathis, A. Lebedev, E. Collin, J. Delville, and J. P. Bonnet. Experimental study of transient forced turbulent separation and reattachment on a bevelled trailing edge. *Exp. Fluids*, 46 (1):131–146, 2009.

K.R. McManus, H.H. Legner, and S.J. Davis. Pulsed vortex generator jets for active control of flow separation. In *25th AIAA Fluid Dynamicss Conference*, Colorado Springs, CO, June 20-23 1994.

R. Petz and W. Nitsche. *Designing Actuators for Active Separation Control Experiments on High-Lift Configurations*. Springer-Verlag, r. king (ed): active flow control edition, 2007.

Jeremy T. Pinier, Julie M. Ausseur, Mark N. Glauser, and Hiroshi Higuchi. Proportional closed-loop feedback control of flow separation. *AIAA*, 45: 181–190, 2007.

Seifert, A. A. Darabi, and I. Wygnanski. Delay of airfoil stall by periodic excitation. *Journal of aircraft*, 33:691–698, 1996.

A. Seifert and L. Pack. Oscillatory control of separation at high reynolds numbers. *AIAA*, 37:1062–1071, 1999.

W.L. Siauw, J. P. Bonnet, J. Tensi, L. Cordier, B.R. Noack, and L. Cattafesta. Transient dynamics of the flow around a naca 0015 airfoil using fluidic vortex generators. *International Journal of Heat and Fluid Flow*, 31:450–459, 2010.

H.A. Siller and H.-H. Fernholz. Manipulation of the reverse-fow region downstream of a fence by spanwise vortices. *European Journal of Mechanics B/Fluids*, 26:236–257, 2007.

R. Skelton, T. Iwaski, and K. Grigoriadis. *A Unified Approach to Linear Control Design*. Taylor and Francis, 1998.

B. L. Smith and G. W. Swift. A comparaison between synthetic jets and continuous jets. *Experiments in Fluids*, 34:467–472, 2003.

Qi Song, Ye Tian, and louis Cattafesta. Mimo feedback control of flow separation. *AIAA*, page 0109, 2007.

A. P. Szumowski and J. Wojciechowski. Semi-circular rods used to control turbulent boundary layer separation at cylindrical surface. *Journal of Fluids Engineering*, 128:628–631, 2006.

Ye Tian, louis Cattafesta, and Rajat Mittal. Adative control of separated flow. *AIAA*, pages 1401–1411, 2006a.

Ye Tian, Qi, and louis Cattafesta. Adative feedback control of flow separation. *AIAA*, page 3016, 2006b.

C.P. Tilmann and K. L. Langan. Characterization of pulsed vortex generator jets for active flow control. In *RTO AVT Symposium on Active Control Technology for Enhanced Performance Operational Capabilities of Military Aircraft, Land Vehicles and Sea Vehicles*, Germany, 8-11 May 2000.

D. R. Williams, D. Cornelius, and C. W. Rowley. Supersonic cavity response to open loop forcing. In *First Berlin Conference on Active Flow Control*, Sept 2006.

K. Zhou and J. Doyle. *Essentials of Robust Control*. Prentice-Hall, 1999.